

https://dspace.org/

Attenuation of very fast transients in Sf6 insulated high voltage busducts. theoretical and experimental considerations of the effect of a ferromagnetic coating applied to busbars.

Jandrell, Ian Robert.

1990
https://hdl.handle.net/10539/25459

Downloaded from a DSpace repository. https://dspace.org/

ATTENUATION OF VERY FAST TRANSIENTS IN SF_6 INSULATED HIGH VOLTAGE BUSDUCTS. THEORETICAL AND EXPERIMENTAL CONSIDERATIONS OF THE EFFECT OF A FERROMAGNETIC COATING APPLIED TO THE BUSBARS.

Ian Robert Jandrell

A thesis submitted to the Faculty of Engineering at the University of the Witwatersrand, Johannesburg, in fulfilment of the requirements for the degree of Doctor of Philosophy.

Johannesburg, August 1990

Declaration

I declare that this thesis is my own unaided work. It is being submitted for the Degree of Doctor of Philosophy in the University of the Witwatersrand, Johannesburg. It has not been submitted before for any degree or examination in any other University.

16 day of August 1990

ABSTRACT

Particularly at the higher system voltages, certain faults have been attributed to VFTs. This work presents a full frequency domain mathematical model of the effects likely to be introduced by the application of a thin ferromagnetic coating to the surfaces of the busbars as a means of attenuating these transients. Experimental verification shows the model to perform accurately as an analysis tool for a continuous coated co-axial system. While a comparison between the model developed here (based on a planar conductor) and the very accurate Bessel function solution is presented, it must be remembered that it is not feasible to include the effects of coatings in the latter solution. Hence it is used merely as a bench-mark for improvements to the general model. Consideration is also given to the transient skin effect, and this is shown to result in an increased attenuation of VFTs, detectable during high voltage experimentation. The frequency domain model is extended to that of a full travelling wave model for VFTs in GIS. The Fourier technique is used to move between the frequency and time domains. Laboratory results obtained at high voltage show that this technique will introduce both risetime increase and peak magnitude attenuation of VFTs. As the most frequent faults directly attributable to disconnector operation are known to be faults to earth at the switch, it is noted that the technique proposed in this work is uniquely suited for use in a design strategy that requires totally robust disconnectors at the expense of more severe VFTs in the GIS. The model is used to determine a range of physical characteristics of materials suitable for use in this application. While the characteristics of the most suitable materials have therefore been established, it is concluded that extensive metallurgical experimentation remains before this technique may be economically applied.

For Heidi

Acknowledgements

The author would like to express his sincere gratitude to both ESKOM and the University of the Witwatersrand for the financial support that has made this work possible. He would also like to thank BBT for providing the test vessel in which the high voltage experiments were conducted.

The author wishes to extend particular thanks to his supervisor, Professor JP Reynders, whose kind assistance and guidance extended to matters well beyond the scope of the work presented in this thesis.

Table of Contents

Declaration i

ABSTRACT ii

Acknowledgements iv

Table of Contents v

List of Figures viii

List of Tables xi

List of Symbols xii

Preface 1

Chapter 1 : Introduction 2
1.1 Background 2
1.2 Advantages Offered by the Proposed Technique of Controlling VFTs 3

Chapter 2 : Problems Associated with VFTs 4
2.1 Background 4
2.2 Recording VFTs 5
2.3 Faults 6
2.3.1 The Frequency Content of VFTs 8
2.3.2 The Influence of VFTs on Insulation 9
2.4 Concluding Remarks 12

Chapter 3 : Techniques of Controlling VFTs 13
3.1 Introduction 13
3.2 Controlling the VFT 13
3.3 System Integrity 13
3.4 Areas of research hoped to reduce the detrimental influence of VFTs 15

Chapter 4 : The Mathematical Model 17
4.1 Introduction 17
4.2 Background 17
4.3 Modelling of the Skin Effect 18
4.4 Development of the Mathematical Model 20
4.4.1 The Concept of a Transmission Line 20
4.4.2 The Transfer Function of a Transmission Line 23
4.4.3 The Generalised Series Impedance per Unit Length of a Transmission Line 24
4.4.4 The Model 25
4.4.5 Correcting the Error in the Planar Model 35
4.5 Experimental Verification of the Model 37

Chapter 5 : Use of the Mathematical Model to Predict the Performance of Various Coating Materials 46
5.1 Background 46
5.2 Formation of a VFT. 46

5.3 Theoretical Study 48
5.3.1 Predicted Performance 48
5.3.2 Discussion of the Theoretical Investigation 54
5.4 Coating Performance 58
5.5 The Consideration of Four Materials for Use as Coatings 59
5.5.1 Coating Technique Considerations 59
5.5.2 The Four Materials 60
5.6 Concluding Observations 63

Chapter 6 : A Travelling Wave Model for VFTs and Laboratory Results 65
6.1 Introduction 65
6.2 The Model 66
6.2.1 Assumptions 67
6.2.2 Incorporation of Reflection and Transmission Coefficients 67
6.2.3 Verification of the Transient Analysis Model 72
6.2.4 A Theoretical Consideration 74
6.3 The Effect of Ferromagnetic Busbars 75
6.4 Consideration of the Transient Skin Effect in Coaxial Conductors 78
6.5 Concluding Remarks 82

CONCLUSION 83

References 84

Appendix 1 : The Free Charge Term Equals Zero For a Good Conductor 90

Appendix 2 : The Total Current in a Planar Conductor 91

Appendix 3 : Determination of Equation (4) of *Chapter 4* 92

Appendix 4 : Field Penetration into a Homogeneous Planar Conductor 93

Appendix 5 : Data Requirement for the Program *Skin* 97

Appendix 6 : Consideration of the Bessel Function Solution 99

Appendix 7 : Time Domain Definition Used in the Fourier Technique 111

Appendix 8 : Low Voltage Experimental Results 113

Appendix 9 : Theoretical Analysis of SF_6 Busducts 121

Appendix 10 : The Effects of Magnetic Field Intensity 127

Appendix 11 : Physical Attributes of Four Materials Considered for Use in this Application 144

Appendix 12 : Methods of Determining Material Characteristics 148

Appendix 13 : Magnetic Field Intensity within a Typical Busduct 150

Appendix 14 : Theoretical Examination of the Effectiveness of the Four Samples 151

Appendix 15 : Consideration of Reflection and Transmission Coefficients 160

Appendix 16 : Consideration of the Travelling Wave Model 162
Appendix 17 : Overview of Various Busbar Coating Techniques 167

List of Figures

Figure 1 5
Figure 2 7
Figure 3 8
Figure 4 9
Figure 5 14
Figure 6 21
Figure 7 22
Figure 8 23
Figure 9 25
Figure 10 26
Figure 11 28
Figure 12 31
Figure 13 36
Figure 14 38
Figure 15 38
Figure 16 39
gure 17a 41
Figure 17b 41
Figure 17c 42
Figure 17d 42
Figure 17e 43
Figure 17f 43
Figure 17g 44
Figure 18 44
Figure 19 46
Figure 20 47
Figure 21 47
Figure 22 48
Figure 23 49
Figure 24 50
Figure 25 50
Figure 26 52
Figure 27 53
Figure 28 56
Figure 29 57
Figure 30 58
Figure 31 59
Figure 32 61
Figure 33 65
Figure 34 66
Figure 35 68
Figure 36 69
Figure 37 71
Figure 38 72
Figure 39 73
Figure 40 74
Figure 41 76
Figure 42 77
Figure 43 78
Figure 44 79
Figure 45 81

Figure 46 82
Figure 4.1 93
Figure 4.2 95
Figure 6.1 100
Figure 6.2 101
Figure 6.3 102
Figure 6.4 103
Figure 6.5 104
Figure 6.6 105
Figure 6.7 106
Figure 6.8 107
Figure 6.9 108
Figure 7.1 111
Figure 7.2 112
Figure 8.1 114
Figure 8.2 115
Figure 8.3 116
Figure 8.4 117
Figure 8.5 117
Figure 8.6 118
Figure 8.7 119
Figure 8.8 120
Figure 9.1 121
Figure 9.2 122
Figure 9.3 123
Figure 9.4 124
Figure 9.5 125
Figure 9.6 126
Figure 10.1 128
Figure 10.2 129
Figure 10.3 130
Figure 10.4 131
Figure 10.5 132
Figure 10.6 133
Figure 10.7 134
Figure 10.8 135
Figure 10.9 136
Figure 10.10 137
Figure 10.11 138
Figure 10.12 139
Figure 10.13 140
Figure 10.14 141
Figure 10.15 142
Figure 10.16 143
Figure 11.1 144
Figure 11.2 145
Figure 11.3 146
Figure 11.4 147
Figure 12.1 148
Figure 14.1 152
Figure 14.2 153
Figure 14.3 154
Figure 14.4 155
Figure 14.5 156

Figure 14.6 157
Figure 14.7 158
Figure 14.8 159
Figure 15.1 160
Figure 16.1 163

List of Tables

Table 1 6
Table 2 11
Table 3 40
Table 4 51
Table 5 54
Table 6 61
Table 7 62
Table 8 69
Table 6.1 109
Table 8.1 119

List of Symbols

ε	absolute permittivity	F/m
ε_o	permittivity of free space	$8{,}85\times10^{-12}$[F/m]
ε_R	relative permittivity	
μ	absolute permeability	H/m
μ_o	permeability of free space	$12{,}57\times10^{-7}$[H/m]
μ_R	relative permeability	
σ	conductivity	S/m
Rd	absolute series DC resistance	Ω/m
Rd_1	DC series resistance of inner conductor	Ω/m
Rd_2	DC series resistance of outer conductor	Ω/m
Ld	external series inductance	H/m
Cd	shunt capacitance	F/m
Gd	shunt conductance	S/m
Zd	series impedance	Ω/m
Yd	shunt admittance	S/m
V	voltage	V
I	current	A
f	frequency	Hz
ω	angular frequency	radians/s
J	current density	A/m^2
E	electric field strength	V/m
B	magnetic flux density	T
H	magnetic field strength	A/m
ρ	volume density of charge	C/m^3

d_i	thickness of coating on inner conductor	m
d_g	thickness of coating on outer conductor	m
r_i	radius of inner conductor	m
r_g	inside radius of outer conductor	m

Preface

SF_6 was first synthesized from fluorine and sulphur in 1900 by H Moissan and P Lebeau. The first comprehensive investigations into the electrical behaviour of SF_6 in non-uniform fields under DC voltage were carried out in 1939 by H G Pollock and FS Cooper (Luxa et al, 1974). During the last quarter of a century it has found extensive use in metal-clad subs tations up to 765kV. SF_6 enjoys two unique characteristics that make it an ideal gas for use in GIS :

- *Its high electrical insulation strength*
- *Its excellent arc quenching behaviour.*

While many researchers have developed gasses which are superior in either one of these two aspects, there is still no gas which combines these two attributes as well as SF_6 does. The attachment properties of SF_6 are responsible for its high insulation level, while its relatively low ratio of the quantum energy for dissociation (production of constituent atoms of a molecule) to that for ionisation (production of ions) gives it its excellent arc quenching properties (6.2eV/15eV) (Boeck, 1988). Thus the ionisation and attachment coefficients for SF_6 make it a good high voltage insulator with a critical field of 89kV/mm.MPa *(this compared to a value for air of 23,5). It should also be borne in mind that the insulating ability of a gas decreases with decreasing pressure. Thus the controlled environment of GIS seemed to offer a very favourable solution.*

As with all developing technologies, a number of unanticipated problems have been encountered in applications making use of the gas - particularly in high voltage gas insulated systems (GIS). One class of problems in particular - those associated with the very high frequency transients generated during the operation of a disconnector switch - is addressed in this thesis. A number of faults recorded within GIS have been attributed to these fast-rising transient voltages and the ensuing travelling wave phenomena developed within the system. The thesis proposes that, if the rising edge of the transient can be made less steep, the resultant very fast transient (VFT) will be less severe, and hence less likely to cause faults.

The proposed technique is to apply a frequency dependent conductive coating to the busbars. While this will not adversely affect normal system operation, it will ensure the attenuation of frequency components of the waveform in the MHz range.

Throughout this thesis care has been taken to use the correct terminology. For example, the use of the name "Transient Enclosure Voltage (TEV)" is preferred to "Transient Ground Potential Rise (TGPR)", as the former describes precisely the observed effect, where it is the voltage recorded on the outer surface of the enclosure with respect to ground that is of importance. Further, reference is made to "Very Fast Transients (VFTs)" instead of "Very Fast Transient Overvoltages (VFTOs)", as the disconnector generated transients of concern in this work need not necessarily be over voltages. The noun "disconnector" is used to refer to the disconnector switch, and the abbreviation "GIS" is used to refer to a "Gas Insulated System" as opposed to Gas Insulated Switchgear. In all instances abbreviations are in the singular, with a plural "s" added when necessary.

A word used frequently in this thesis is "degradation", specifically with reference to the increase in rise time that occurs as the initial surges of a VFT travel within the system. Much the same way that a mountain slope is degraded over time - that is made more gentle by the actions of nature - so too this term is used in this text.

Chapter 1 : Introduction

1.1 Background

While SF_6 technology enjoys a highly respected service record throughout the world (Banfai, 1988; Dower, 1988; Esmeraldo, 1988; Frantz et al, 1990; Kawada et al, 1988), it has been noted that at service voltages of 420kV and above, a number of well defined problems can be attributed to the operation of a disconnector (Alvinson et al, 1988). However, now, as previously, there are a number of factors that make the use of a GIS attractive. Most large utilities, including ESKOM (The Electricity Supply Commission) in the Republic of South Africa, elected to use SF_6 GIS for very standard reasons:

- Aesthetic and environmental considerations
- Perceived increased reliability, and reduced maintenance costs
- Increased personnel safety
- Improved installation security

SF_6 technology enjoys these advantages in particular over conventional air insulated substations.

ESKOM is the main supplier of electricity in Southern Africa, being responsible for approximately 95% of the generating capacity on the subcontinent. The supply system is large by any standards, with over 170 000km of transmission line - including 18 000km energised at voltage between 220 and 400kV. It also has 100km at ±533kV DC, and about 900km at 765kV. An excellent summary of the electricity supply in Southern Africa is given by Norman (1988).

ESKOM controls two 765/400kV substations incorporating what could be considered to be the first gas insulated switchgear specially designed for 765kV operation. Not only are these substations designed for operation at this voltage, but also for operation at an altitude of up to 1 800m. In many respects the associated problems are comparable to those of a 1 000kV system operating at sea level. One of these stations is also located where very high lightning activity occurs, with a maximum lightning flash density of 10 flashes per square km per year.

Thus, although Southern Africa is a fairly late developer in the use of this technology, it is evident that she is now a world leader in its use. As elsewhere, there is an increasing awareness of the associated problems, including those related to the operation of a disconnector switch.

Disconnector induced failures may be broadly classified into two types:

- Failures that are time correlated with the operation of a disconnector (including flashovers to ground at the switch as well as in adjacent sections of busduct, and malfunctions related to electromagnetic interference (EMI))
- Equipment failure as a result of the repeated impingement of VFTs upon it.

It is often exceedingly difficult to relate the latter to VFTs as it is a long-term effect. It would be unwise, however, to ignore this effect.

1.2 Advantages Offered by the Proposed Technique of Controlling VFTs

In this thesis, a technique that takes advantage of the wide discrepancy in frequency between the power (50Hz) and VFT waveforms (up to 200MHz) is proposed. The application of a ferromagnetic coating to the surfaces of the busbars within the system will be considered.

As will be shown, the severity of a VFT may be defined in terms of:

- Its high frequency content
- Its peak magnitude (after reflections)

While very high frequency oscillations may contribute to the low breakdown voltages observed under VFT stimulation, it will also be shown that, in any GIS configuration, the peak magnitude is affected by the high frequency content (in particular, that associated with the initial rising edge of the VFT). It will be argued that by reducing the high frequency content, many of these undesirable features may be effectively eliminated.

As the application of a ferromagnetic coating introduces more pronounced attenuation at high frequencies, a further benefit relates to the design of the disconnector itself: It is well known that one of the most common faults experienced during disconnector operation is an earth fault at the switch. This is due to a leader breaking out to ground from the inter-contact arc. To a large extent this fault is eliminated by the use of a switch with a more homogeneous inter-contact field configuration. The resulting inter-contact breakdown is more rapid, but the coating will control the severity of the ensuing VFT.

A further advantage relates to the fact that the coatings will attenuate the initial surges as they travel away from the disconnector towards adjacent section and coupled equipment: It is well known that large trapped charge is undesirable for many reasons (Boggs et al, 1982; Boggs et al, 1984). Those failures that have occurred are generally in or very near to the disconnector vessel, within the region exposed to trapped charge, and subject to the highest transient voltage. In order to reduce the trapped charge, preference is given to slow-operating disconnector switches. However, while the magnitude of the resulting VFTs may be low, a large number are generated. The long-term effects of the VFTs upon coupled equipment is thus a consideration. The proposed technique will attenuate these transients, in particular reducing their high frequency content.

In summary it should be stressed that the primary motivation of this work was the protection of coupled equipment - line traps (outside the station), instrument transformers within the station. This required a reduction of the very high dV/dt of the VFTs. Any indication that flashovers within the gas may also be reduced is considered to be a bonus! This fact should be viewed in the light of recent reports noting the decreased breakdown voltage recorded under VFT stimulation in certain systems (Boeck, 1986). Such systems may be considered representative of many industrial GISs. Pertinent observations relate to the fact that the probability of a flashover increases not only with peak magnitude and the degree of field inhomogeneity, but also with the oscillating frequency.

The effect of coatings upon the high frequency content of VFTs will be stressed frequently. Relevant aspects of the problems relating to VFTs, as well as possible means of controlling them, will be discussed in the following two chapters.

Chapter 2 : Problems Associated with VFTs

2.1 Background

SF_6 has been extensively used in high voltage applications during the past two and a half decades. However, as with all innovative technologies, a number of unanticipated problems have been encountered. One of these is associated with the VFTs resulting from the operation of a disconnector. The previous lack of interest in these VFTs was due largely to the fact that at lower than 300kV, no problems within GIS could be correlated with the operation of disconnectors (Alvinson et al, 1988).

The design and testing of disconnectors for use in GIS has received a great deal of attention in the technical literature of the past few years. The reasons for this include the difficulties in designing and testing disconnectors for EHV and UHV so as to ensure freedom from low probability failures to ground during normal operation, as well as the difficulty in measuring and simulating the transients generated within the substation by disconnector operation (Boggs et al, 1984).

In many cases, disconnector operation generates the highest line-to-ground voltages imposed on the switchgear during normal operation (Boggs et al, 1982; Kynast et al, 1984), and in EHV and UHV GIS VFTs could be a determining factor in the insulation design (Nakanishi et al, 1984). There is a growing concern, however, that even at low voltages VFTs may pose a problem (Reynders, 1987a).

It is clearly shown in *figure 1* that only in UHV systems are VFTs expected to exceed the rated lightning impulse withstand level (LIWL). Lightning events are relatively rare, while in the order of 10^3-10^4 disconnector operation may be recorded at a substation in one year (Thione, 1984). Furthermore, it should be remembered that not every lightning surge is as high as that level, whereas (for any GIS) every disconnector operation will result in the expected overvoltages. This fact has been stressed in support of this work (Jandrell, 1988), and has also been noted elsewhere (Bargigia et al, 1984). As many VFTs occur at voltages well below the LIWL, they can hardly be controlled by surge arresters. Indeed, damage to surge arresters at conventional substations due to repeated VFT application has been reported (Nishiwaki et al, 1983).

The fact that these phenomena are receiving increasing attention relates not only to the use of high operating voltages, but more specifically to the increased need for reliable system operation associated with those systems. More power is being committed to a single line.

Recent analysis conducted by a group representing a number of South Africa suppliers of the technology (Frantz et al, 1990) show that the failure rates experienced are comparable, if not better, than those accepted as the world averages. (The analysis was of faults that have occurred in Southern African installations of 88kV or greater.)

Also, as is typically the case, and specifically with regard to newer technologies, the analysis indicates that the failure rate records of the installations show a reducing trend with increasing years of service. Frantz et al (1990) pointed out that for all faults remedial actions was taken to eliminate the defect - either by means of modifications, or complete replacement. The South African experience indicates that defects tend to manifest themselves well within the normal maintenance period of the first year of service. This is an encouraging observation.

It is important to examine some of the reasons why faults occur. More specifically, factors that have contributed to the present level of interest in VFTs having been reached will be overviewed.

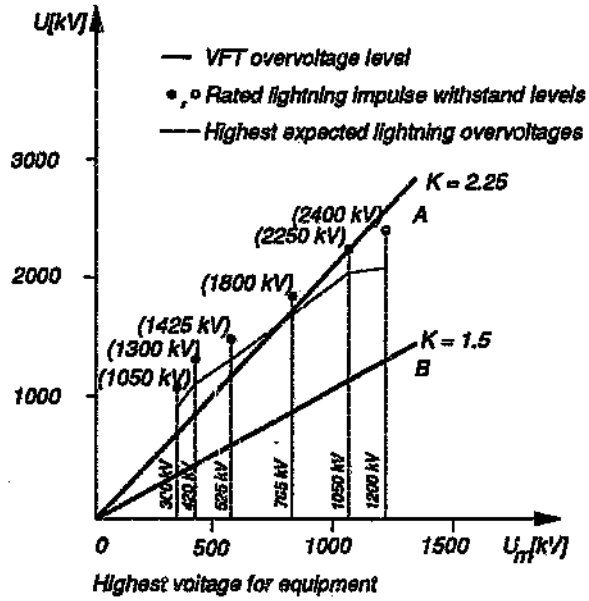


Figure 1: Comparison of overvoltage levels due to disconnector operations, lightning and rated lightning impulse withstand levels (Bargigia et al, 1984).

First, the recording of VFTs will be discussed. There is no doubt that it is of great important to be able to accurately measure the relevant frequencies of VFTs, and to be able to explain the origin of those components. Thereafter, the broad topic of faults will be covered. This topic will be crudely divided into an examination of the high frequency content of VFTs, and a discussion of the insulating behaviour of the gas. While the last-mentioned relates in many respects to the peak magnitude of the VFT, the inter-relationship between this and the high frequency components will be stressed.

2.2 Recording VFTs

While the recording of VFTs is not an associated problem, it has certainly contributed to some of the previous ignorance concerning these phenomena. Even reports appearing in late 1988 (Auriol et al, 1988) indicated the severe problems encountered by investigators trying to measure VFTs accurately. The importance of sufficient bandwidth, correct screening, and properly designed voltage dividers cannot be sufficiently stressed. It is the opinion of this author that many early investigators did not utilise proper measuring equipment, and thus failed to perceive some of the very important characteristics of VFTs. It is well known, for example, that filtering will reduce the apparent peak magnitude of a VFT. Also, the response time of the divider is crucial. Well known equations govern its design, and competent examples can be fairly easily constructed (Jandrell, 1985). It was only in 1982 that researchers began to stress the importance of the very fast rising edge (2 – 12ns). Curiously, also, the measurements reported during the 80's show a distinct increase in the highest observed frequency. Only in 1987 did researchers begin to pay careful attention to the frequency content of these phenomena to the extent that they considered the Fourier analysis a useful tool (Reynders, 1987(b); Jandrell, 1987; Aron, 1987). *Table 1* notes some of these observations. It does not pretend to be exhaustive.

Table 1 : Causes of transient voltages in various frequency ranges.

		kHz range		"Low" MHz range		High MHz range		
Year	Comments	Ascribed cause	Frequency kHz	Ascribed cause	Frequency MHz	Ascribed cause	Frequency MHz	Simulation Measurement
1981 Narimatsu et al, 1981)	Typical GIS configuration	Resonance between GIS and external station	500	not identified	6			EMTP simulation
1981 Narimatsu et al, 1981)		Resonance between GIS and external station	250	not identified	6,5			Measured
1981 Narimatsu et al, 1981)		not identified	360	not identified	3,0			EMPT simulation
1981 Narimatsu et al, 1981)		not identified	300	not identified	6,9			Measured
1982 (Boscttl, 1982)	GIS	Supply side reactance	~2,1	Supply and load capacitive resonance	~1,5			Measured
1982 (Boggs et al, 1982)				Travelling wave phenomena	1-10	Voltage collapse during spark development	5-20 ns risetime	Measured
1983 (Nishiwaki et al, 1983)	Typical GIS configuration	not identified	~400	not identified	several MHz			EMPT simulation
1984 (Kynast et al, 1984)	GIS	Supply and load charge equalization	several kHz	Travelling wave phenomena	1,25	(limited bandwidth of measuring equipment)	12MHz	Measured
1984 (Edlinger et al, 2134)	Test pole	Resonance between capacitance of busduct and bus transformer	~800	Travelling wave phenomena	7,2			Measured
1984 (Boggs et al, 1984)	Typical GIS configuration			Travelling wave phenomena	~5	Voltage collapse during spark development	~20 MHz 5-15ns risetime	Measured and predicted
1986 (Boeck et al, 1986)	Test pole			Travelling wave phenomena	(Frequency is dependant upon the configuration)	Voltage collapse during spark development	4-10ns risetime	Measured
1986 (Reynders, 1986)	Test pole			Travelling wave phenomena	14	Formation time of conduction channel	4-7ns risetime	Measured
1987 (Boeck, 1987)		Oscillation of whole system	<100	Travelling wave phenomena	1-50	Voltage collapse during spark develop-ment	2-12ns risetime	

2.3 Faults

Faults ascribed to VFTs relate to two distinct features:

- The high frequency content

- The peak magnitude reached after multiple reflections

These may be further subdivided into the failure of solid insulation of connected equipment, and the occurrence of faults to ground within the gas. With reference to *figure 2*, it is important to note the influence of the high frequency content upon the peak magnitude of a VFT. A number of important features are clearly evident from the figure:

- The most prominent effect relates to the risetime of the initial surges
- A significant difference in peak magnitude results immediately - at the first major peak
- The difference in peak magnitude does not become progressively larger
- The displacement in time between the corresponding peaks and troughs does not shift with increasing time.

These are important, and should be contrasted with the effects introduced by the application of ferromagnetic coatings to the busbars. There is no significant skin effect, implying a similar transmission characteristic for both the fast and the slow rising VFTs.

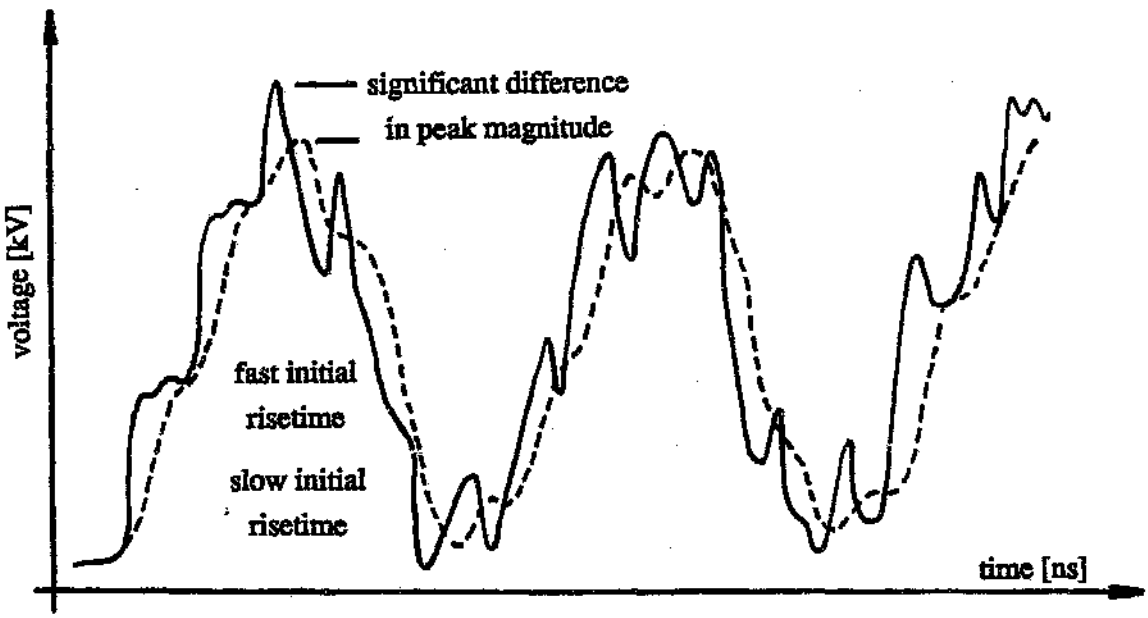


Figure 2 : The effect of the initial risetime on the peak magnitude of a VFT. The resulting reduction in high frequency content is also evident. Note, however, that there is no evidence of an increasing shift between corresponding peaks of the two waveforms with time. This prediction is for a system with the dimensions shown in *figure 33*.

A further consideration relates to breakdowns recorded within an industrial SF_6 insulated systems at voltages well below those anticipated (Reynders, 1987a). The implications of this are that even at systems operating at well below the UHV level (refer to *figure 1*), faults may be initiated by VFTs.

In the broadest context, three problem areas relating to VFTs have been distinguished (Nakanishi, 1984, Jandrell 1988):

- Breakdowns (as noted above)
- The TEV (specifically the EMI radiated, and the influence on personnel (sparking between earthed parts))
- Damage to line equipment (a long term effect, particularly with regards to equipment having coils where a non-linear stress distribution may occur)

2.3.1 The Frequency Content of VFTs

Since the proposed technique is reliant upon the skin effect, it is of particular concern to study the origin of the highest frequency component of VFTs, and to note how this may effect the system integrity.

It is well known that field inhomogeneity results in prolonged breakdown times, which is indicative of a leader-type breakdown mechanism. A further influencing factor on the breakdown voltage is the dominant frequency associated with the VFT at the point of breakdown. It has been noted that in practice the highest significant frequency component which can exist will be limited by the finite voltage collapse time of voltage at the contacts (Alvinson et al, 1988). This fact is borne out in the Fourier analyses conducted by Reynders (1987b) and Boeck (1989). In their analyses, they suppressed the DC component of the sampled transient and thus produced a very clear indication of the relevant frequency components. Refer to *figure 3*. A typical VFT is shown in *figure 4*.

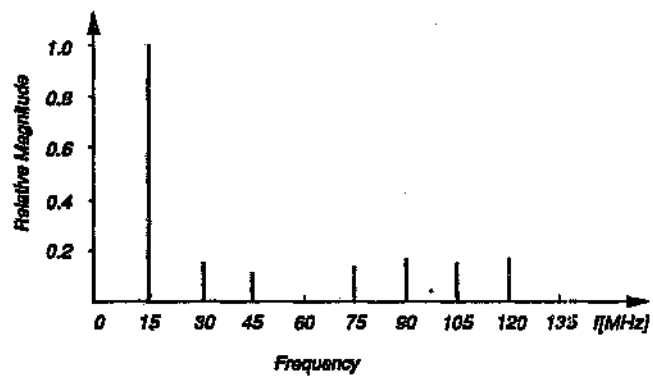


Figure 3 : High frequency content of a typical disconnect transient (Reynders, 1987b).

Very little effort to date has been directed towards understanding the underlying physics of dielectric performance under VFT conditions. In particular, it is important to observe the effect of the oscillatory nature of a VFT upon breakdown voltage. It has been argued that a strong relationship may exist between this oscillation and the breakdown voltage in SF_6. This process is described by Luxa et al (1988).

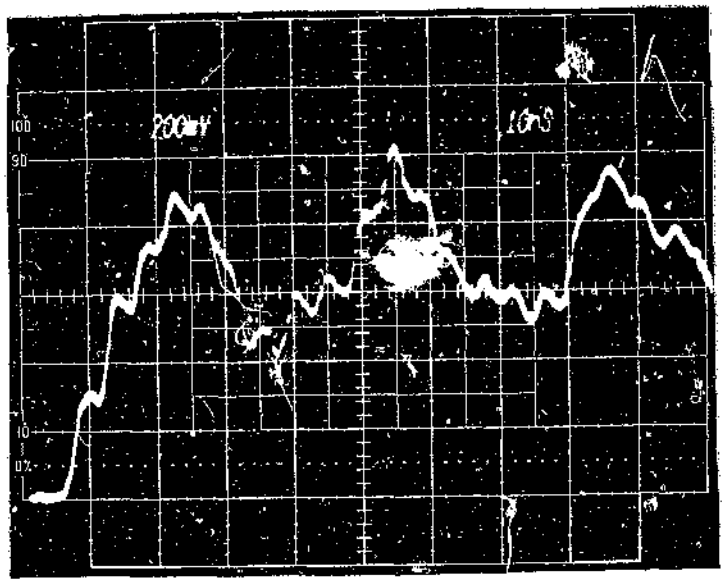


Figure 4 : A VFT recorded in the Werner von Siemens High Voltage Test Facility at the University of the Witwatersrand. The dimensions of the test vessel in which this VFT was recorded are discussed elsewhere (Reynders, 1986). Scales: 20ns per large division; 90,8kV per large division.

It thus appears clear that the dominant frequencies of the transie are important aspects governing the insulating behaviour of the gas. In particular the configuration induced oscillation has an important effect upon the breakdown development to ground. Of course, the oscillating frequency depends for its severity upon the initial rising edge. Reducing the frequency component in that edge will reduce the severity.

2.3.2 The Influence of VFTs on Insulation

While increasing the knowledge base of the processes involved in breakdown in SF_6 is an on-going process, many years of collective research has lead a number of researchers to the conclusion that, in accordance with the upturning trend of the lightning impulse voltage-time (V-t) curve with decreasing front rise times, all VFT flashover values must be above the LIWL (Alvinson et al, 1988). The upturning trend is, of course, due mainly to the statistical and formative time lags for development of the breakdown channel. Negative polarity VFTs produce breakdown at slightly higher values than positive VFTs, and after longer times. Thus SF_6 gas itself is an excellent insulant under VFT conditions. Concern, however, must be with the performance of the gas when it is pressurised within an industrial GIS.

While the breakdown time (Toepler's spark equation) and the breakdown voltage for a homogeneous field configuration (eg coaxial) can be accurately predicted, (in an industrial system) the presence of even very small imperfections can lead to longer breakdown times and significantly lower breakdown voltages (Auriol et al, 1988, Boeck et al, 1986; Luxa et al, 1988; Reynders, 1986; Reynders, 1987a). Indeed, in severe cases the V-t curve exhibits a down-turning trend with decreasing time to breakdown. Solid insulation (of coupled equipment) is most profoundly affected by the steepness (dV/dt) of the VFT (Thione, 1984).

Considering first the breakdowns in the gas, the most common fault is the breakout of an arc to ground at the disconnector. *Table 2*, compiled from a random list of references, indicates that approximately twice the number of ground faults occur at the disconnector in comparison to faults in adjacent sections.

Mention is also made in the table to the effects on coupled equipment. While the number of these is small, this must be viewed in the light that it is a long-term effect, and hence difficult to attribute directly to VFTs.

Table 2 : Commonly reported faults ascribed to VFTs. In particular, the concern for faults to ground at the disconnector is of importance. Often, however, techniques of reducing the frequency of these faults implies that more severe stressing of the rest of the GIS results. This will be discussed later.

Year	Increased disconnector stressing	Faults to ground at disconnector	Faults to ground in adjacent sections	TEV	EMI	Premature instrument transformer ageing	Damage to outdoor lightning arresters	Excessive insulation stress w.r.t. grounded enclosure	Damage to coupled equipment due specifically to initial rising edge
1958 (Korden et al, 1958)							X		
1958 (Griscom, 1958)							X		
1960 (Weber, 1958)							X		
1979 (Nishikawara et al, 1979)		X							
1981 (Narimatsu et al, 1981)		X							
1982 (Bosetti et al, 1982)	X	X	X					X	
1982 (Boggs et al, 1982)		X	X						
1983 (Nishiwaki et al, 1983)		X							
1984 (Fynaut et al, 1984)		X		X				X	
1984 (Hosanda et al, 1984)				X		X			
1984 (Thione, 1984)		X		X	X			X	X
1984 (Nakanishi et al, 1984)		X		X	X			X	
1984 (Eilinger et al, 1984)		X		X					
1984 (Boggs et al, 1984)		X	X						
1986 (Boeck et al, 1986)			X					X	
1987 (Reynders, 1987a)			X						
1987 (Morf, 1987)							X		
1987 (Kobayashi et al, 1987)		X	X					X	
1987 (Hara et al, 1987)								X	
1987 (Hopkins, 1987)		X		X	X				
1987 (Reynders, 1987b)				X	X			X	

2.4 Concluding Remarks

While most recent work concludes that the breaking out of the spark at the disconnector is the most important consideration in design, breakdowns in remote ares are also considered to be important. Many failures to ground occur unexpectedly and remain unexplained (Fujimoto et al, 1988; Lewis et al, 1988). Hence a very thorough understanding of the gas, as well as the design of the disconnector and the GIS is required. An inter-relationship between all these features determine the nature of the VFT, and hence system reliability. To date, disconnector generated VFTs are still a more common cause of failure than externally generated surges. While experience is generally good, it is becoming increasingly accepted that VFTs do present a problem. Not only are problems being encountered, but, more importantly, they have been recognized as a very important field requiring a lot of research effort. Attempts to reduce their effects are but one facet, and many questions still remain unanswered (Weck, 1988).

Therefore, despite the increasing amount of work being performed in the field of GIS, a number of important insulation problems are still far from being resolved. Indeed, some, like the problems associated with VFTs are only now being fully understood and even recognized. By 1984 no performance testing standard nor specification existed concerning the switching capability of a GIS disconnector (Bargigia et al, 1984; Edlinger et al, 1984; Nakanishi et al, 1984). A further problem appears to relate to an incomplete understanding of the true nature of breakdowns caused by VFTs.

The importance of frequency - upon the peak magnitude of the VFT, the insulating behaviour of the gas, and upon the performance of solid insulation and coupled equipment - has been stressed. In the light of the discussion contained in this chapter, it is clear that any reduction in the frequency content of a VFT must have a positive influence upon the reliability of the system. Furthermore, this technique allows use to be made of disconnector switches that disallow the arc breaking out to ground at their contacts, and do not result in large trapped charge being left on the busbars.

Chapter 3 : Techniques of Controlling VFTs

3.1 Introduction

There are two aspects to VFT fault control:

- Attenuating or controlling the VFT itself
- Design of the system to ensure integrity under the influence of VFTs

There is no doubt that, to date, the latter option has been followed, although it is likely that a compromise between these two approaches may be the most suitable. Making the system resilient has included the introduction of test techniques, as well as improvements in the disconnector design. This may be understood in the light of *chapter 2*.

3.2 Controlling the VFT

There are two fairly obvious techniques that may be employed in order to control the VFT:

- Filtering
- Resistive Dissipation

Filtering the VFTs would have to be at what ever frequency is considered desirable, in order, say, to remove a dominant component of the rising edge. Note that it is not feasible to entertain the thought that the oscillatory frequency (at a point) can be filtered out directly. This can only be achieved by filtering of the rising edge (as we saw in the previous chapter). While the technique holds great promise, clearly the use of discrete element filters is impracticable. To protect adjacent duct sections (which is in reality all the any filtering technique can do), the filters should be as close to the disconnector as possible, as their effect is only felt as the surge passes. Since a low pass filter would have to present a high series impedance to the high frequencies in order to block them, high voltages would necessarily be developed. Such filters are difficult to realise in a GIS.

The second technique involves the use of resistors to dissipate energy at the disconnector contacts. While prototypes of disconnectors incorporating resistors have been produced, no commercial models have been utilised (Ozawa et al, 1986). Testing of these devices indicated an expensive, unreliable product. Also, it must be noted that the occurrence of resistors on one side only implies a directional nature for the device. While the initial transient may be controlled on one side, 0.5pu may well occur on the other. Further, therefore, no reduction in the dV/dt of the rising edge will occur, but certainly the peak magnitude of the VFT will be controlled. Any frequency filtering caused by the resistors is utterly system dependent. Furthermore, should the resistor react for this with, say, system capacitance, the fast rising edge precludes initially the capacitance on the far side of the resistors, as the transient has not yet got there, and hence knows nothing about it. Hence the attractiveness of a distributed technique.

It is the contention of this thesis that the proposed distributed technique may offer a more suitable solution.

3.3 System Integrity

As noted in *chapter 2*, faults within the system may occur in one of two places:

- At the disconnector

- In adjacent sections, remote from the disconnector

In order to discuss the design of systems of high integrity, it is pertinent to briefly overview the formation of VFTs.

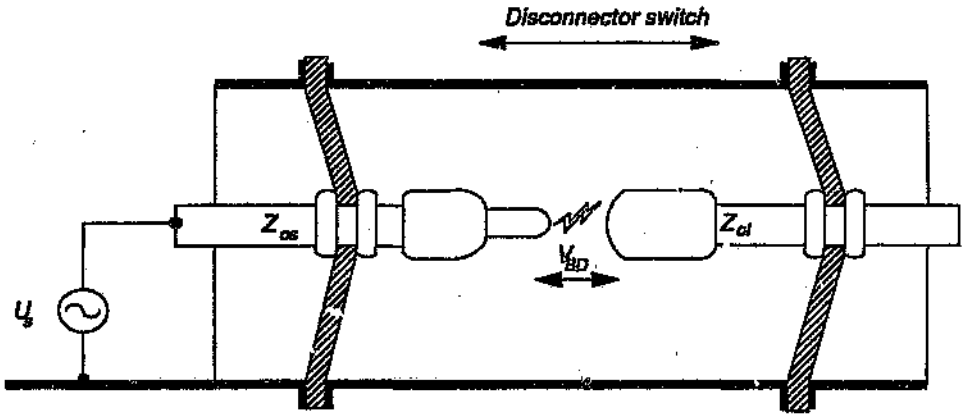


Figure 5 : The arc current formed during spark formation at a disconnector switch is a function of the characteristic impedances of the supply and load sides of the switch, where the 50 Hz supply voltage is given by U_s.

Disconnector operation typically involves slow-moving contacts, which switch small capacitive charging currents on no load. This results in numerous discharges, restrikings of the disconnector, which occur repetitively. The sequence of restrikes is determined by the electrode gap-dependent breakdown voltage, V_{BD} (refer to *figure 5*), and the potential difference of the load and supply side across the contact. This gives rise to numerous transient events during each disconnector operation. Each breakdown initiates a voltage collapse on either side of the disconnector. The magnitude of the surge is dependent upon:

- V_{BD} - which, due to the slow action of the disconnector, is typically a peak voltage
- The characteristic impedance of the GIS on either side of the disconnector

These surges have very short risetimes, and as they propagate within the co-axial network of the GIS, very little loss. They reflect and transmit (in reality all they do is refract, since there is always a phase shift associated with Z_o) at the internal discontinuities, and generate time and position dependent overvoltages. Thus the specific configuration of the GIS dictates the peak overvoltage attained at any particular location for any particular disconnector. While it is not inconceivable that judicious design can alleviate many of the problems, this is unrealistic, since to design to such constraints will drastically alter the physical dimensions of the various sections of GIS (remember that there is little loss). The length of the GIS segments controls the frequency of oscillation. This oscillation may indeed affect the occurrence of ground faults in adjacent sections, and thus controlling may well be advantageous. But it remains the risetime of the initial surges, T_r (refer to *appendix 7*) which really dictates many of the detrimental features. As time progresses and the waveform develops after multiple reflections, it ceases to depend on travelling wave phenomena, and begins to depend more upon the overall circuit parameters.

With regard to the rising edge, computations have shown that the magnitude of voltage components above 10MHz are determined by the duration of T_r. It is thus of prime importance to understand the sequence of spark development (Edlinger et al, 1984):

- At time zero, wherever the first ionisation occurs, a leader-like discharge starts in the axial direction towards the opposite electrode, and branches into a leader tree
- After about 30ns, one of the branches has reached the other electrode
- After another 4ns, the gap is crossed by a conducting arc channel

Thus each restrike generates a spark which equalises the potential at the disconnector contacts. The crossing of the gap by a conducting arc channel therefore stimulates the transient event. For homogeneous fields, this breakdown time is accurately predicted by Toepler's spark law. This gives the time T_r. During T_r, the spark resistance changes from very large to very small. Based roughly on this theory, the breakdown time across the gap of a disconnector can vary from 2 to 20 ns - depending largely upon the field inhomogeneity. The more inhomogeneous the field, the more leader breakdown will dominate, and hence the longer the risetime.

It has already been established that longer rise times are, in many case, desirable. Recall, however, that in a homogeneous electric field, a very fast discharge propagation in SF_6 - a streamer-like phenomena - is reported; whereas in an inhomogeneous field, leader-like propagation can be observed (Edlinger et al, 1984). While neither pure leader nor pure streamer form in disconnectors, it is the leader characteristic, with its associated branchings, that determines the flashovers to ground at the disconnector. Every disconnector has a varying degree of inhomogeneity. It is therefore advantageous to attempt to achieve a uniform field configuration at a disconnector - purely for operational integrity. Indeed, all reported techniques for achieving operational integrity relate directly to the field inhomogeneity. The only exception is increased disconnector chamber diameter. (Remember that the inhomogeneity is defined for the field between the contacts).

For an optimised disconnector design, as mooted in *chapter 2*, the individual arcs concentrate radially in a limited area, and in an area of lower radial field intensity because their axial length is much shorter for the same voltage. This greatly reduces the risk of the arc breaking out. Thus disconnectors are optimised in order to increase their own operational integrity. This does have ramifications for the rest of the system.

As a homogeneous field generates more rapid breakdown, this inevitably leads to more severe VFTs being formed, thus shifting the weakness of the system away from the disconnector. While this is a sound principle, some of the recent work relating to V-t curves as reported in the previous chapter, as well as the effect of the very fast risetime on adjacent sections and equipment belie this fact. However, as most ground flashes have been reported at the disconnector, it is more sound to do this, and then to examine techniques of controlling the VFTs thus generated. It is believed that the proposed technique offers a solution.

In two papers by Boeck (1987; 1989), the major attributes of VFTs are discussed, with particular regard to the influence various system parameters have on the form of the transient, and the effects of GIS configurations.

3.4 Areas of research hoped to reduce the detrimental influence of VFTs

A definitive recent paper on the topic of improved reliability of GIS notes five of its constituent authors' current work in this regard (Fujimoto et al, 1988):

- Methods to determine the reliability-related operational characteristics of GIS disconnectors
- Methods for calculating the magnitude of internally generated transients
- Methods for mitigating transients on control wiring to improve relaying reliability and facilitate the use of electronic equipment in GIS
- Improved high voltage commissioning test techniques to assure surge integrity
- Methods for the safe handling and disposal of solid and gaseous decomposition by-products during maintenance

It is thus abundantly clear, that in late 1988, it was the respected opinion that disconnectors deserved much greater research effort, particularly relating to aspects likely to result in maloperation. Understanding the underlying physics is one thing, but avoiding faults should be a priority reached in any way. In this research we concentrate on the high frequency components, arguing that their removal will result in a better system.

It is thus well understood and accepted that VFTs only result in breakdown under inhomogeneous field conditions in ideal industrial systems. Thus a valid controlling technique on breakdowns is to ensure that the system is ideal! This is a particularly onerous task at EHV and UHV. The techniques discussed in this chapter will no doubt help in this regard. It must be noted that it is predominantly the peak magnitude that is of consequence in these considerations, which it has been shown is closely related to the high frequency content of the VFT (particularly the rising edge).

As system faults caused by VFTs are well documented, reliable sections of GIS can be readily designed. Techniques employed in order to make disconnectors more reliable have also been noted. The technique proposed in this work will serve to complement those noted above.

Chapter 4 : The Mathematical Model

4.1 Introduction

A technique is proposed whereby the rising edge of the initial disconnector surge is filtered as it propagates within the system. This is done with the aid of a conductive coating (with electrical characteristics different to those of the busbars) applied to the busbar and grounded enclosure surfaces. Realising such a system in a laboratory for high voltage testing proved to be impractical, and it was found to be more useful to conduct a full theoretical study followed by simple experiments based on this proposal. In *chapter 6*, the results of high voltage tests conducted in a test vessel are presented.

4.2 Background

The objective of a mathematical model is to facilitate the establishment of a better understanding of a physical system - an understanding which may not even be deduced from a full comprehension of the design of the model itself.

Thus the model should serve the purpose of actually helping in the evolvement of a technique for achieving something. Of course, once the model has been developed, it must be ensured that it corresponds with reality, and where it does not, efforts must be made to enhance it, or to establish why the correspondence is not perfect.

While many models of transmission lines have been established in the past, the model to be developed here is unique in a number of ways:

- It allows for separate physical characteristics of the two conductors in the system. It thus fully accounts for the outer grounded enclosure
- It allows for different coatings to be independently applied to the two conductors in the system
- It is based on engineering assumptions that allow it accuracy for the systems under consideration in this investigation

These assumptions, made at the very outset of the investigation, and based on practice to date in the modelling of GIS, will be discussed in full. Indeed, the unique attributes may be adequately defined by the "generality" of the model. It is this generality, however, which is vital in order to facilitate the extensive theoretical study reported herein.

The availability of rapid computing power also facilitates the establishment of a simple program to execute the model, thus precluding unnecessary simplifications that may detract from the accuracy of the model.

As the effect of coatings is being considered, it is apparent that the skin effect as it applies in coaxial systems must be considered. This effect itself is well known, and has indeed been quantified in many applications and systems for decades. When coatings are applied, or very wide bandwidths are required, however, the tendency has been to simplify the models developed:

- Generally, the computing power was limited .
- The application did not warrant it

- The systems was considered to consist of two identical (physical parameters) conductors

Notably, the very wide bandwidths are seldom required in reality. In this application, because the pulse and 10-90% surge attenuation are found to be slightly different in the important frequencies involved, the very wide was deemed necessary.

While many of the existing models are even applicable to this work under certain conditions, the broad band of the model here developed, as well as its generality, facilitate easy and accurate time domain examination of the system transfer function.

In order to develop any working model, the constraints and requirements must be very well established. Where applicable in a given situation, valid approximations may be made.

The comparative accuracy of the model, based on the Bessel function solution, is shown. As the model developed here is based on a planar approximation, the Bessel function solution is used to establish a suitable correction factor.

4.3 Modelling of the Skin Effect

Modelling of the skin effect became necessary with the advent of the nanosecond pulse systems (nsps) of the late 50s, early 60s, when it was found that cables (particularly co-axial cables) attenuated signals far more than anticipated. This then paved the way for the development of a far greater understanding of the attributes of typical conductors.

Particularly in the early sixties to early seventies, with the advent of the nsps, much work was done in modelling and understanding the transient behaviour of co-axial cables (Nahman, 1962; Nahman, 1972). The simple skin effect (ie skin effect which occurs in a homogeneous conductor), and the skin effect in heterogeneous plane conductors, and the effects of factors like reflection, radiation and dielectric loss were discussed by Nahman in his classic paper of 1962. However, because of the nature of the systems considered, as well as the available computing facilities, these studies considered only the high frequency performance (Nahman, 1962), or only considered homogeneous conductors (Nahman, 1972). None allowed different coating materials to be independently applied to the inner and outer conductors.

Nahman (1962) derives high frequency solutions from which he obtains the unit step response. He considers a coaxial line having a lossless dielectric and consisting of conductors (for the inner and outer current paths) fabricated from identical materials, and having a metallic coating of different conductivity (to the conductors) applied. He then produces high frequency approximations by expanding the expression. As he limited his model to the high frequency region, it performs accurately at those frequencies. This is evident when it is compared to results obtained using the model presented in this thesis. Refer, for example, to *figure 8.7* of *appendix 8*. Again, the step response is obtained from the Heaviside step function. The assumption is made that the step rises infinitely rapidly.

As the stated objective was to determine why the attenuation characteristic of some cables departed from the well known skin effect $\sqrt{f}$ law, the analysis was readily expanded and enhanced to form a useful basis for the model developed for use in the work presented in this thesis.

The method of characteristics has also been used in the past in transmission line simulations - notably by Branin (1967), Liu (1968) and Frey (1961), who refer to it by its European title, the "Schneyder-Bergeron Method." (The method of characteristics is a standard mathematical technique for solving hyperbolic partial differential equations, and it leads to a particularly efficient algorithm for studying transmission lines). However, this method of time-domain

analysis is limited to the low frequency range where the frequency-dependent skin-effect loss may be neglected (Yen, 1982). Indeed, in an innovative expansion of the technique, Br ·in erred, and his new technique is only valid for loss-less and distortionless lines (Haack, 197).

In 1969, Herman W .Dommel (regarded by many to be the father of modern-day computer simulation of transmission lines) presented a paper in which he specifically examined digital computer simulation of electromagnetic transients in single- and multi- phase networks. The useful features of his program are the inclusion of non-linearities, any number of switchings during the transients, non-zero initial conditions, and great flexibility in specifying voltage and current excitations of various waveforms (Dommel, 1969).

Dommel assumed all lines to be lossless, but showed that they could be easily approximated very accurately in other ways. Although the method used by Dommel in this program is applicable to lossy lines, the ordinary differential equations it produces are not directly integrable (Branin, 1967). Further, at the time of Dommel's paper, the per unit length parameters were assumed to be frequency independent.

More recently, Nahman in conjunction with Holt, presented a paper in which the planar skin effect approximation was used (Nahman, 1972). The effect of coatings, however, was excluded. They discuss the regions of accuracy for the approximation. Due to the lack of computing power in those times, they put a large amount of effort into truncating and simplifying the results. While they did not account for the effect of coatings, they did note its effect in the recorded results.

When a method of simulating skin-effect is used where a waveshaping network is introduced at the end of a lossless transmission line, the network can produce a very good match between recorded and simulated results (Nahman, 1972). However, information can only be found for the end of a line, and one can learn nothing about the waveform distribution along the line. Accounting for reflections between such networks is also impossible. Furthermore, there is no firm basis for the design of waveshaping networks.

In a true time domain simulation presented by Chu-Sun Yen, Fazarinc and Wheeler, coated conductors are not considered (although it would be possible to adjust the values of the equivalent circuit elements so that the calculated loss agrees with the measured data) (Yen, 1982). While this modelling method may be beautiful and elegant, it requires exceedingly careful component value adjustment - particularly if the inner and outer conductors are of different materials, or are coated. No established technique of component value adjustment has been presented. Furthermore, the definition of the partial inductances utilised in this technique is invalid. It can thus at best only be considered to be an approximation.

Their technique has developed essentially from skin effect models of rotating machines. In these machines, however, the frequencies are low, and there are no coatings. For exceedingly thin coatings the top slice (as defined by the requirements of the model) must be exceedingly thin. This then predetermines the other slices in the model, and it becomes cumbersome. It must be noted, however, that Chu-Sun Yen, Fazarinc and Wheeler actually allow for true time domain transient analysis - ie the time it takes the fields to penetrate the conductor, and this effect on the attenuation, is allowed for. However, they go to some trouble to show that these results compare favourably with simple frequency domain results and that the actual transient event (or transient nature of the event) is short- lived. Also, while the usefulness of their method is clear, it is nevertheless important to be able to examine some form of frequency domain model of the system. The range of frequencies relevant to the work presented in this thesis preclude this time domain technique.

It should be noted, however, that in fact only Chu-Sun Yen, Fazarinc and Wheeler consider the truly transient case. Nahman and Holt use the technique utilised in the model to be presented here, but attempt to modify the steady state solution in order to obtain a pseudo-transient result. However, it should be remembered that such a solution is correct for only a fixed period of time - in fact an instant in time only. This is because the diffusion of the fields (ie flux establishment within the conductors) into the conductors is not accounted for in the steady state solution. It must further be noted that once periodicity has been forced upon the time domain signals of the system, the frequency dependent transfer characteristic thus defined is by its very nature a steady state solution. (Refer to *chapter 6*.) For this work, although "transient" events were under consideration, it was decided to develop a complete frequency domain model of the busbar and grounded enclosure since the technique under consideration was clearly frequency dependent. A full frequency domain model would then allow a study of the parameters of importance in this technique. In order to gain an impression of the effect of the proposed technique, the model was extended into the time domain using the Fourier technique.

4.4 Development of the Mathematical Model

4.4.1 The Concept of a Transmission Line

A transmission line is best described as a means of guiding energy from one point to another. When considering a gaseous dielectric (occupying the space between the conductors), the dielectric loss is typically ignored, as it will be for much of this analysis. Hence, in the case of perfect conductors, all the energy distributed down the line at one end, would be available at the other. The fields associated with the line would therefore not penetrate the conductors, but exist only between them, as penetration would imply losses.

This is clearly explained by the well-known equation defining the depth of penetration (skin depth) of an electric field into a conductor:

$$\delta = \frac{1}{\sqrt{\pi f \mu_o \mu_R \sigma}}$$

where : the symbols have their usual meanings. (Refer to *appendix 4*, where the field penetration into a homogeneous planar conductor is considered.)

A perfect conductor has infinite conductivity, which implies $\delta = 0$. Thus resistive loss within the conductors is zero. Dielectric loss, however, may still occur. For a perfect dielectric, the loss tangent is:

$$\frac{\sigma}{\omega\varepsilon} = 0$$

where : the symbols have their usual meanings.

However, as conductors are imperfect, the electric field will penetrate them. (Indeed, where the dielectric medium is a gas such as SF_6, conductor losses are dominant, and dielectric losses are negligible and may thus be ignored.) The fields therefore do not travel unimpeded, and various loss mechanisms come into play. In other words, losses occur *within* the material from which the conductors are made. It therefore becomes important to carefully distinguish between *internal* and *external* impedance effects associated with a transmission line. As will be shown, both need to be accounted for in order to accurately model the effects of interest.

The concept of an "internal" impedance effect further suggests that these impedances are not constant under all conditions, but must be functions of conductor parameters, and the "nature" of the electromagnetic fields they serve to guide. While this statement is suggestive of much of the analysis to follow, it is important to view the concept of internal and external impedance in terms of the lumped element model of the transmission line.

Conventionally, we think of a coaxial transmission line as consisting of two conductors, each carrying an equal and opposite current, with a voltage existing between the conductors. This is suggested in *figure 6*.

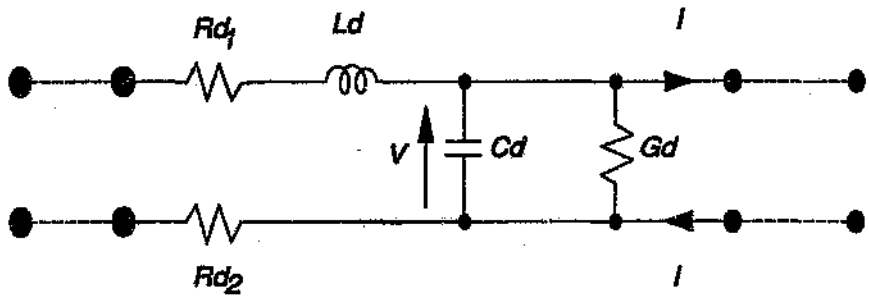


Figure 6 : Lumped parameter representation of a transmission line.

The current flow is affected by a distributed series inductance (*Ld*) representing the back induced voltage effects of the magnetic flux surrounding the conductors, and a series loss resistance ($Rd = Rd_1 + Rd_2$); the voltage between the conductors acts across a distributed shunt capacitance and conductance. In general, Rd_1 and Rd_2 would contribute equally to the voltage drop along the line. The series inductance, with *Ld*, is only defined for the inner conductor. (As will be explained later, *Ld* is really the external inductance term for the system.) The separate split series components are typically lumped together and represented in only one line of the two-conductor system.

Consider a 1m long section of high voltage busduct. The medium between the conductors is characterised in terms of:

permittivity

$\varepsilon = \varepsilon_o \varepsilon_R = \varepsilon_o$ because $\varepsilon_R = 1$

and permeability

$\mu = \mu_o \mu_R = \mu_o$ because $\mu_R = 1$

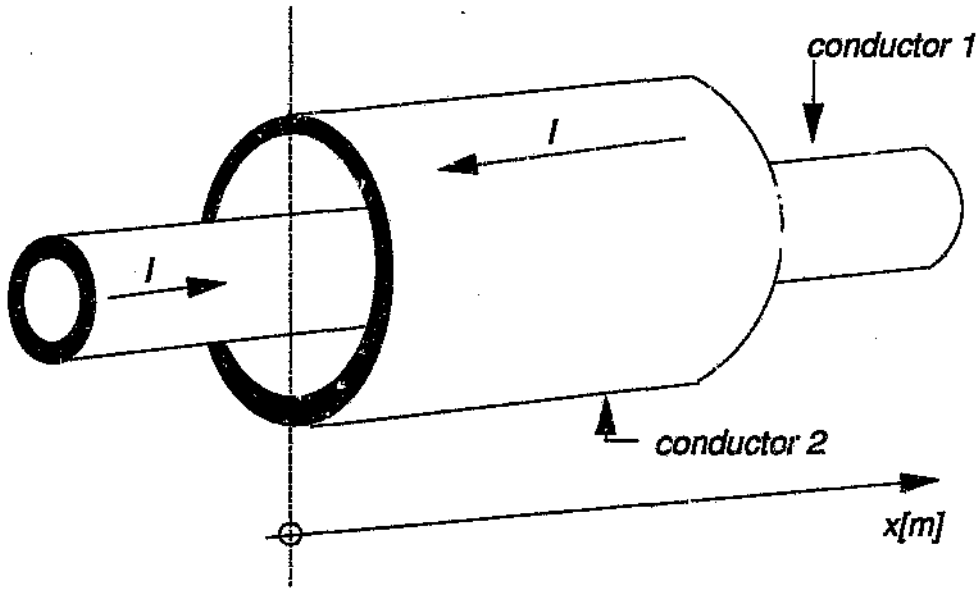


Figure 7 : Representation of a typical busduct, showing the transient current flowing on the outer surface of the busbar and the inner surface of the grounded enclosure. The numbering of the conductors is in accordance with the nomenclature used in this thesis.

From *figure 7* it is clear that conductor 1 and conductor 2 will not offer exactly equal impedance to the flow of energy. More specifically, they will not cause identical power losses. Both conductors must contribute to the effective impedance of the transmission line. Care must therefore be exercised when incorporating the loss elements of the two conductors, and it must be remembered that the effective series impedance must be given by the sum of the series impedances of each conductor. This should under no circumstances be mistakenly construed to imply that the electromagnetic wave travels at "differing speeds" in the two conductors. This is not true, as the velocity of propagation is a function of the characteristics of the entire system (two conductors), and is a function of $\beta\{\Im(\gamma)\}$. (β, the phase shift factor, is the imaginary component of γ, the propagation factor.) This is an important consideration in the following analysis, and serves adequately to illustrate that the contribution to loss from

each conductor must be accounted for individually. Consequently, it must be noted throughout this analysis, that any series term includes the sum of the terms associated with each of the two conductors.

4.4.2 The Transfer Function of a Transmission Line

Kirchoff's voltage and current laws to the circuit shown in *figure 8*, hence defining the series impedance per unit length of the line as:

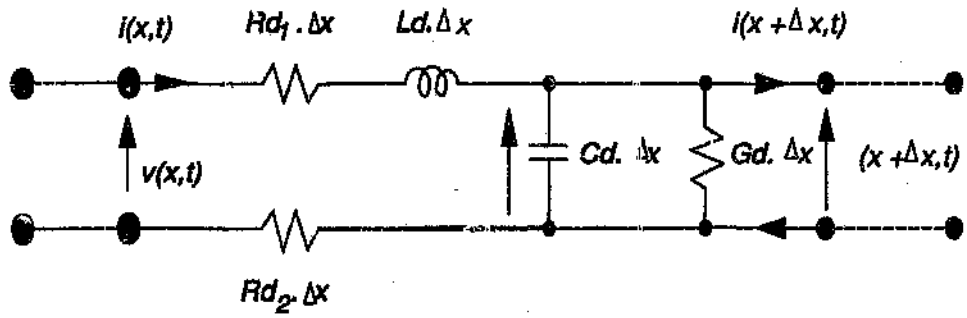


Figure 8 : An infinitesimal length of transmission line, showing the parameters associated with each of the two conductors. It is assumed that the conductors are operating under balanced conditions, where *Rd*,*Ld*,*Cd* and *Gd* are the parameter values per unit length.

$$Zd = (Rd_1 + Rd_2) + j\omega(Ld) \qquad (1)$$

Similarly the shunt admittance per unit length may be defined as:

$$Yd = Gd + j\omega \cdot Cd \qquad (2)$$

From equations (1) and (2) the propagation factor, γ, may be defined:

$$\gamma = \sqrt{Zd \cdot Yd}$$

$$= \alpha + j\beta$$

where: $\alpha = \Re(\gamma)$ = attenuation factor (the Real part of γ).

$\beta = \Im(\gamma)$ = phase shift factor (the Imaginary part of γ).

Hence, if γ can be found for a transmission line, then the transfer function for any voltage, E, along the line in either direction can also be found.

It is further important to note exactly what the parameters in *figure 8* represent:

Ld = external inductance per unit length (in other words, this term is merely based upon the total current flow within the conductor)
Cd = external capacitance per unit length
Gd = shunt conductance between conductors
Rd = DC series ohmic resistance per unit length

Therefore, assuming that the dimensions of a section of a GIS do not vary between a disconnector (D) and another point (G) distance l away within the GIS, the voltage transfer function between the two points is given by:

$$\frac{E_G(s)}{E_D(s)} = e^{-l\gamma(s)}$$

where : s is the Laplace transform complex variable, which reduces to the familiar steady state variable $j\omega$ when s is confined to the real frequency axis.

$\gamma(s)$, and its constituents, is as defined above.

When internal effect are considered, the term $Zd(s)$ has to be expanded in order to include internal effects of impedance. The following development of a model for γ will clarify this.

4.4.3 The Generalised Series Impedance per Unit Length of a Transmission Line

It has been established that the impedance of a transmission line incorporates an "external" and an "internal" component. The internal terms are due to fields penetrating the imperfect conductors, and thus account for losses. In fact, when the dielectric is considered lossless, the internal impedance terms exclusively account for the loss. It is clear that losses may only be fully accounted for by summing the internal impedance terms of the two conductors (inner busbar and outer grounded enclosure). Generally, internal losses are crudely accounted for by the term Rd. Rd is the DC resistance term, and hence assumes complete field penetration within the conductors. Of course, should the field penetration decrease, then the current within the conductors is confined to flow through a small cross-sectional area, and increased losses result (due to the higher series resistance).

Noting, therefore, the definition of the skin effect, Rd must be frequency dependent, and may not necessarily always be purely resistive (hence the specific definition of the external impedance terms earlier). It is thus only by careful modelling of the effect of frequency upon the value of Rd that the frequency dependent impedance of any transmission line may be accounted for. In general, therefore, the series impedance of a frequency dependent transmission line must be given by equation (3) below:

$$Zd = Rd + j\omega \cdot Ld + z(s) \qquad (3)$$

where : $z(s)$ is the internal impedance per unit length.

Rd is the value of z at $\omega = 0$.

Remember also that by definition the characteristic impedance of a transmission line, Z_o is given by:

$$Z_o = \sqrt{\frac{Zd}{Yd}}$$

Which, under lossless conditions, reduces to:

$$Z_o = \sqrt{\frac{Ld}{Cd}}$$

The concept of loss elements due to imperfect conductors necessitates a definition of the internal impedance terms (remember, *Rd* is an internal impedance term, but is a special case, as it is valid only at $\omega = 0$. For all frequencies above DC, an expression for $z(s)$ must be developed.)

A full development of a suitable expression for $z(s)$ will now be presented. The effects of coatings on both the busbar and the outer enclosure will be incorporated in the analysis.

4.4.4 The Model

The object is to develop an expression for the transfer characteristics of the system depicted in *figure 9*:

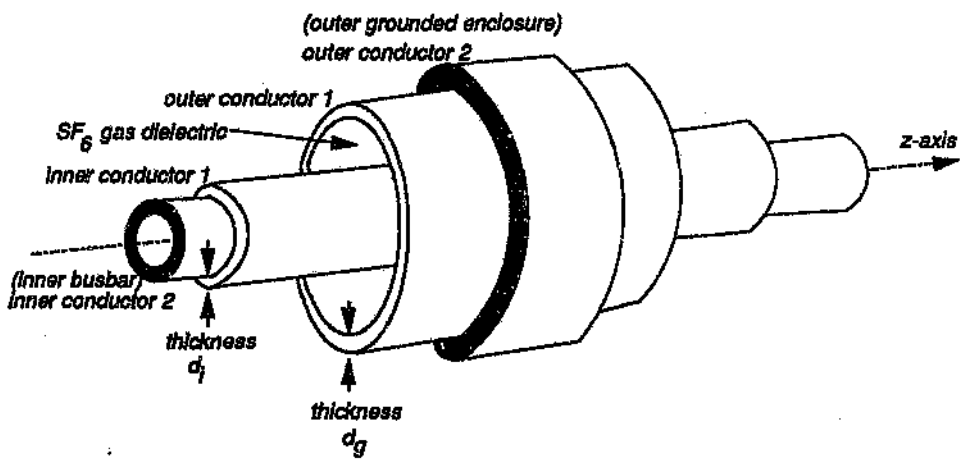


Figure 9 : Detail of a short section of busduct, showing the busbar and outer grounded enclosure, as well as the proposed coatings. Numbering used in this figure will be retained throughout the discussion. The figure is not to scale.

Note from the figure that conductor 2 (for both the inner and the outer conductor) represents the original busbar and outer grounded enclosure. Conductor 1 is, in both cases, the coating. Recall that it has been stated that all four of these materials may be independently defined.

Use is made in the analysis of simplifications that can apply due to the physical dimensions of the system. For this analysis, the system is reduced to that shown in *figure 10*. Concern is with the penetration of the component of the electric field, E_z, into the (generally) coated conductor. The validity of the planar approximation will be discussed later in this chapter, as will a suitable technique that minimises the error that this method introduces.

In other words, the system will be fully characterised in the frequency domain. Clearly any time domain waveform may be reduced to its com onental frequencies and the transfer function of the system applied to it. The resultant waveform may be recreated in the time domain.

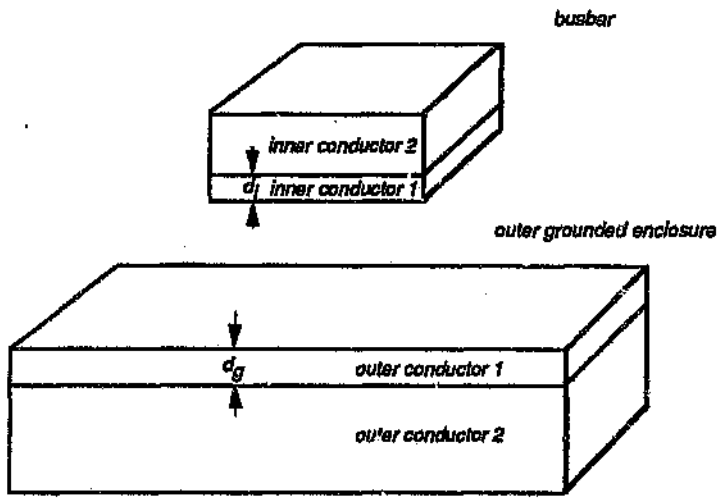


Figure 10 : Parallel plate approximation of a co-axial section of busduct, showing the coatings.

Note that $\vec{J} \equiv$ current density vector, having direction of current, i. (and that Ohm's Law states that $\vec{J} = \sigma\vec{E}$).

It must be stressed that the following derivations are valid only for good conductors, that is (refer to *appendix 1*):

- Conduction current is given by Ohm's Law, $\vec{J} = \sigma\vec{E}$
- The free charge term, ρ, is zero
- $\frac{\sigma}{\omega\varepsilon}$ *(loss tangent)* $\gg 1$ (Recall that we are assuming sinusoidal conditions)

From *figure 10*, a rectangular co-ordinate system may be used.

Prior to the development of the model, it is important to clearly explain the procedure that will now be followed:

- We consider one square metre of the surface of conductor 1 and conductor 2 (of unit length and unit width)
- We find the internal impedance term - ie accounting for the resistance and internal reactance of the conductors, noting the definition of internal impedance (Ramo, 1967). The internal impedance term per unit length of a conductor is the ratio of the surface electric field to the total current in the conductor. (The total current in the conductor is determined in *appendix 2*)

$$\Rightarrow Z_s = \frac{E_w}{I_z}$$

where : E_w is the electric field intensity at the conductor surface.

I_z is the total current flowing within unit width of the conductor.

- We find the internal impedance per unit length, z(s), from Z_s

The "internal" impedance term is thus clearly defined in terms of voltage per unit length at the surface of the conductor.

It is the volt drop along the conductor surface that defines the transmission characteristics of a set of conductors.

For the situation depicted in *Figure 10*, there is clearly no variation of the surface current density with y or z. We can thus write (refer to *appendix 3*):

$$\frac{d^2 J_z}{dx^2} = j\omega\mu\sigma J_z \qquad (4)$$

Consider equation (4) first as it applies to a block of coated material. It must be noted that this block may be considered to be part of either the inner busbar (subscript *i*), or the outer grounded enclosure (subscript g). The surface area of the block is a unit square. The block is depicted in *figure 11*:

Solutions to the distribution equations must be found for both media and matched at the boundary between the two. (Refer also to *appendix 4*.) The solution in either material is of the form of 4-4 (equation 4 of *appendix 4*). Subscript *1* refers to the coating material, and subscript *2* to the substrate. Hence:

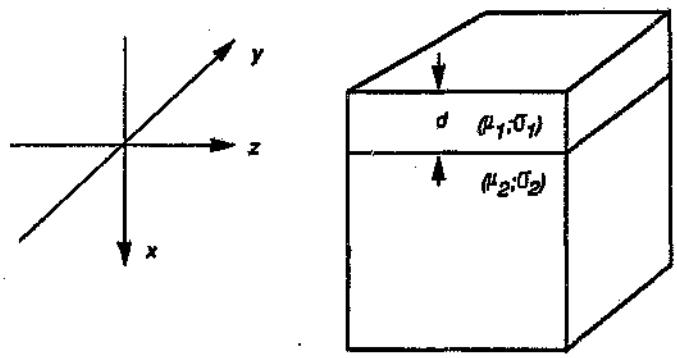


Figure 11 : A block of coated material, where the coating and the substrate have different electrical properties.

$$J_{z1} = C'e^{-\tau_1 x} + D'e^{\tau_1 x}$$
$$= C\sinh(\tau_1 x) + D\cosh(\tau_1 x) \qquad (5)$$

where : $\tau_1 = (1+j)\sqrt{\pi f \mu_1 \sigma_1}$ (refer to *appendix 4*)

Clearly there may be no positive exponential term for the busbar itself as the current density must be exactly zero at infinite depth. This form of the solution is the well known expression for the current density in a semi-infinite homogeneous planar conductor.

$$J_{z2} = Be^{-\tau_2 x} \qquad (6)$$

where : $\tau_2 = (1+j)\sqrt{\pi f \mu_2 \sigma_2}$

For both materials, from Ohm's law:

$$E_z = \frac{J_z}{\sigma} \qquad (7)$$

and:

$$H_y = \frac{1}{j\omega\mu}\frac{dE_z}{dx} = \frac{\sigma}{\tau^2}\frac{dE_z}{dx} \qquad (8)$$

Hence, from equations (5) and (6) we may define the electric and magnetic fields in the two materials, by using (7) and (8):

$$E_{z2}=\frac{B}{\sigma_2}e^{-\tau_2 x} \qquad E_{z1}=\frac{1}{\sigma_1}(C\sinh(\tau_1 x)+D\cosh(\tau_1 x))$$

$$H_{y2}=-\frac{B}{\tau_2}e^{-\tau_2 x} \qquad H_{y1}=\frac{1}{\tau_1}(C\cosh(\tau_1 x)+D\sinh(\tau_1 x))$$

Since tangential electric and magnetic fields are continuous over a boundary, we may evaluate the constants: ie $E_{z1}=E_{z2}$ and $H_{y1}=H_{y2}$ at x = d.

$$\therefore \quad \frac{D}{C}=-\left\{\frac{\sinh(\tau_1 d)+\left(\frac{\tau_2\sigma_1}{\tau_1\sigma_2}\right)\cosh(\tau_1 d)}{\cosh(\tau_1 d)+\left(\frac{\tau_2\sigma_1}{\tau_1\sigma_2}\right)\sinh(\tau_1 d)}\right\} \tag{9}$$

Making use of the fact that $\vec{J}$ and $\vec{H}$ are mutually perpendicular:

$$\vec{J}=\vec{n}\times\vec{H}$$

where : $\vec{n}$ is a unit vector perpendicular to the conductor surface and directed into the dielectric region.

This may be re-written in the form (Ramo, 1967):

$$J_z=-H_y|_{x=0}$$

Thus from the definition of surface impedance:

$$Z_S=\left.\frac{-E_{z1}}{H_{y1}}\right|_{x=0}=\left.\frac{-\frac{1}{\sigma_1}(C\sinh(\tau_1 x)+D\cosh(\tau_1 x))}{\frac{1}{\tau_1}(C\cosh(\tau_1 x)+D\sinh(\tau_1 x))}\right|_{x=0} \tag{10}$$

$$=-\frac{\frac{1}{\sigma_1}D}{\frac{1}{\tau_1}C}$$

$$=-\frac{\tau_1 D}{\sigma_1 C}$$

Therefore, from (9) and (10):

$$Z_S=-\frac{\tau_1}{\sigma_1}\cdot-\left\{\frac{\sinh(\tau_1 d)+\left(\frac{\tau_2\sigma_1}{\tau_1\sigma_2}\right)\cosh(\tau_1 d)}{\cosh(\tau_1 d)+\left(\frac{\tau_2\sigma_1}{\tau_1\sigma_2}\right)\sinh(\tau_1 d)}\right\}$$

Substituting for τ_1 and τ_2, the equation may be reduced to:

$$Z_S = \sqrt{\frac{\mu_1}{\sigma_1}}\sqrt{s}\left\{\frac{\sinh(\sqrt{\sigma_1\mu_1}\,d\sqrt{s}) + \sqrt{\frac{\sigma_1\mu_2}{\sigma_2\mu_1}}\cosh(\sqrt{\sigma_1\mu_1}\,d\sqrt{s})}{\cosh(\sqrt{\sigma_1\mu_1}\,d\sqrt{s}) + \sqrt{\frac{\sigma_1\mu_2}{\sigma_2\mu_1}}\sinh(\sqrt{\sigma_1\mu_1}\,d\sqrt{s})}\right\}$$

Substituting for the steady state value of s (ie $s = j\omega$):

$$Z_S = (1+j)\sqrt{\frac{\mu_1}{\sigma_1}}\sqrt{\pi f}\left\{\frac{\sinh((1+j)\sqrt{\sigma_1\mu_1}\,d\sqrt{\pi f}) + \sqrt{\frac{\sigma_1\mu_2}{\sigma_2\mu_1}}\cosh((1+j)\sqrt{\sigma_1\mu_1}\,d\sqrt{\pi f})}{\cosh((1+j)\sqrt{\sigma_1\mu_1}\,d\sqrt{\pi f}) + \sqrt{\frac{\sigma_1\mu_2}{\sigma_2\mu_1}}\sinh((1+j)\sqrt{\sigma_1\mu_1}\,d\sqrt{\pi f})}\right\}$$

However, in order to retain consistency, nomenclature first introduced by Nahman (1962) is utilised, ie:

$$K_i = \sqrt{\mu_i\sigma_i}$$

$$\therefore \quad Z_S(s) = \frac{K_1\sqrt{s}}{\sigma_1}\left\{\frac{\sinh(K_1 d\sqrt{s}) + \left(\frac{K_2\sigma_1}{K_1\sigma_2}\right)\cosh(K_1 d\sqrt{s})}{\cosh(K_1 d\sqrt{s}) + \left(\frac{K_2\sigma_1}{K_1\sigma_2}\right)\sinh(K_1 d\sqrt{s})}\right\} \qquad (11)$$

Equation (11) thus defines the internal impedance of the coated block. Note that this is the internal impedance for a unit length *and* unit width of a coated planar conductor. This term is often referred to as the *impedance per square* of a material. (An analysis similar to the preceding one may be conducted for both the inner *and* outer conductor.)

Consider, now, only the inner busbar. Clearly, equation (4) must be solved in general for the coating material (subscript *i1*) and the busbar itself (subscript *i2*). The thickness of the coating applied to the inner busbar is d_i (refer to *figure 12*).

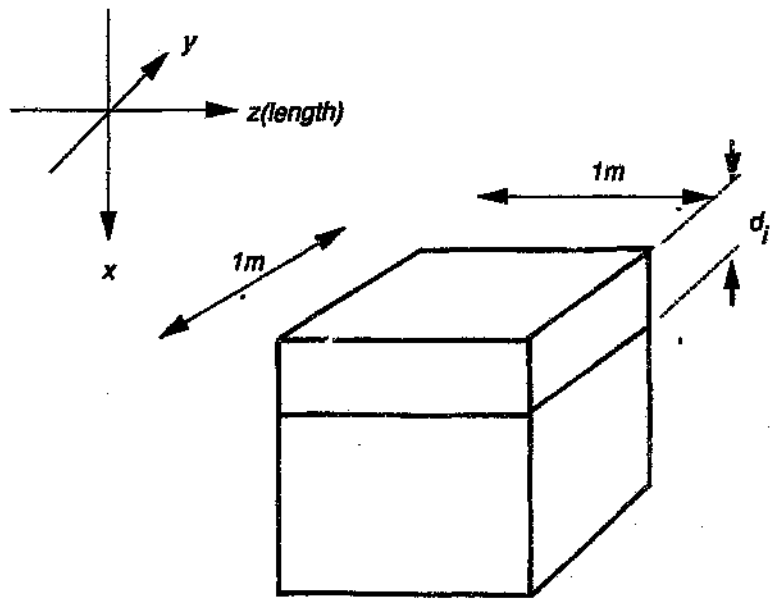


Figure 12 : A unit square of a coated flat conductor (inner busbar). The orientation of the cartesian co-ordinates will be retained throughout the discussion.

let:

$$\tau_{i1} = j\omega\mu_o\mu_{R_{i1}}\sigma_{i1}$$

$$\tau_{i2} = j\omega\mu_o\mu_{R_{i2}}\sigma_{i2}$$

For the coating, thickness d_i, the general solution is well known:

$$J_{zi1} = A_o e^{-\tau_{i1}x} + B_o e^{-\tau_{i1}x}$$

$$= A\sinh(\tau_{i1}x) + B\cosh(\tau_{i1}x) \qquad cf\,(5)$$

For the busbar itself:

$$J_{zi2} = Ce^{-\tau_{i2}x} \qquad cf\,(6)$$

For both materials:

$$E_z = \frac{J_z}{\sigma} \qquad cf\,(7)$$

$$H_y = \frac{1}{j\omega\mu_o\mu_R}\frac{dE_z}{dx} \qquad cf\,(8)$$

Once again, because tangential electric and magnetic fields are continuous across the boundary, the following boundary conditions apply:

$$F_{z_{11}} = E_{z_{12}}\big|_{x=d_i} \qquad H_{y_{11}} = H_{y_{12}}\big|_{x=d_i}$$

and:

$$I_z = -H_y\big|_{x=0}$$

Hence it may be shown that, for the inner conductor, coated with a material of thickness d_i:

$$Z_{Si} = \frac{E_w}{I_z} = -\frac{E_z\big|_{x=0}}{I_z} = -\frac{E_z}{H_y}\Big|_{x=0}$$

$$= -\frac{\frac{1}{\sigma_{i1}}B}{\frac{1}{\tau_{i1}}A} \qquad cf\,(10)$$

In accordance with *figure 9* and the discussion contained in this chapter, the inner and outer conductor, both of which have different widths in a co-axial system, must be accounted for. Thus, in the same manner as above, the internal impedance per square of the outer grounded enclosure may be determined.

For the inner conductor:

$$Z_{Si}(s)$$

For the outer grounded enclosure:

$$Z_{Sg}(s)$$

Thus a further subscript, g, has been introduced to indicate the outer grounded enclosure. (We shall continue to use subscript *1* to refer to the coating and subscript *2* to refer to the substrate.)

It is accepted in transmission line theory that all attributes of the line be expressed per unit length. Consequently, in order to obtain a value of conductor internal impedance per unit length ($z(s)$), we must divide the internal impedance per unit length and width by the conductor width. Furthermore, the internal impedance is the sum of the contributions of the inner and outer conductors (as noted earlier):

$$\therefore \quad z(s) = z_i(s) + z_g(s)$$

where : (due to effectively placing in parallel the number of internal impedance terms per unit square)

$$z_i(s) = \frac{Z_{Si}(s)}{2\pi r_i}$$

$$= \frac{Z_{Si}(s)}{2\pi r_{i1}}$$

$$z_g(s) = \frac{Z_{S_g}(s)}{2\pi r_g}$$

$$= \frac{Z_{S_g}(s)}{2\pi r_{g1}}$$

and:

$$Z_{Si}(s) = \frac{K_{i1}\sqrt{s}}{\sigma_{i1}} \left\{ \frac{\sinh(K_{i1} d_i \sqrt{s}) + \left(\frac{K_{i2}\sigma_{i1}}{K_{i1}\sigma_{i2}}\right) \cosh(K_{i1} d_i \sqrt{s})}{\cosh(K_{i1} d_i \sqrt{s}) + \left(\frac{K_{i2}\sigma_{i1}}{K_{i1}\sigma_{i2}}\right) \sinh(K_{i1} d_i \sqrt{s})} \right\}$$

$$Z_{S_g}(s) = \frac{K_{g1}\sqrt{s}}{\sigma_{g1}} \left\{ \frac{\sinh(K_{g1} d_g \sqrt{s}) + \left(\frac{K_{g2}\sigma_{g1}}{K_{g1}\sigma_{g2}}\right) \cosh(K_{g1} d_g \sqrt{s})}{\cosh(K_{g1} d_g \sqrt{s}) + \left(\frac{K_{g2}\sigma_{g1}}{K_{g1}\sigma_{g2}}\right) \sinh(K_{g1} d_g \sqrt{s})} \right\}$$

$z(s)$ is thus the internal impedance of a co-axial system in Ω/m. It is now pertinent to introduce one further level of reduction prior to establishing the propagation factor of the system incorporating the skin effect:

$$z(s) = \frac{K_{i1}\sqrt{s}}{2\pi\sigma_{i1} r_{i1}} \left\{ \frac{1 - A_i e^{-B_i\sqrt{s}}}{1 + A_i e^{-B_i\sqrt{s}}} \right\} + \frac{K_{g1}\sqrt{s}}{2\pi\sigma_{g1} r_{g1}} \left\{ \frac{1 - A_g e^{-B_g\sqrt{s}}}{1 + A_g e^{-B_g\sqrt{s}}} \right\}$$

where:

$$A_i = \frac{\left(1 - \frac{K_{i2}\sigma_{i1}}{K_{i1}\sigma_{i2}}\right)}{\left(1 + \frac{K_{i2}\sigma_{i1}}{K_{i1}\sigma_{i2}}\right)} \qquad B_i = 2K_{i1}d_i \qquad K_{ix} = \sqrt{\mu_{ix}\sigma_{ix}}$$

$$A_g = \frac{\left(1 - \frac{K_{g2}\sigma_{g1}}{K_{g1}\sigma_{g2}}\right)}{\left(1 + \frac{K_{g2}\sigma_{g1}}{K_{g1}\sigma_{g2}}\right)} \qquad B_g = 2K_{g1}d_g \qquad K_{gx} = \sqrt{\mu_{gx}\sigma_{gx}}$$

We can now define the impedance ($Zd(s)$) and admittance ($Yd(s)$) per unit length of a co-axial busduct with the conductors coated with a conductive material:

$$Zd(s) = Rd + s \cdot Ld + z(s) \quad [\Omega/m] \qquad Yd(s) = Gd + s \cdot Cd \quad [S/m]$$

and: (12)

$$Ld = \frac{\mu_o}{2\pi}\ln\left(\frac{r_{g1}}{r_{i1}}\right) \quad [H/m] \qquad Cd = \frac{2\pi\varepsilon_o\varepsilon_R}{\ln\left(\frac{r_{g1}}{r_{i1}}\right)} \quad [F/m]$$

where : ε_R is the relative permittivity of the medium between the conductors.

Gd is the conductance per unit length between the conductors. For a gaseous dielectric such as SF_6 this term is considered to be zero.

The term *Rd* is valid only at DC. The transition from this term to $z(s)$ is discussed in *appendix 6*. It is thus apparent that equation (12) has differing forms at various frequencies. The way it is presented here is thus acceptable only when this is noted. Its various forms over a range of frequencies is discussed in *chapter 6* as well.

It is also important to note that *Ld* and *Cd* are *external* impedance terms, as they are in no way affected by the actual characteristics of the conductor materials - in contrast to the term $z(s)$.

Thus the propagation factor, $\gamma(s)$, may be determined in terms of $Zd(s)$ and $Yd(s)$, giving α, the attenuation factor, and β, the phase factor. ie:

$$\gamma(s) = \sqrt{Zd(s) \cdot Yd(s)}$$

$$= \sqrt{(Rd + s \cdot Ld + z(s)) \cdot (s \cdot Cd)}$$

and

$$\Re\{\gamma(s)\} = \alpha \quad [Neper/m] \qquad \Im\{\gamma(s)\} = \beta \quad [radians/m]$$

Therefore, in terms of the nomenclature introduced above, we may define in full the propagation factor (equation (13)). Note that, once defined, this factor allows us to determine the frequency transfer characteristic of any length of our now defined co-axial system. The propagation factor now also includes the effects of various coatings independently defined for the two conductors. It is not the purpose of this work to detail the solution to the next equation. It is, however, obvious that its solution is utilised in the program *Skin* discussed in *appendix 5*.

$$\gamma(s)=\sqrt{\left(Rd+s\cdot Ld+\frac{K_{i1}\sqrt{s}}{2\pi\sigma_{i1}r_{i1}}\left\{\frac{1-A_i e^{-\beta_i\sqrt{s}}}{1+A_i e^{-\beta_i\sqrt{s}}}\right\}+\frac{K_{g1}\sqrt{s}}{2\pi\sigma_{g1}r_{g1}}\left\{\frac{1-A_g e^{-\beta_g\sqrt{s}}}{1+A_g e^{-\beta_g\sqrt{s}}}\right\}\right)(s\cdot Cd)}} \qquad (13)$$

Thus the term $z(s)$ can be used to account for both the simple skin effect, and the effect introduced by the application of various coatings to the busbar and/or grounded enclosure.

We have therefore established an equation for the impedance per unit length of a transmission line consisting of two coated planar conductors. Clearly, the four materials may have differing properties, and it is these properties that define ultimately the characteristic impedance of the system.

One final point to note is that equation (13) must be programmed in order to accurately model four distinct cases ((13) being for the most general case):

- Both conductors coated
- Inner conductor only coated
- Outer conductor only coated
- Neither conductor coated

The data requirements for the *Pascal* programme *Skin*, based on this model, are presented in *appendix 5*. It should be noted that the required data all pertains to the physical characteristics of the system. The electric nature of the system is derived directly from this physical data.

4.4.5 Correcting the Error in the Planar Model

As previously noted, *Rd* represents the internal impedance term for the special case - DC. The transition from *Rd* to the real component of $z_i(s)$ is defined in terms of modified Bessel functions for the busbar, and modified Hankel functions for the outer grounded enclosure in the exact solution. The following equation is used to define the internal impedance in the cylindrically defined system (Ramo, 1967) (This is fully discussed in *appendix 6*):

$$\Re\{z(s)\}=\sqrt{\frac{\pi f\mu}{\sigma}}\frac{1}{\sqrt{2}\pi r_i}\left\{\frac{Ber\left(\frac{\sqrt{2}r_i}{\delta}\right)Bei'\left(\frac{\sqrt{2}r_i}{\delta}\right)-Bei\left(\frac{\sqrt{2}r_i}{\delta}\right)Ber'\left(\frac{\sqrt{2}r_i}{\delta}\right)}{\left(Ber'\left(\frac{\sqrt{2}r_i}{\delta}\right)\right)^2+\left(Bei'\left(\frac{\sqrt{2}r_i}{\delta}\right)\right)^2}\right\} \qquad (14)$$

where : the symbols have their usual significance (Relton, 1965).

Hence, with this term omitted in equation (3), an 11% error in the real component of $z(s)$ for a typical section of high voltage busduct ($r_i = 55 \times 10^{-3}$m, $r_s = 200 \times 10^{-3}$m) is produced at 50 Hz. This error has decreased to less than 5% at 250 Hz. In fact, the accuracy of the planar model of a coaxial system is a function of the ratio of the busbar radius (r_i) to the skin depth at a particular frequency. Hence, in the graphs shown in *appendix 6*, this ratio is indicated at the various frequencies (Refer to *figure 13*).



Figure 13 : Comparison of planar and bessel solution for $\frac{r_i}{\delta} = 5$, f = 59,76 Hz and $\delta = 0,011$m.

Since the model relies for its validity upon the establishment of TEM mode waves, the highest useful frequency is also set by the dimensions of the busduct. In the same high voltage busduct, first order TE mode waves would occur above 375 MHz. From the solution defined in equation (14) a correction factor, ζ, to be incorporated into Rd may be determined. This optimises the accuracy of the planar solution. The correction factor ζ is found from:

$$\Re\{z(s)\}_{\text{Bessel}} = \zeta \cdot Rd + \Re\{z(s)\}_{\text{planar}}$$

It is shown in *appendix 6* that a value of $\zeta = 0,256$ is recommended.

Thus the frequency domain portion of the model is based on well established theory, and the inclusion of coatings and two independently defined conductors with distinctly different characteristics is not to be expected to introduce significant inaccuracies. Furthermore, errors associated with the transition from the DC resistance value, Rd, to the real component of $z(s)$ are easily accounted for in the manner discussed above and in *appendix 6*.

4.5 Experimental Verification of the Model

The model was experimentally tested in the time domain using scaled down test ducts. Scaled down systems were used:

- To enhance the expected attenuating effects
- To allow a relatively long length of duct with no discontinuities to be used in order to both enhance the effect and avoid reflections not accounted for in the simulation
- For simplicity, and the ability to produce an easily controlled pulse

The initial tests were conducted by considering the response of the system to a carefully controlled pulse of short duration. The reason for basing these tests on a pulse were largely that the reflection off a voltage transformer (a VT essentially being represented by a capacitor at these high frequencies) has the very spiky characteristic shown in *figure 14*. This effect is explained pictorially in *figure 15*. Furthermore, since the model should faithfully model a wide frequency band, the pulse includes a wide frequency spectrum.

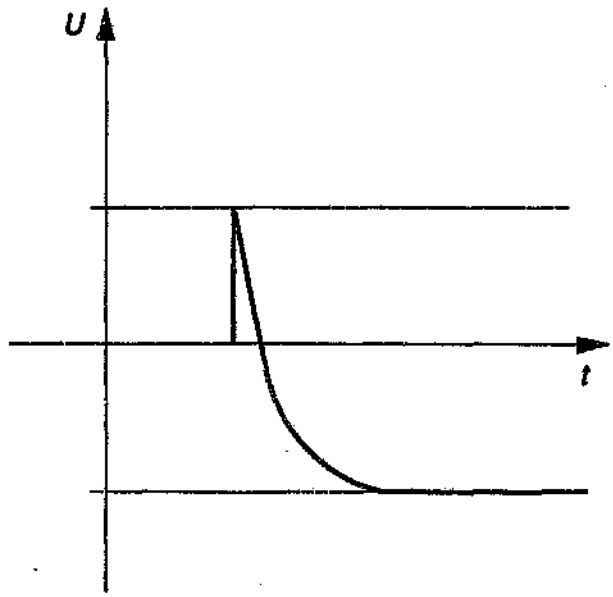


Figure 14 : An idealised reflection off a voltage transformer which behaves like a purely capacitive impedance for very short time periods.

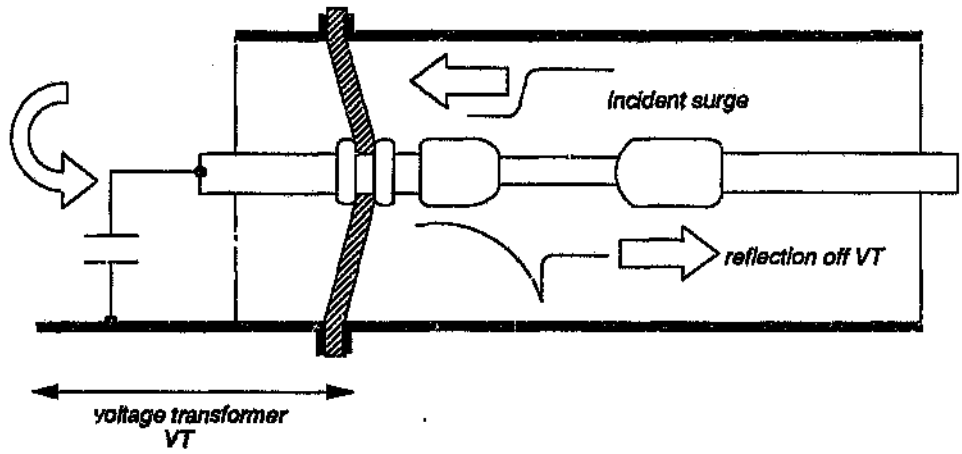


Figure 15 : Reflection off a voltage transformer, showing the distinctive pulse-like nature of the reflected surge.

This type of reflection is largely responsible for the high frequency content of typical VFTs, and it was thus important to include as the first example the time domain performance of such a pulse. The Fourier series of the pulse was determined as per *appendix 7*. Note the inherent periodicity of the waveform.

To verify the accuracy of the model, four different experiments were conducted using a 50Ω measuring circuit with a 400MHz bandwidth. The same experimental set-up was used in all the experiments, and is represented in *figure 16*.

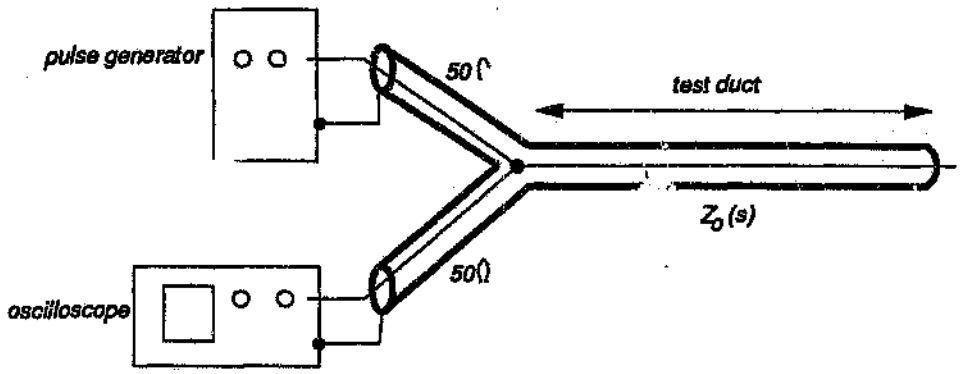


Figure 16 : The experimental set-up used in order to verify the operation of the model. The test duct was 6m in length

The simulation accounted for reflections introduced at the junction of the measuring circuitry and the test line:

- Prediction of the performance of a scaled down busduct fabricated entirely from aluminium
- Prediction of the performance of a scaled down busduct fabricated entirely from mild steel
- Prediction of the performance of a scaled down busduct with a copper busbar and an aluminium grounded enclosure
- Prediction of the performance of a scaled down busduct with a copper busbar coated with a 20μm layer of nickel and an aluminium grounded enclosure

The physical dimensions and parameters of all the tested systems are included in *appendix 8*, and noted on the theoretical prediction plots in that appendix and in this chapter. The techniques used to establish the physical parameters are detailed in *appendix 12*.

Although neither of the first two test involved coatings, they are to be considered important since they allowed the model to be assessed for materials with widely differing values of conductivity and permeability. The third experiment tested the operation of the model with different materials for the busbar and outer grounded enclosure. The final experiment is most significant, since it tests all of the above-mentioned, as well as the effect of a coating on the accuracy of the model.

In conducting these experiments, the objective was clear and as outlined above. However, the results, which demonstrated clearly the accuracy of the model, also lead to the identification of a number of important considerations, which will be more thoroughly dealt with later. The results and the corresponding predictions are tabulated in *table 3*. It is clear that the model is sufficiently accurate to allow a theoretical study of the effects of coated busbars on the attenuation of VFTs.

Table 3 : Predicted and recorded pulse responses.

System description	Predicted percentage (peak) of pulse returned	Recorded percentage (peak) of pulse returned
Solid aluminium busbar supported within an aluminium grounded enclosure	98	97
Solid mild steel busbar supported within an mild steel grounded enclosure	86	84
Solid copper busbar supported within an aluminium grounded enclosure	99	99
Solid copper busbar coated with a 20μm thick nickel layer supported within an aluminium grounded enclosure	94	95

As mentioned previously, there is a mismatch between the generator and the system under test. However, this is easily accounted for. While the characteristic impedance of the system under test was simply calculated (ignoring frequency dependent effects), the correctness of the value used in the assumptions was verified by terminating the system under test with a radially arranged resistor network of precisely that value. Furthermore, as a short circuit termination gives a more defined (but inverted) response, the busbar end was alternately open and short circuited. No measurable difference in the magnitude of the returned pulse was observed. Consequently a non-inverted response was preferred as it could be captured on a single display with sufficient resolution and greater significant accuracy than the inverted response. The photographic record of the results for these tests is shown in *figure 17*. Also shown are the predicted responses, as well as the corresponding frequency domain transfer characteristic for the system. In examining these, care must be exercised in the interpretation of the photographic results in accordance with the earlier discussion. A full experimental record is included in *appendix 8*.

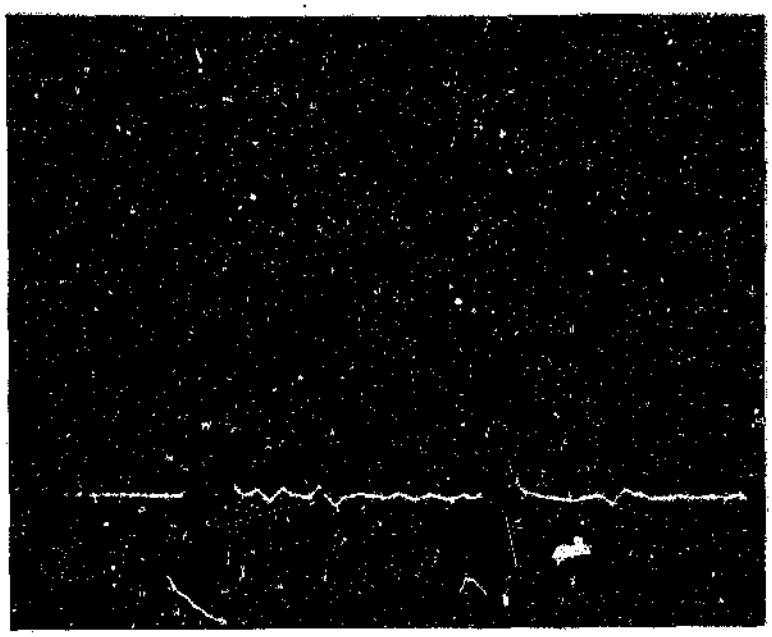


Figure 17a : Photographic record of pulse attenuation within a 12 m length of scaled down busduct fabricated entirely from aluminium. Scales: 10ns per large division; 400mV per large division.

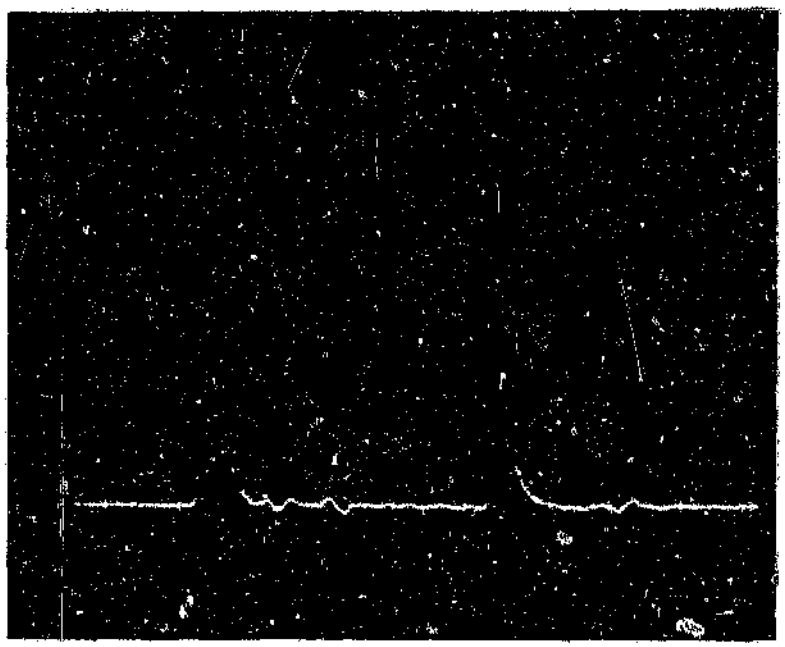


Figure 17b : Photographic record of pulse attenuation within a 12 m length of scaled down busduct fabricated entirely from mild steel. Scales: 10ns per large division; 400mV per large division.

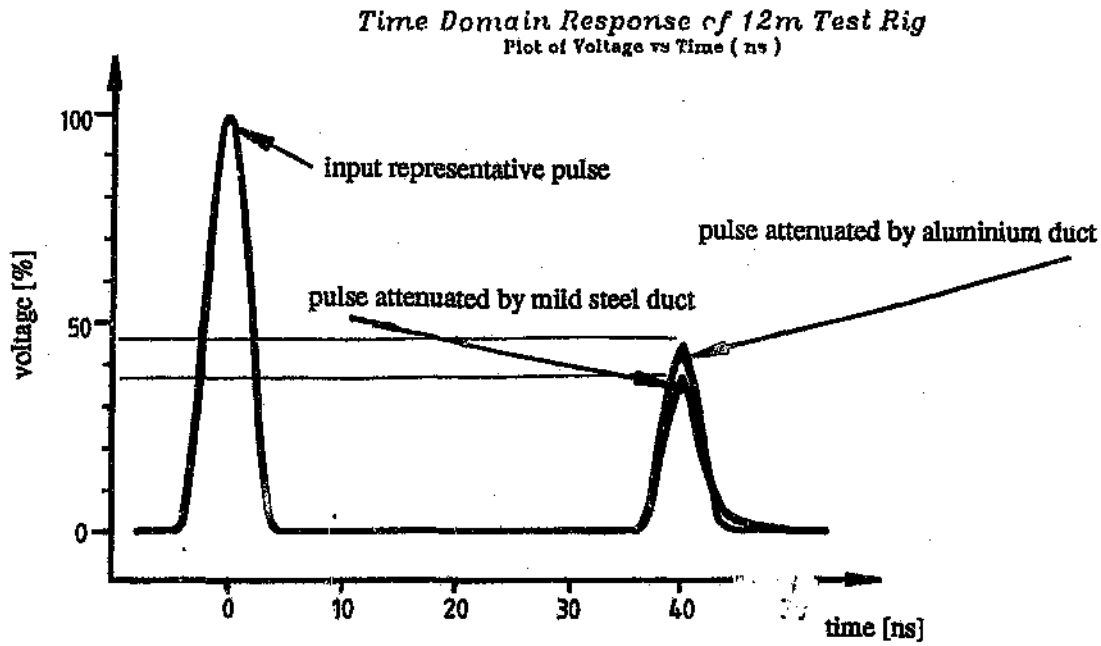


Figure 17c : Predicted pulse attenuation within a 12 m long mild steel and a 12 m long aluminium system. For both systems $r_i = 5$ mm and $r_e = 22{,}5$ mm.

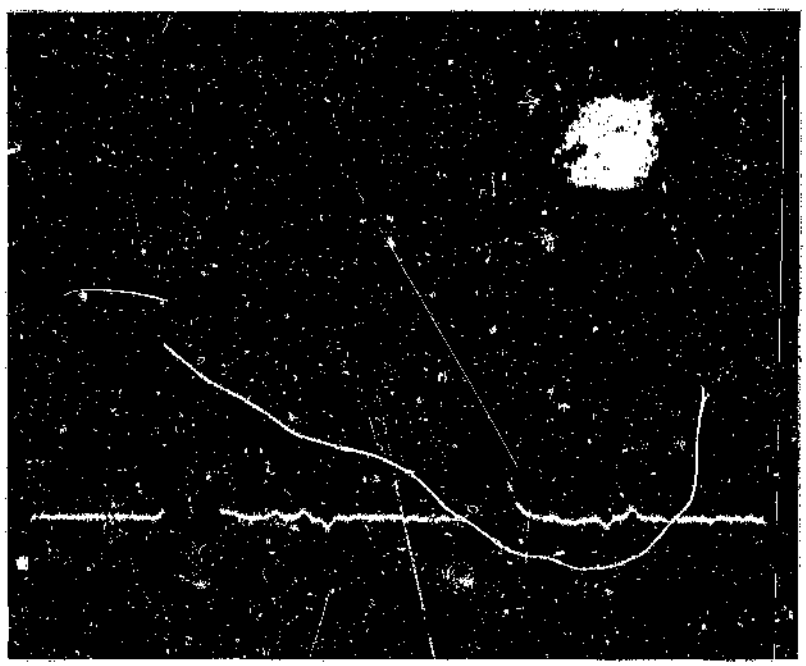
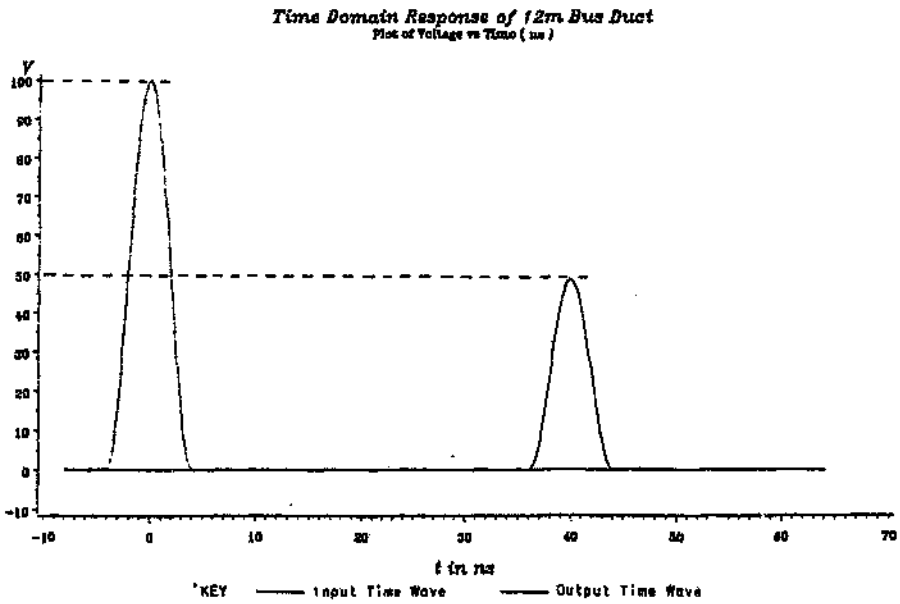


Figure 17d : Photographic record of pulse attenuation within a 12 m length of scaled busduct. Busbar fabricated from copper, $\sigma = 5{,}8 \times 10^7 [S/m]$. Outer grounded enclosure fabricated entirely from aluminium, $\sigma = 3{,}54 \times 10^7 [S/m]$. $r_i = 6{,}11$ mm, $r_e = 22{,}1$ mm. Scales: 10ns per large division; 400mV per large division.



Output of program SKIN

Figure 17e : Pulse attenuation within a 12 m length of scaled busduct. Busbar fabricated from copper, $\sigma = 5,8 \times 10^7 [S/m]$. Outer grounded enclosure fabricated from aluminium, $\sigma = 3,54 \times 10^7 [S/m]$. $r_i = 6,11$ mm, $r_g = 22,1$ mm.

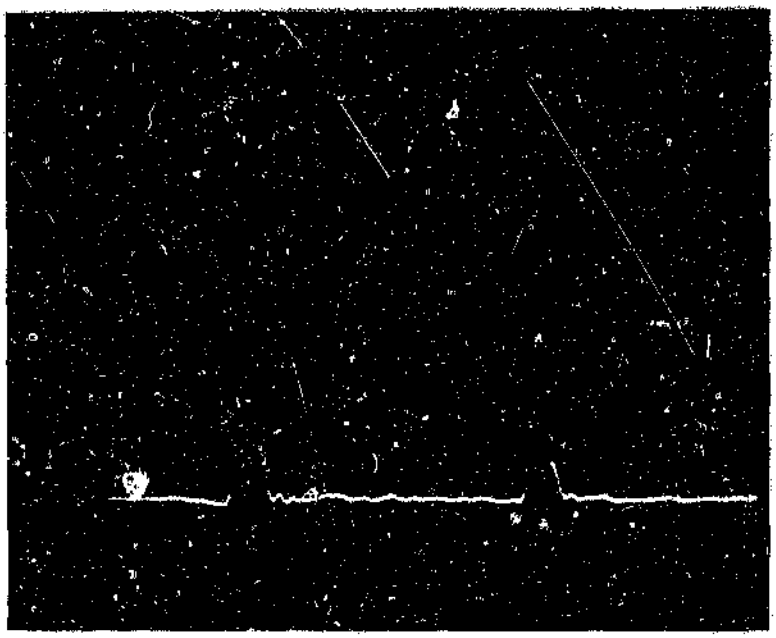
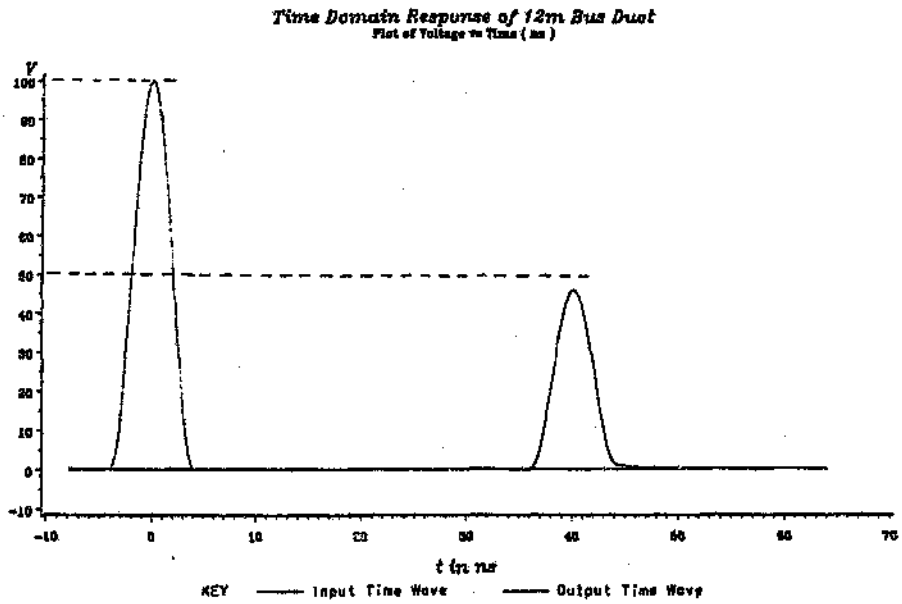


Figure 17f : Photographic record of pulse attenuation within a 12 m length of scaled busduct. Busbar fabricated from copper, $\sigma = 5,8 \times 10^7 [S/m]$. Busbar coated with a $20 \mu m$ layer of nickel, $\sigma = 1,4 \times 10^7 [S/m]$, $\mu_R = 50$. Outer grounded enclosure fabricated from aluminium, $\sigma = 3,54 \times 10^7 [S/m]$. $r_i = 6,11$ mm, $r_g = 22,1$ mm. Scales: 10ns per large division; 400mV per large division.



Output of program SKIN

Figure 17g : Pulse attenuation within a 12 m length of scaled busduct. Busbar fabricated from copper, $\sigma = 5,8 \times 10^7 [S/m]$. Busbar coated with a 20μm layer of nickel, $\sigma = 1,4 \times 10^7 [S/m]$, $\mu_R = 50$. Outer grounded enclosure fabricated from aluminium, $\sigma = 3,54 \times 10^7 [S/m]$. $r_i = 6,11$ mm, $r_g = 22,1$ mm.

The assessment of the results, and particular the conclusion drawn from the initial results with ferromagnetic material, made it clear that the effect of permeability was vital. Thus, since it is used as a constant in the model, its choice is important. It must be remembered that a ferromagnetic has an initial permeability ($\mu_R = \mu_i$, Rayleigh region), a maximum permeability ($\mu_R = \mu_M$), and a high field permeability ($\mu_R = \mu_S$), as shown in *figure 18*.

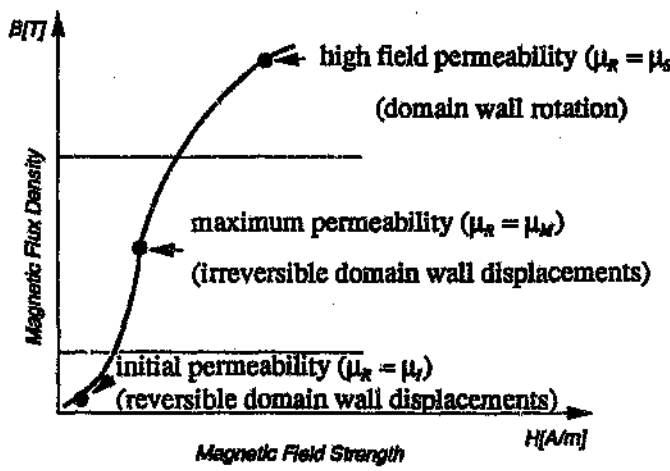


Figure 18 : Virgin B-H curve of a typical ferromagnetic. The figure shows the definition of μ_i, μ_M and μ_S.

The effects of permeability will be more fully dealt with in *chapters 5* and *6*.

Chapter 5 : Use of the Mathematical Model to Predict the Performance of Various Coating Materials

5.1 Background

In the study upon which the concluding remarks of this chapter are based, the philosophy was to identify the two most important waveforms likely to result in a VFT, and to consider the theoretical effect of coatings on their transmission along a typical high voltage busduct. The duct chosen was a BBC BG-2 type, with dimensions $r_i = 55\text{mm}$, $r_g = 200\text{mm}$. A length of 15m was selected as a suitable example as this was considered to be fairly representative of the distance between a disconnector and the SF_6 substation outer wall (Edlinger et al, 1984).

5.2 Formation of a VFT.

It must be noted that VFTs are made up from the time domain sum of numerous surge voltages that have been transmitted through the system from the disconnector switch to the observation point as suggested in *figure 19*.

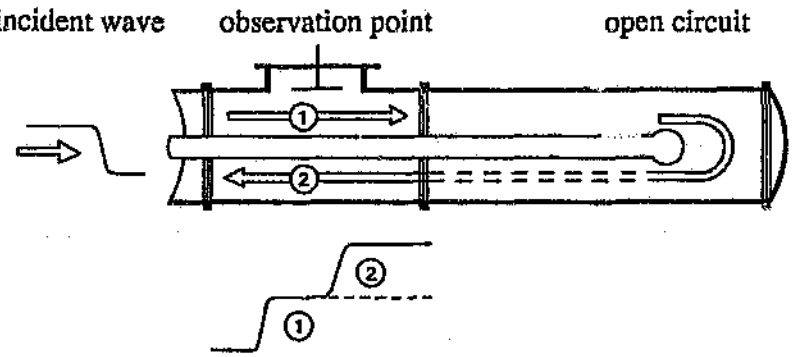


Figure 19 : The addition of the time domain components in order to build up the VFT recorded at a particular point in a GIS.

While the travelling wave phenomena will be more formally discussed in *chapter 6*, it is pertinent to briefly outline the formation of a VFT:

The incident surge shown in *figure 19* is one of the two surges developed by the operation of a disconnector. As it propagates within the duct, it passes the observation point, and is recorded for the first time, and is labelled voltage step 1 in the figure. (This is considered to constitute a single "path" between the source and observation point for this system.) The surge continues to propagate, and would then be reflected at the open circuit, whereupon it passes the observation point travelling in the opposite direction (in this case) and is recorded for the second time. (Again, the travel from the source to the observation point is considered a "path" in this model.)

At the measuring point, the two recordings are superposed to give the waveform indicated, representing the VFT over this short time interval.

Consequently, the nett attenuation of any observed VFT is clearly dependent on the sum of the effects introduced to the componental surges - not to any gross effect introduced to the VFT as an entity. Attention was therefore paid to the transmission of a surge voltage along the duct.

As was noted in *chapter 3*, the highest frequency component associated with a VFT is due to the rising edge of the voltage surge. The high frequency content of a typical VFT is therefore significant. This is illustrated in *figure 20*, which is a copy of *figure 3* of *chapter 2*. Furthermore, the reflection from a voltage transformer (modelled as a capacitor to earth) has a particularly significant spiky nature. These spikes are known to contribute significantly to the peak magnitude of VFTs (Boeck, 1987). This effect is shown in *figure 21*.

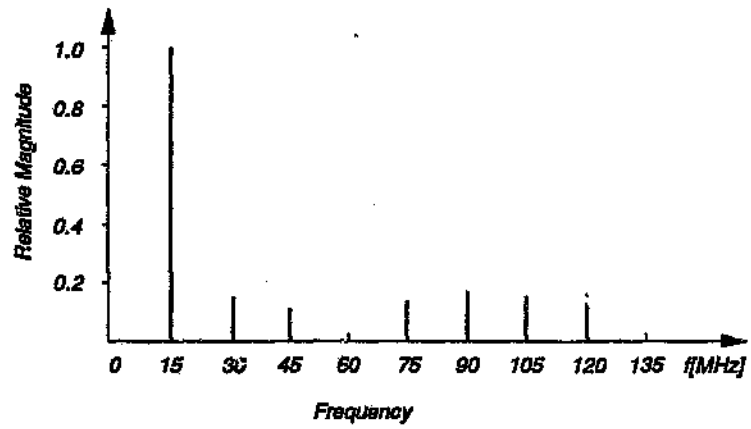


Figure 20 : Harmonic content of a typical VFT with a fundamental oscillation frequency of 15 MHz. The DC component has been suppressed in the analysis (Reynders, 1987b).

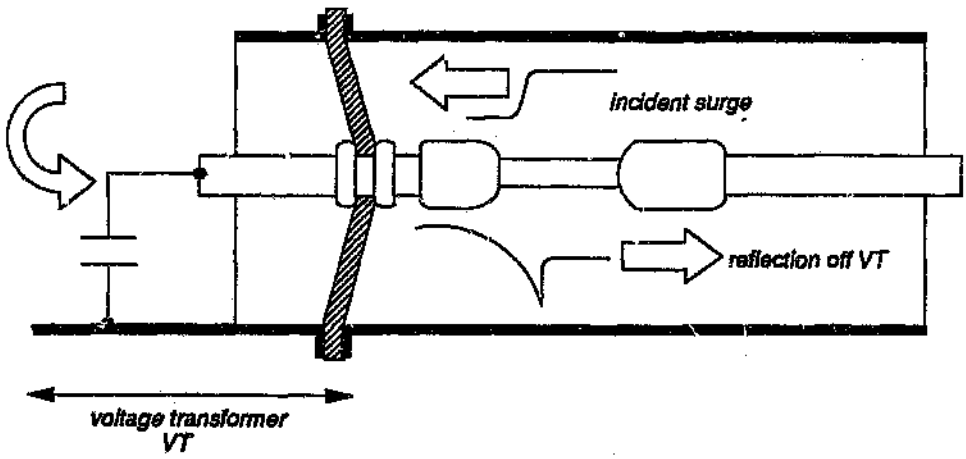


Figure 21 : Reflection off a voltage transformer, showing the distinctive pulse-like nature of the reflected surge.

5.3 Theoretical Study

Consequently, the objective of this theoretical study was to:

- Observe the effects of coatings upon the risetime of a surge and the peak magnitude of a pulse
- Gain an understanding of the relative effects of various material parameters upon the attenuation
- Draw conclusions pertaining to optimum coating characteristics

Recall that for this study, all the parameters shown in *figure 22* below may be controlled, as may the length of the duct for the time domain study. Furthermore, since μ_R is used as a constant within the program, its choice is important, and motivates the use of a range of μ_R values in the study.

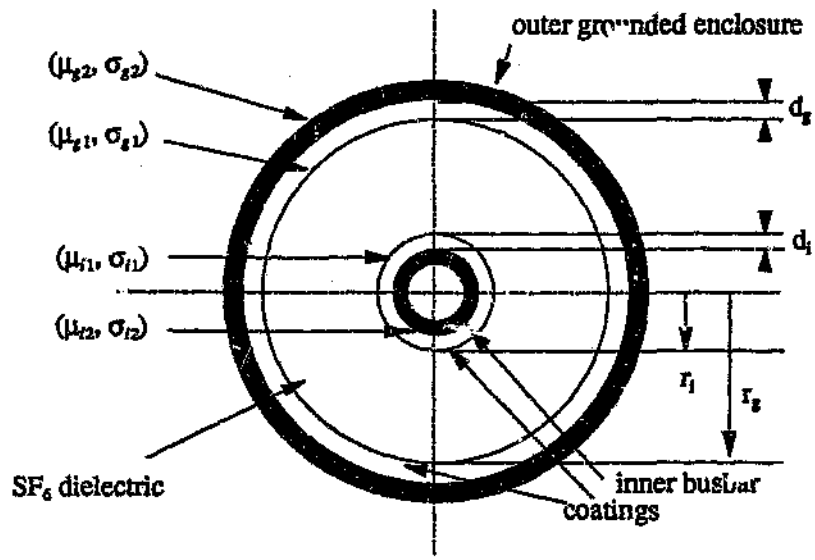


Figure 22: Cross-sectional representation of the busduct with coatings, clearly indicating all the variables accepted by the model. The figure also serves to define the variables used in this thesis. Particular attention should be paid to the use of subscripts.

5.3.1 Predicted Performance

The two most important frequency ranges associated with disconnect transients are evident from *figure 23*. The higher frequency range is determined by the initial step, a characteristic of the mechanism of breakdown in the gap. Hence this range typically falls between 50 and 120MHz. The second is the slower damped oscillation, dependent upon reflection and transmission of the initial surges within the GIS. Note that the slower damped oscillation, because it is a function of system configuration, cannot be directly affected by this technique.

The application of coatings attenuates only the waveform travelling along the duct. The form of the observed VFT is location-dependent and made up of numerous components. This oscillating frequency is therefore a function of the specific GIS configuration, and is shown to be 15MHz for the system in which the transient of the above figure was recorded. Although these transients are also known to cause oscillations of frequencies below a few hundred kHz and well above 100Mhz (Reynders, 1987b; Boeck, 1987), the main component of the order of some MHz and the superimposed component of some tens of MHz are known to define the most detrimental features.

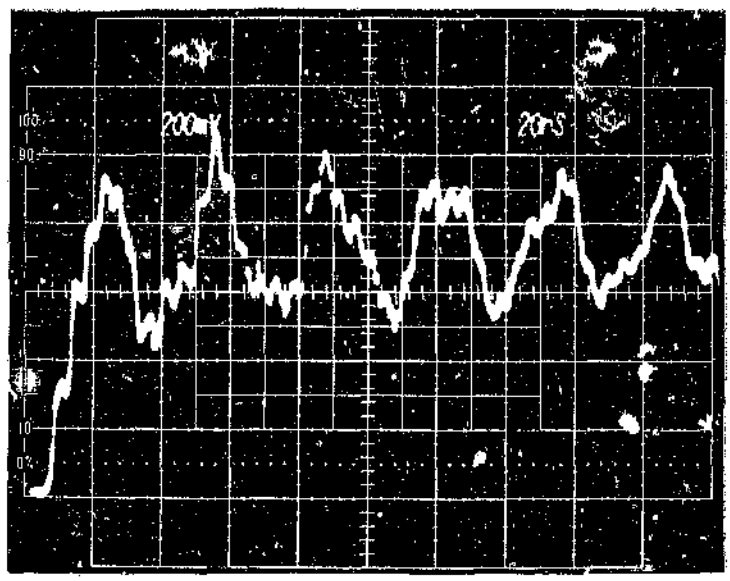


Figure 23 : A VFT recorded in the Werner von Siemens Test Facility at the University of the Witwatersrand clearly showing two distinct frequency components. The system in which this VFT was recorded is identical to that used in *figure 4*. Scales: 40ns per large division; 90,8kV per large division.

The frequency domain performance of three typical high voltage busducts is shown in *figure 24*, where the busbars and grounded enclosures are fabricated from uncoated aluminium. *Figure 25* considers the frequency response when the busbar and outer grounded enclosure are coated with a 50μm layer of a stainless steel, 3CR12. In generating this plot, a value of $\mu_R = 1000$ (μ_M) has been used. Refer to *figure 18*, where μ_r, μ_M and μ_S are defined. The upper dotted line shows the frequency response if the entire busbar was fabricated from 3CR12, while the lower dotted line shows the response for the aluminium system. (The physical parameters of these materials are to be found in *table 4*.)

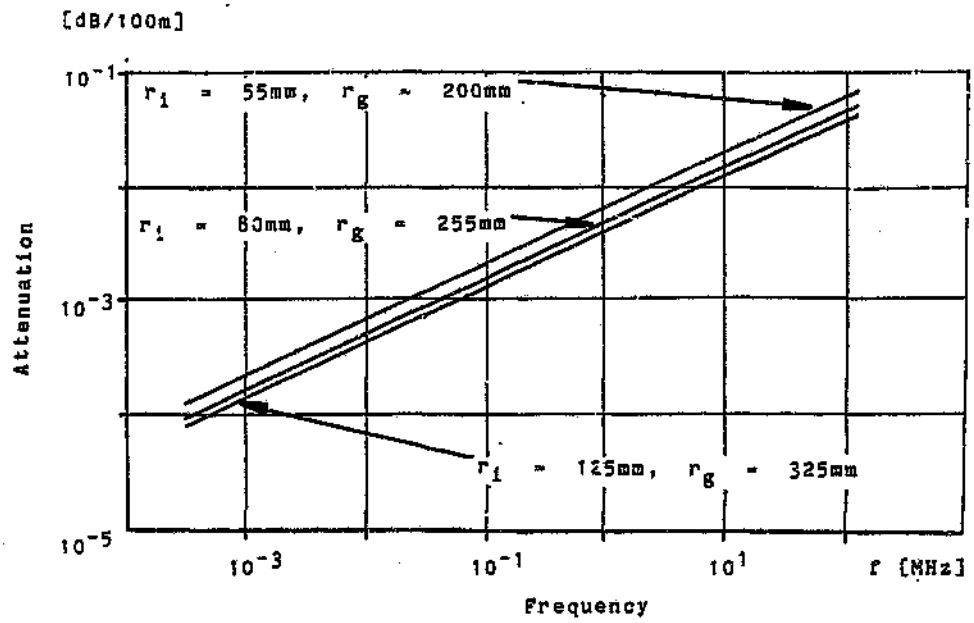


Figure 24 : Attenuation characteristic of three common high voltage busducts.

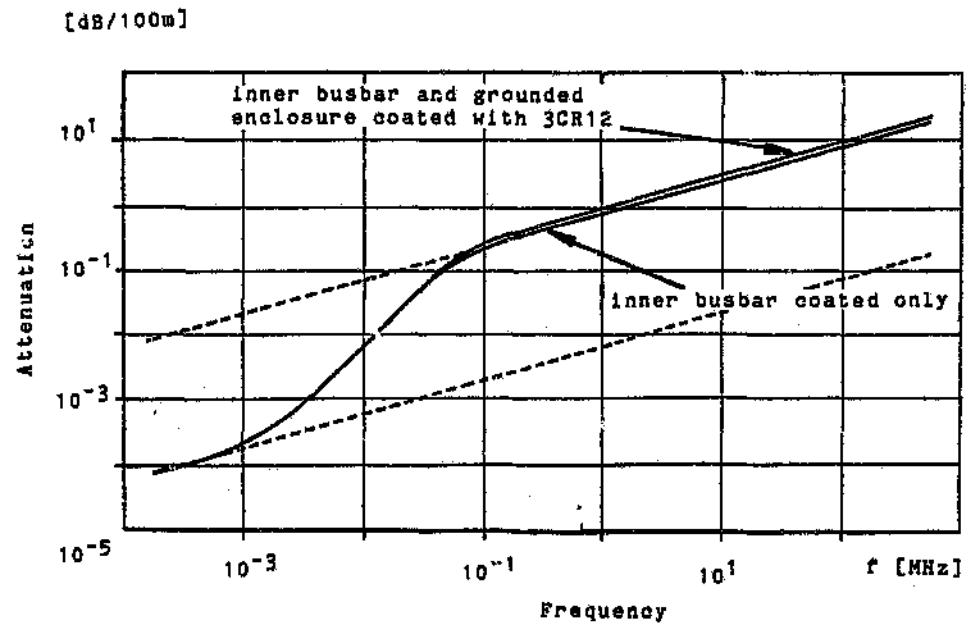


Figure 25 : Attenuation characteristic of a busduct with a 50µm thick skin of 3CR12 applied. A value of $\mu_R = \mu_M = 1000$ has been used. The upper dotted line shows the characteristic if the entire busbar was fabricated from 3CR12, while the lower dotted line shows the response for the aluminium busbar.

As can be seen from *figure 25*, the increased effective cross-sectional area of the grounded enclosure reduces its series resistance to such an extent that the effect of coating it has negligible influence upon the increased attenuation characteristic. Consequently, for all the subsequent predictions, the application of coatings to only the busbar has been considered.

It must be borne in mind that, as this study is effectively based on a steady state model, the transient nature of the skin effect is excluded. Once again, it becomes important to consider a range of μ_R values, as no transient model has yet been developed that accurately accounts for all the effects introduced by a ferromagnetic. The importance of this study is thus to carefully analyse the effects of these controllable parameters. The predicted performances for a typical high voltage busduct have been tabulated in *table 4*. *Figure 26* shows the attenuation introduced to such a pulse for a coating material with the characteristics of 3CR12. Consideration is given to values of μ_R.

Table 4 : Percentage attenuation of a representative pulse for different materials and different field intensities.

Material	Conductivity [S/m]	Relative Permeability			Coating Thickness	Percentage Attenuation		
		μ_r	μ_R	μ_M	[μm]	μ_r	μ_R	μ_M
Commercial Iron	1×10^7	150	660	5000	129	1,8	3,8	9,5
Permalloy	1×10^7	1200	400	250×10^3	65	6,9	4,1	59,8
Nickel	$1,4\times10^7$	110	200	600	128	1,3	1,8	3,0
Mild Steel	1×10^7	120	650	2000	145	1,6	3,7	6,3
Pure Iron	1×10^7	10000	660	200×10^3	16	13,1	3,8	45,1
Supermalloy	$1,6\times10^6$	100×10^3	240	-	13	63,5	5,6	-
Vanadium Permendur	$3,8\times10^6$	800	730	4500	91	6,5	6,4	14,2
Alperm	7×10^6	3000	240	35000	109	25,0	8,5	67,1
3CR12	$1,8\times10^6$	-	-400	-1000	346	-	6,9	10,8
Hypothetical Materials								
(a)	200	110	-	-	33900	89,8	-	-
(b)	200	10000	660	-	3350	99,0	96,1	-
(c)	7×10^5	120	650	2000	549	6,0	13,4	21,0
(d)	1×10^6	120	650	2000	4590	37,6	64,2	80,5

Consider a 275kV three phase system. If the initial surge reaches 0,3pu, this would imply an initial surge of magnitude 67kV travelling within the duct. With a 75Ω surge impedance, a peak transient current of 0,9kA would occur. Hence the initial step could initiate a peak magnetic field intensity of $2600A \cdot m^{-1}$ at the surface of the inner busbar. This value is then used to determine the high field permeability value of μ_R for the pulse attenuation evaluation.

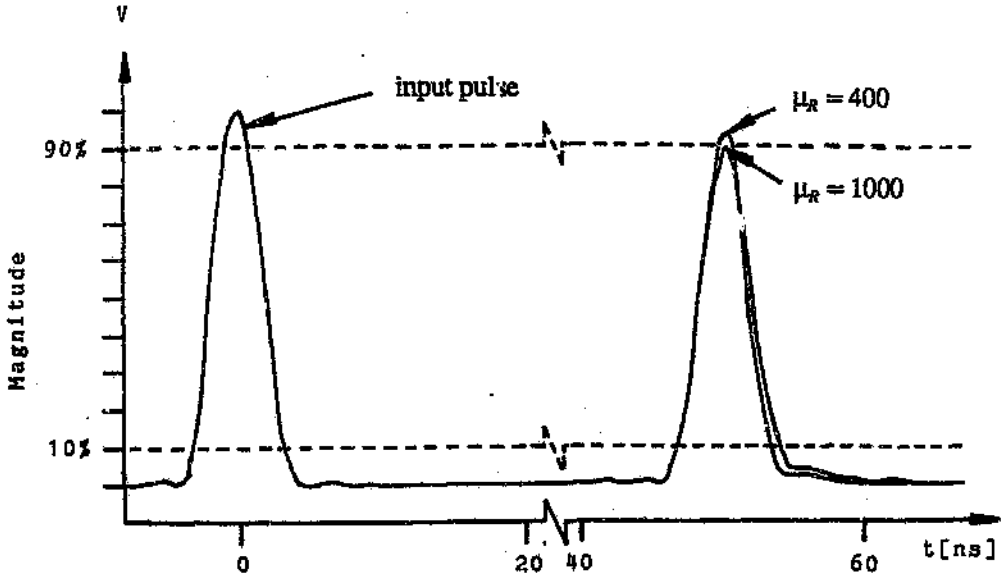


Figure 26 : Pulse attenuation with a skin of 3CR12 stainless steel 50µm thick. Duct dimensions : r_i = 55mm, r_s = 200mm, length = 15m.

However, such a pulse contains numerous frequency components of relevant magnitude well above the frequency range of interest in this discussion, and consequently the degradation of the rising edge of a typical surge voltage has also been considered. Remember that the initial surges determine the maximum *dV/dt* of the transient, and by reflection and transmission, develop the peak overvoltage within any GIS. The degradation of the rising edge as the surge travels over a 15m length of busduct is shown for 3CR12 in *figure 27*.

Again two values of μ_R have been considered. The results of this analysis are listed in *Table 5*, where the important criterion is the increase in the 10-90% risetime of a surge reaching 0,3pu.

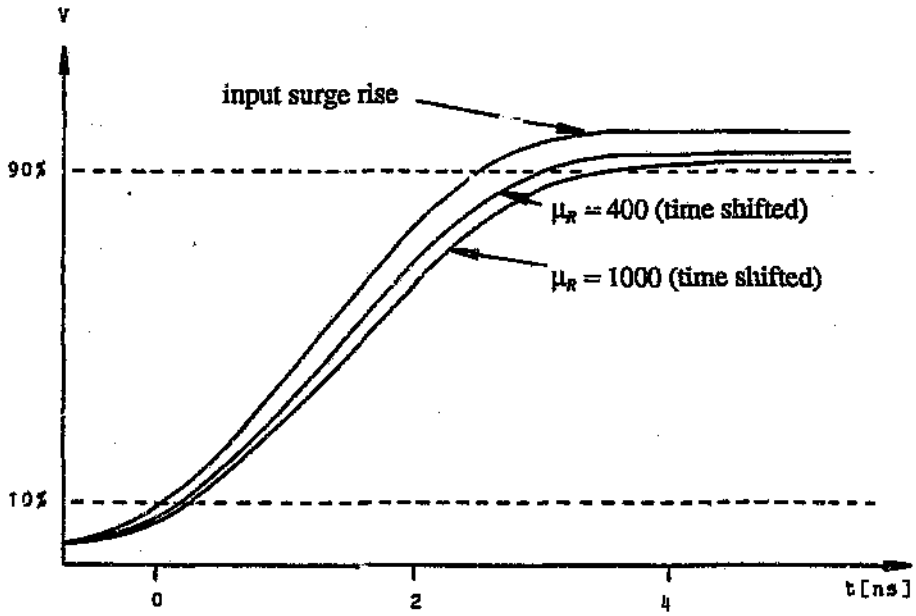


Figure 27 : Distance related increas the risetime of the surge front caused by a 50µm thick skin of 3CR12 over a duct length of 15m. Duct dimensions : $r_i = 55mm$, $r_a = 200mm$.

Table 5 : Percentage degradation of the rising edge of a surge voltage for different materials and different field intensities.

Material	Conductivity (S/m)	Relative Permeability			Coating Thickness	Percentage 10%-90% Risetime Degradation		
		μ_r	μ_R	μ_M	[μm]	μ_r	μ_R	μ_M
Commercial Iron	1×10^7	150	660	5000	129	5	7	26
Permalloy	1×10^6	1200	400	250×10^3	65	14	8	$>10^5$
Nickel	$1,4\times10^7$	110	200	-	128	3	4	-
Mild Steel	1×10^7	120	650	2000	145	3	8	14
Pure Iron	1×10^7	10000	660	200×10^3	16	49	8	$>10^5$
Supermalloy	$1,6\times10^6$	100000	240	10^6	13	$>10^5$	12	$>10^5$
Vanadium Permendur	$3,8\times10^6$	800	730	4500	91	13	13	64
Alperm	7×10^6	3000	240	55000	109	$>10^5$	19	$>10^5$
3CF12	$1,8\times10^6$	-	~400	~1000	346	-	15	28
Hypothetical Materials								
(a)	200	110	200	800	93900	$>10^5$	$>10^5$	$>10^5$
(b)	200	10000	660	200×10^3	3550	$>10^5$	$>10^5$	$>10^5$
(c)	7×10^7	120	650	2000	549	10	56	254
(d)	1×10^6	120	650	2000	4590	$>10^5$	$>10^5$	$>10^5$

5.3.2 Discussion of the Theoretical Investigation

From the preceding theoretical examination, a number of factors have been found to influence the attenuation introduced by any coating material. Some of these factors may require a detailed examination of the physics of the material, while others may merely imply the need for careful material selection.

The Effects of Magnetic Field Intensity

A non-linear relationship between B and H defines μ_r and this cannot as yet be expressed in a suitably simple mathematical form. As very high currents, and hence high fields are generated under VFT conditions, particularly after the initial surges have been reflected a number of times, it is important to select materials that saturate at high flux densities. This is adequately demonstrated in *table 4*, where the high attenuations introduced by mild steel, commercial iron and pure iron at 2600A/m are directly attributable to their high saturation flux densities of above 1,5T. All enjoy good electrical conductivities of approximately one third the value of typical electrical conductivity aluminium. A similar correlation is shown in *table 5*.

Another important feature stemming from the magnetisation curve is the fact that a high degree of hysteresis generally implies a very reduced value of μ_R at high field intensities. Furthermore, heating effects due to hysteresis losses may be detrimental at power frequency. Hence the most suitable materials to apply as coats are soft ferromagnetics, exhibiting high saturation flux densities, but not necessarily high maximum values of μ_R.

Appendix 9 shows predictions made assuming a maximum value of permeability existed at all times. Clearly these results are dramatic, but the effect of field intensity must be borne in mind.

A number of factors are known to influence the shape and extent of the magnetisation curve of any material. Not ..ly does the relative percentage composition have a marked influence, but more importantly, techniques employed during manufacture have been found to introduce large effects (Bozorth, 1951). Increased research effort should enable magnetic materials to be designed to meet specific requirements.

The Effects of Frequency

The apparent permeability of a conducting ferromagnetic material is the value of permeability that the material appears to have at high frequencies. It has been shown that, once corrections have been made for the classical skin effect within the sample, the actual permeability is found to still be at the value recorded at DC (Mallary, 1985). The mathematical model presented here accounts for changes in apparent permeability by virtue of the term $z(s)$. Furthermore, these changes are correctly predicted irrespective of coating thickness or frequency. Generally, these are the only permeability changes ever considered. However, a number of researchers have detected frequencies above which the classical theory no longer accounts for these changes, and the actual permeability of the material begins to decrease. This occurs when the classical skin depth becomes equal to the half-wall width of the material, and exchange effects dominate. For most ferromagnetics, this occurs above 100 MHz (Thornley, 1971;Thompson, 1971).

Although the attenuation of the harmonics of interest in this research may not be greatly affected by frequency effects on relative permeability, this subject is still open for investigation. *Tables 4* and *5* were generated ignoring these effects.

The Effects of the Factor $\mu_R\sigma$

A prominent and anticipated feature of the attenuations shown in *tables 4* and *5* is the poor performance of highly conductive materials at lower values of μ_R. Thus low conductivity values can be conveniently utilised providing they do not lead to unacceptably high power frequency attenuations. Alperm and the four hypothetical materials all enjoy low conductivities, but are nevertheless still conductors by definition. The good performance of vanadium permendur at $2600 A \cdot m^{-1}$ is clearly attributable to a combination effect of its high field value of permeability and its lower conductivity. Similarly 3CR12 shows a good high field performance.

The factor $\mu_R\sigma$ is thus an important criterion, and is the major factor influencing the selection of coating material. This phenomena is easily understood by examination of the simple equation defining the skin depth, δ:

$$\delta = \frac{1}{\sqrt{\pi f \mu_o (\mu_R \sigma)}} \qquad (15)$$

As the product $\mu_R\sigma$ increases, so the skin depth decreases. This introduces increased loss at the high frequencies.

The percentage attenuation of a 4 ns risetime representative pulse is shown in *figure 28*. *Appendix 10* includes numerous plots depicting the attenuation of a representative pulse, and also shows the frequency domain performance, from which the effect of coating thickness is clear.

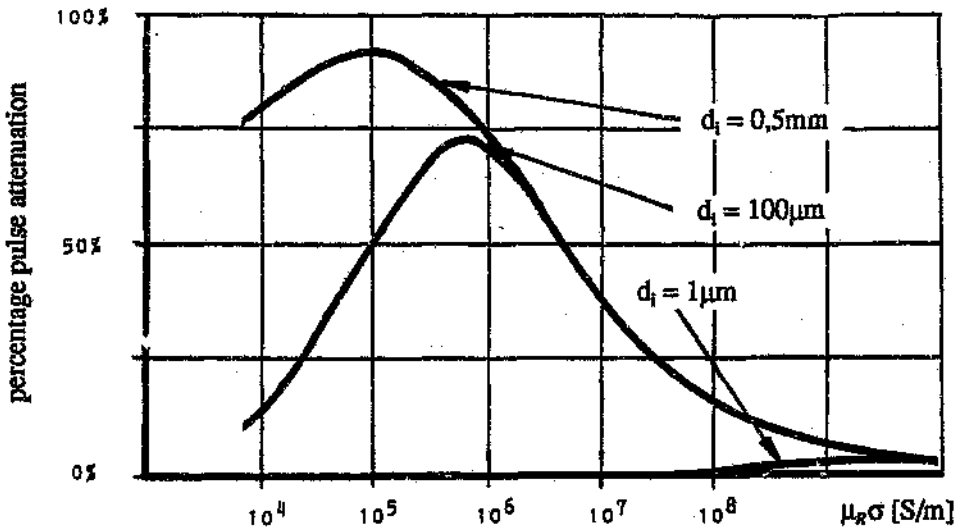


Figure 28 : Influence of the factor $\mu_R\sigma$ on the attenuation of a representative pulse - a graphical representation of peak magnitude attenuation as a function of $\mu_R\sigma$.

It must be remembered that a family of similar curves exist for differing values of μ_R, as indicated in *figure 29*. For the materials of interest, σ is a constant, and can be accurately measured. Care must be exercised in the choice of μ_R. The higher the μ_R value, the greater the attenuation spread of the curve. The plot of *figure 28* was produced using a μ_R value of 350 which, from the previous discussion, represents a realistic approximation to the value likely to be experienced under high field conditions. *Figure 30* considers the increase in the 10-90% risetime of a surge voltage with a 4 ns risetime. As expected, a close correlation exists between the curves of figures 8 and 9. Using these curves, it is therefore possible to obtain a theoretical knowledge of the characteristics of coating materials suitable for use in this application. A number of important features are shown:

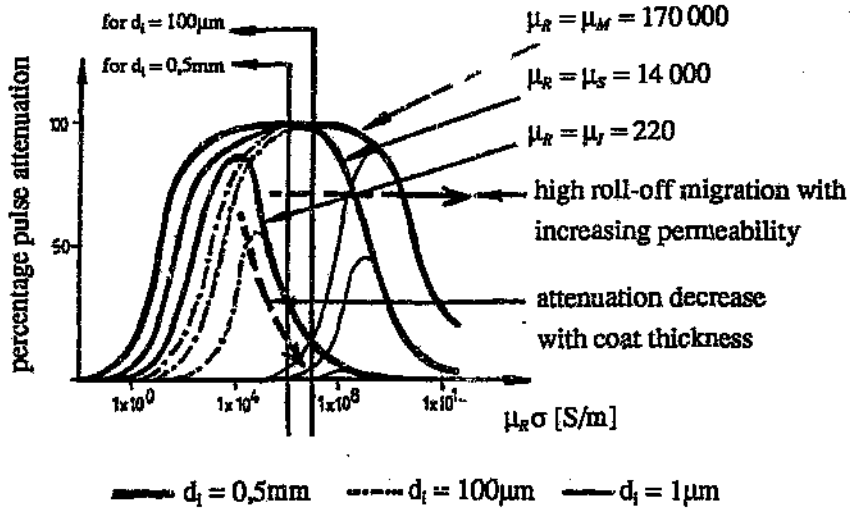


Figure 29 : Graphical representation of peak magnitude attenuation as a function of $\mu_R\sigma$ for various values of permeability.

- The reduction in attenuation at the high values of $\mu_R\sigma$ is defined in terms of the coat characteristics, and can be seen to be independent of coat thickness. However, this does imply that along this region, reduced coat thickness must introduce reduced attenuation

- The reduction in attenuation at the low values of $\mu_R\sigma$ is due to the combined effects of coat characteristics and thickness. Implicit in this roll-off is the fact that the depth of penetration for the coating material, as defined by the earlier equation, has become far larger than the coat thickness. This situation nullifies the attenuating properties of the coat, as the majority of the current flows within the aluminium busbar. (Of course, this is the same effect that allows this technique to introduce very little attenuation at 50Hz). This situation tends towards that of the application of a thin dielectric layer to the busbar. The attenuation effect in this case is therefore no longer due to changes in the internal impedance of the busbar, but is to be accounted for in the external impedance terms

- A comparison between the curves of *figures 28* and *30* shows that, for any given coating thickness, the maximum 10-90% increase in risetime occurs at higher $\mu_R\sigma$ values than the maximum pulse attenuation. Noting from equation (15) that the depth of penetration δ is an inverse function of frequency f, implying that for any given coating thickness, lower frequencies are only effectively restricted to the coating if the $\mu_R\sigma$ values are correspondingly higher. Hence the degradation of the rising edge of the voltage surge is effectively more dependent upon lower frequency effects than is the attenuation of a representative pulse. It is important that these effects be noted, and that increased

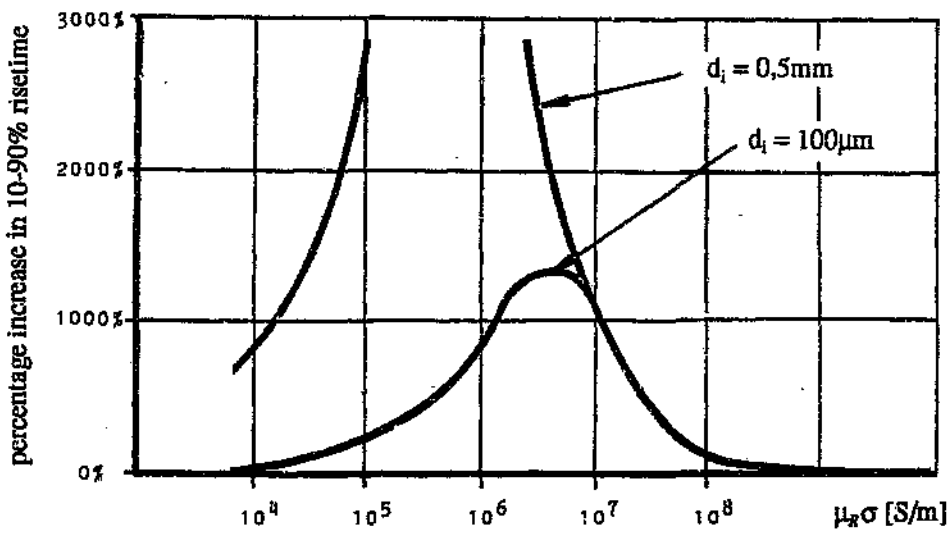


Figure 30 : Influence of the factor $\mu_R\sigma$ on the risetime degradation - a graphical representation of increase in initial risetime as a function of $\mu_R\sigma$

attenuation be introduced at as low a frequency as feasible in order to ensure risetime degradation of the initial surge voltages. For any particular coating material, this is achieved by the selection of coating thickness

5.4 Coating Performance

Using the model presented, it is thus possible to identify a range of $\mu_R\sigma$ values which would produce meaningful results over a 15m length of busduct. For a 100µm thick coating layer, and in order to introduce at least a 50% increase in the 10-90% risetime, this range extends from 2×10^4 to 4×10^8S/m. The effect of coating thickness should be noted, and it must be stressed that increased attenuation must only be introduced at frequencies well above 50Hz in order that this technique fulfil its objective of not affecting the power frequency transmission characteristics of the busduct. Furthermore, the effective range is dramatically affected by the value of μ_R for the coating (Jandrell, 1987). As both the expected field intensity and the physical effects upon the coating material during the coating process limit the values of μ_R, careful attention must be given to the conductivity of the material.

While it is clear that pulse attenuation will occur, as will risetime degradation of the initial step, it is important to remember that this analysis is only applicable to a continuous single length of busduct. Also the final "DC" value attained by the surge generated by a disconnector is not significantly affected. This is an important consideration in attempting to extrapolate too freely the results of this analysis to the case of a GIS, where numerous reflections and transmissions do occur, in order to express an opinion on the peak magnitude attenuation. What this analysis does permit us to do is draw certain valid conclusions pertaining to the VFT:

- An increase in the risetime of a surge voltage as a function of distance travelled in the duct is expected
- An increased time delay for any given distance travelled is expected in a coated system in comparison to an aluminium system

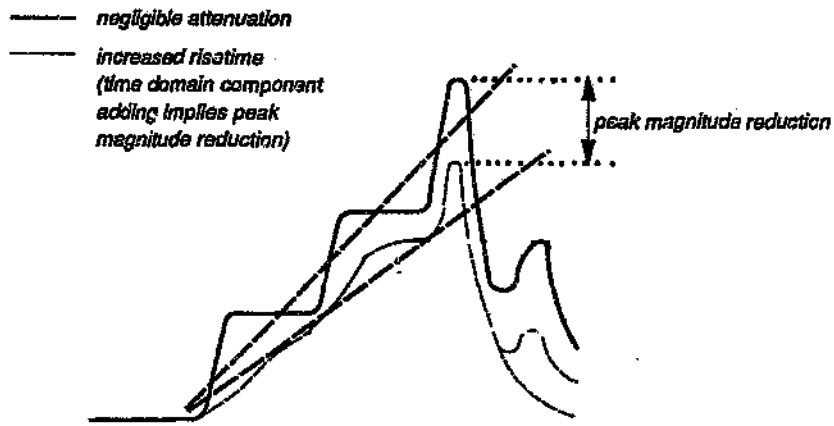


Figure 31 : Reduction in the peak magnitude of a VFT brought about by risetime increase of the initial surge with travel distance within the system. A secondary effect of the risetime attenuation is therefore a peak magnitude decrease resulting from the nature of the time domain development of the VFT.

As sugg ` in *figure 31*, this may lead to a peak magnitude attenuation, and a decrease in the *dV/dt* o. ` slope to the first and subsequent major peaks. This effect is dependent upon the configuration of the system to a large extent.

5.5 The Consideration of Four Materials for Use as Coatings

From the preceding theoretical analysis, it is possible to identify materials that may be suitable for use as coatings in this application. It is also important to give consideration to va ous coating techniques. The ease and precision with which the coating may be applied to the aluminium substrate, in this case the busbar, is of concern.

The characteristics of suitable coating materials have been found to be those of soft ferromagnetic materials, exhibiting a high saturation flux density but not necessarily a high maximum value of permeability. This is because the coating will be required to operate under saturation conditions under transient stimulation.

5.5.1 Coating Technique Considerations

Although pure iron has been shown to offer an acceptable alternative, it is evident that alloys are the materials most suited to this application. A number of factors therefore influence the choice of material, as well as the coating technique:

- The bond formed between the coating and the substrate must be mechanically sound and should preferably be conductive (Silveira, 1985)
- The coating material should not adversely affect the breakdown characteristics of the system

- The coating technique must be simple and economically viable, imposing as few constraints upon the physical dimensions of the busbars to be coated as possible

Any mechanical weaknesses may result in flaking, and thus the formation of free particles. This is undesirable. Similarly, surface roughness is an important criterion, as even small field inhomogeneities may result in very low breakdown voltages under the influence of VFTs (the very effect that this technique aims to control). Refer to *chapter 2*.

Based on these broad requirements, a number of coating techniques have been evaluated:

- Electroplating
- Hot dipping
- Metal Spraying

These techniques are briefly discussed in *appendix 17*. As noted in that appendix, a combination may provide the most viable solution, with the final coating being metal sprayed onto the prepared substrate.

5.5.2 The Four Materials

Based on the electrical and mechanical requirements of the coating, four materials have been selected for consideration. For the sake of clarity, they shall simply be referred to as samples 1 to 4. The percentage composition of each is shown in *appendix 11*, and is tabulated in *table 6*. Also shown in the appendix are the hysteresis curves and the conductivities of each sample. The techniques employed to ascertain these physical attributes are discussed in *appendix 12*. With the exception of sample 4, these materials are all suitable for metal spraying. Sample 3 has previously been very successfully metal sprayed onto various substrates.

Samples 1 and 3 are examples of soft magnetic materials. Sample 3, in particular, has characteristics very close to those considered to be most desirable for use in this application. Like sample 4, sample 3 saturates above 1,5T. Sample 2 enjoys the advantage of the lowest conductivity value, but saturates the most rapidly, at less than 0,5T.

The four B-H curves, superimposed upon each other, are shown in *figure 32*.

Table 6 : The percentage composition of the four materials.

Sample 1
C 0,070; *Ni* 59,35; *Mn* 0,71; *Si* 0,15; *Cu* 0,06; *S* 0,005, *P* 0,007; *Fe* Balance
Sample 2
C 0,102; *Cr* 29,95; *Ni* 9,73; *Mn* 1,95; *Si* 0,40; *P* 0,02[illegible] *S* 0,0011; *Mo* 0,09; *Fe* Balance
Sample 3
C 0,03; *N* 0,03; *Ni* 1,5; *Mn* 1,5; *Si* 1,5; *P* 0,03; *S* 0,03; *Cr* (11,0-12,0) *Ti* 4·(C+N); *Fe* Balance
Sample 4
Cr 5; *Co* 40; *Fe* 55

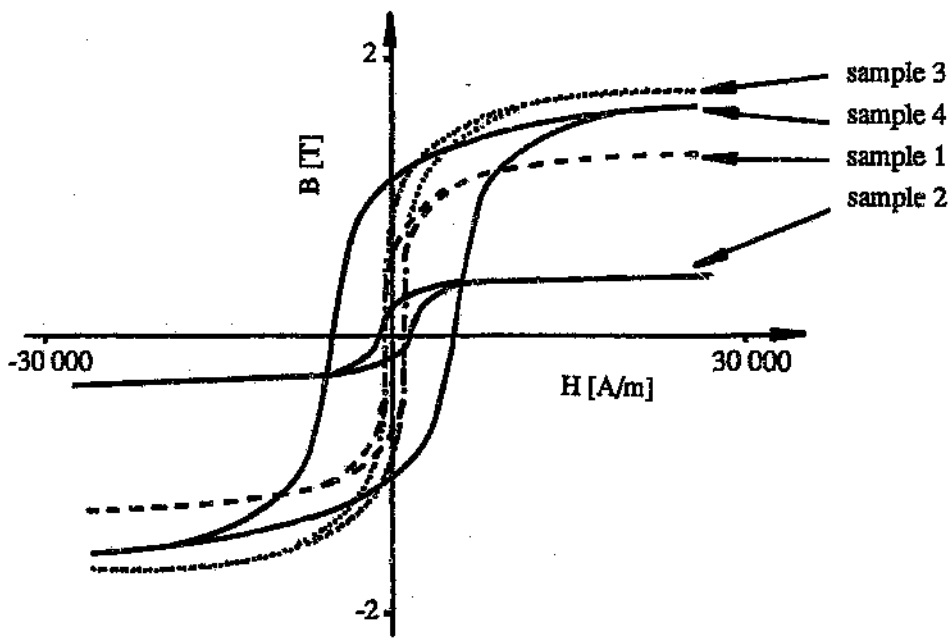


Figure 32 : Superimposed B-H curves of four materials considered for use in this application.

In order to examine the effect of this coating technique upon the rising edge of the transient, the degradation introduced to a surge with a 4ns risetime over a 15m length of busduct has been considered. For the simulations, the surge front has been considered to pass the measuring point, travel 7,5m to an open circuit, and then return to the observation point.

In order to assess the value of permeability likely to be experienced for each coating material, it is important to decide the expected magnitude of the voltage surge. The peak magnitude of the initial surge was chosen to be 0,7pu. This implies a trapped charge of 0,4pu, and a source side line-to-ground voltage of 1,0pu on switching. This is essentially the highest value of initial surge likely to be experienced in modern equipment (Boeck, 1987). All the predictions were for a typical 132kV system operating in a busduct with a busbar radius of $r_i = 55\text{mm}$, and a grounded enclosure with an inner radius of $r_g = 200\text{mm}$.

The predictions were conducted at field intensities of 2080A/m, which is calculated in *appendix 13* as being representative of the field intensities likely to be experienced under the influence of a VFT. The predictions were repeated at a field intensity of four times this value in order to show the effect of reduced permeability. The permeability values were determined from the virgin magnetisation curves of each sample of material, thus making the tacit assumption that the ferromagnetic coatings were demagnetised immediately prior to the transient event. The results of these simulations are shown in *appendix 14*. In that appendix, the attenuation characteristic, the representative pulse response, and the surge response are shown for the four samples.

From the attenuation characteristic, it is clear that the reduced values of permeability at the higher field intensity manifests itself as a reduction in the attenuation at the higher frequencies.

It should also be noted that a close relationship exists between the percentage attenuation introduced to a representative pulse and the degradation of the rising edge of the surge.

The performance of the various materials, measured as the percentage pulse attenuation, is summarised in *Table 7*.

Table 7 : The pulse attenuation introduced by the four sample materials. Note that the attenuation at low and high field intensities are show. (Permeability is affected by the field intensity.) The increase in the 10-90% risetime was only determined at the realistic value of field intensity for the most promising samples.

Sample	Field Intensity [A/m]	Pulse Attenuation [%]	Risetime Increase [%]
1	2080 8320	4,90 2,93	15 not determined
2	2080 8320	3,00 2,34	not determined not determined
3	2080 8320	6,75 4,13	25 not determined
4	2080 8320	1,79 3,19	not determined not determined

With reference to the table, samples 1 and 3 show the most favourable results at both field intensity values. At 2080A/m, sample 1 introduces 4,9% attenuation to the pulse, and increases the 10-90% risetime by approximately 15%. For sample 3, these values are 6,75% and approximately 25% respectively. The high saturation flux density of sample 3 ensures that it still introduces a marked degradation of the rising edge at a field intensity of 2080A/m. In sample 1, this effect has been greatly reduced.

Samples 2 and 4 are, from these results, shown to be least suitable. Sample 2 saturates too soon, while sample 4 cannot be classed as a soft ferromagnetic material.

5.6 Concluding Observations

A method of reducing both the magnitude and dV/dt of surges and pulses by the application of ferromagnetic coatings has been discussed in this chapter. A number of conclusions may be drawn from the theoretical analysis and the results presented in the previous section:

- The application of coatings to the inner busbar only need be considered
- The magnetic properties of suitable coatings are those of soft ferromagnetic (ie materials exhibiting low hysteresis losses, characterised by a narrow B-H curve) materials exhibiting high saturation flux densities, yet not necessarily high values of maximum permeabilities. Careful consideration must be given to ensure that sufficient VFT attenuation is introduced without introducing unwanted 50Hz attenuation
- Above about 100MHz, the actual permeability of most materials is known to decrease
- The maximum attenuation is a function of coating thickness
- The factor $\mu_R\sigma$ has been identified as a major design criterion for coating materials. The attenuation reaches a maximum for a range of $\mu_R\sigma$ values, dependent largely upon the permeability of the material at the highest expected field intensity
- It has been shown that the degradation of the rising edge of a voltage surge is more dependent upon lower frequency effects than is the attenuation of a representative pulse. This is because of the broad band frequency content of the pulse. Consequently, increased attenuation must be introduced at as low a frequency as feasible in order to effectively degrade the rising edge of the initial surge
- Changes in the physical characteristics of the coating material during the coating process must be given careful consideration

Any suitable coating material must provide not only good permeability values, but also suitable values of conductivity. The form of the magnetisation curve is also an important criterion, as demonstrated by the ineffectiveness of the hard magnetic material, sample 4. It must be noted that the most useful of the four samples considered in this chapter, sample 3, is a stainless steel alloy, 3CR12. Its magnetic characteristics were previously unknown. It is thus clear from this discussion that a combination of these attributes in a single material will ultimately ensure the success of this technique.

It is important that any coatings be used in such a manner as to only introduce effective attenuation to the high frequency voltages and currents. Fabricating the entire busbar from the coating material would lead to unacceptably high power frequency attenuation.

It should be stressed that the effectiveness of this technique is largely dependent upon the available transmission distance for the initial surge within the busduct. Also, because the effect of field intensity is so marked, it is important to introduce as much attenuation to the initial surge as possible before any subsequent reflections have lead to increased values of field intensities in the GIS case. This will be discussed in greater detail in *chapter 6*.

Chapter 6 : A Travelling Wave Model for VFTs and Laboratory Results

6.1 Introduction

In this chapter the emphasis will be on two aspects of this work:

- A travelling wave model for a simple GIS
- Laboratory results obtained from a ferromagnetic system operating at high voltage

The theoretical work presented in *chapter 5* has shown that the application of ferromagnetic coatings to the surfaces of the busbars in a gas insulated busduct may lead to a noticeable diminuation of the undesirable features of the very fast transients associated with the operation of a disconnector switch (Jandrell, 1988).In order to examine the actual effects in realistic systems, it was necessary to utilise the available laboratory equipment, where long travel distances did not exist. The longest system available for experimental work is shown in *figure 33*.

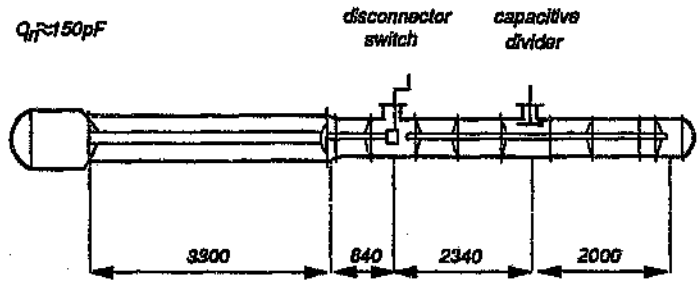


Figure 33 : Longest system supported at the Werner von Siemens test facility at the University of the Witwatersrand, and the syste... in which the high voltage experiments were conducted.

Accurate travelling wave models allow for good correlation between predicted and recorded responses for long time periods (Witzmann, 1987). Little effort, however, has been directed towards the accurate modelling of short time periods where effects introduced by differing conductor materials are specifically accounted for. This is not surprising, as little attenuation is expected to be introduced by the simple skin effect in aluminium ducts (Jandrell, 1988; Witzmann, 1987) (Refer also to *figures 24* and *25*). The predominant portion of the transient attenuation is ascribed to spark resistance, while the skin effect is ignored, or only crudely accounted for (Alvinson et al, 1988).

By contrast, in the travelling wave model discussed in this chapter, the nature of the investigation dictates that interest be specifically in the effects of the busbars and grounded enclosure upon the attenuation of the transients. Other system components are accounted for by the use of simple accepted methods. Furthermore, if the application of coatings is to be considered as a means of controlling VFTs, it is apparent that an effect must be noticeable within the first few reflections of the initial step voltages. The software model presented here is thus not envisaged to be a replacement for existing transient analysis techniques. It serves to facilitate the study of a specific effect. The importance of this model was to enable us to gauge the effectiveness of this technique in a system incorporating reflections and transmissions (Jandrell, 1989; Jandrell 1990).

The frequency domain model presented in *chapter 4* has been extended in order to simulate a number of coupled sections of GIS. The entire vessel has been defined in terms of the discontinuities within it, while each section is still individually defined. Although this technique is well known, this is the first time a detailed skin effect model has been included in it. It also has a number of drawbacks:

- The number of alternate paths that may be defined to exist between the disconnector and the observation point is limited by available computer memory
- The time taken to simulate the system response is excessive on an IBM AT operating at 12MHz
- A relatively large amount of data is requi d in order to define the system in sufficient detail to fully utilise the power of the models used

The last mentioned drawback is merely a function of the detail of the model presented in this work. Furthermore, it is important to note that the only required data is of a physical nature. All electrical characteristics, including electrical lengths of sections of the GIS, are determined by the program as functions of frequency. Furthermore, the alternate paths that may exist are determined by the program as it operates.

The two remaining drawbacks, first and second in the list above, are limitations imposed by the hardware being used and are merely irritations. For this work, however, the complexity of the systems was reduced and the time interval of interest minimised in order to only show the effects we were interested in.

6.2 The Model

From the work on which this transient analysis model is based (Jandrell, 1987), it is clear that the effects of both the busbar and the outer grounded enclosure are directly accounted for. Previous work allowed for the time domain study of a single section of duct (Jandrell, 1988). The propagation effects associated with discontinuities within a duct were not accounted for. This is evident from the analysis contained in *chapter 5*. As shown in *figure 34*, the two characteristic impedances need not necessarily be equal. Furthermore, they and hence the reflection and transmission coefficients, are non-linear functions of frequency, being dependent upon the conductor and coating materials used. Many of the assumptions made in the development of the transient analysis model are thus derived from the original mathematical model.

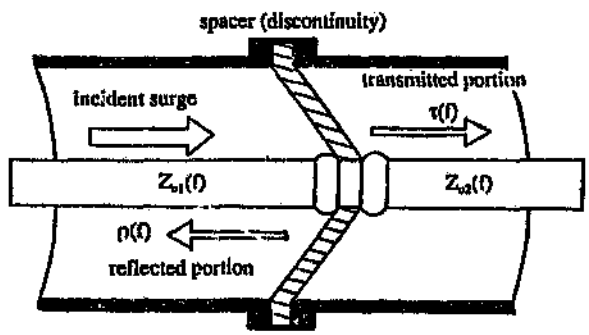


Figure 34 : A generalised discontinuity in a GIS, showing the frequency-dependent characteristic impedances on either side of the discontinuity.

6.2.1 Assumptions

In the development of any model of a physical process, it is important to make simplifying assumptions that will not detract from the accurate operation of the model. The following assumptions have been made:

Linear System Elements

This assumption allows the use of superposition to establish the final form of the VFT at any point within the duct. It is, for example, in accordance with the use of single capacitor values to simulate the effects of voltage transformers and spacers. The transient spark resistance, which changes very rapidly during the voltage collapse at the disconnector contacts, is accounted for in the definition of the risetime of the time domain waveform used to represent the initial negative and positive voltage steps generated at the disconnector. However, this assumption disallows the use of a changing value of relative permeability, μ_R, in the physical definition of a ferromagnetic material. The complications associated with selecting a suitable value of μ_R for the simulation are addressed in *chapter 4*, and are also discussed elsewhere (Jandrell, 1988).

Instantaneous Establishment of the Flux Within the Busbars

This assumption makes it possible to utilise the Fourier technique in order to determine the time domain form of the VFT based on the frequency domain model of the busduct. The attenuation experienced by a given frequency component is thus assumed to remain unchanged in time, allowing the establishment of a frequency transfer function. While the frequency domain model accurately accounts for the skin effect in coated conductors of the form and dimensions typical of a gas insulated duct, the transient component of the skin effect is ignored. Were this assumption not made, the concept of a characteristic transmission function would be meaningless (Jandrell, 1990).

Only a Single Phase of a Three Phase System Need be Modelled

Particularly at higher operating voltages, single phase busbars are separately encapsulated. No attempt has been made to model the three phases of a system encapsulated within a single grounded enclosure.

These three assumptions form the basis of the model presented here, and facilitate easy understanding of its operation.

6.2.2 Incorporation of Reflection and Transmission Coefficients

Consider first a single incident wave in a simple system. In *figure 35*, the incident wave represents a a surge voltage emanating from a disconnector switch. The observation point would be realised by a broad bandwidth capacitive voltage divider.

As the surge propagates within the duct, it passes the observation point, and is recorded for the first time, and is labelled voltage step 1 in the figure. (This is considered to constitute a single "path" between the source and observation point for this system.) The surge continues to propagate, and would then be reflected at the open circuit, whereupon it passes the observation point travelling in the opposite direction (in this case) and is recorded for the second time. (Again, the travel from the source to the observation point is considered a "path" in this model.)

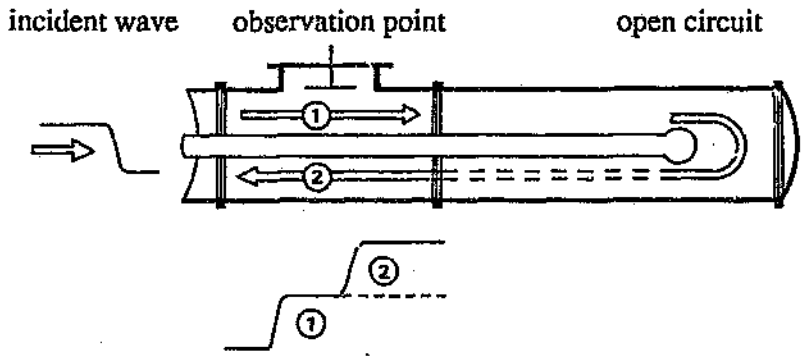


Figure 35 : Figure depicting the addition of the time domain components in order to build up the VFT recorded at a particular point in a GIS.

At the measuring point, the two recordings are superposed to give the waveform indicated, representing the VFT over this short time interval.

Now consider a more extensive system, in which both initial surges generated by the disconnector must be accounted for. Note that the non-linear spark resistance is tacitly included in the definition of the rising edge of the surges.

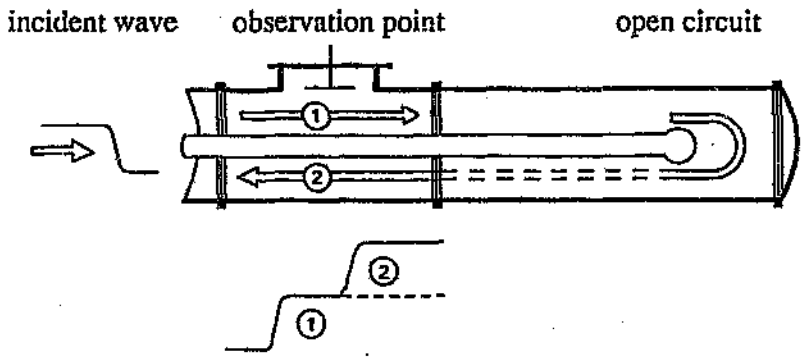


Figure 35 : Figure depicting the addition of the time domain components in order to build up the VFT recorded at a particular point in a GIS.

At the measuring point, the two recordings are superposed to give the waveform indicated, representing the VFT over this short time interval.

Now consider a more extensive system, in which both initial surges generated by the disconnector must be accounted for. Note that the non-linear spark resistance is tacitly included in the definition of the rising edge of the surges.

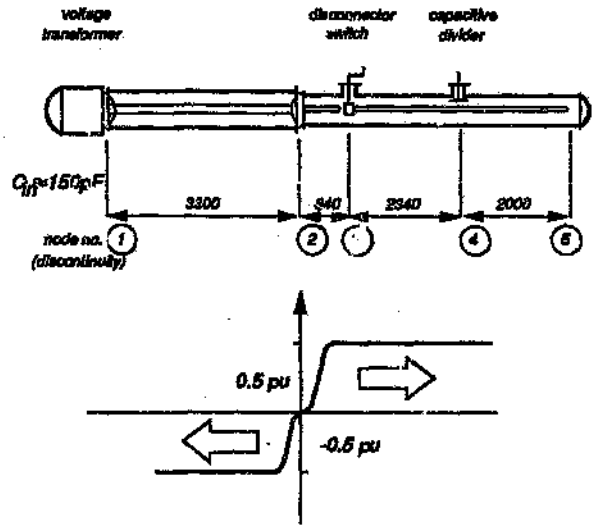


Figure 36 : A simple system, with the two surges generated at the disconnector shown. The Fourier technique is used to move between the frequency and time domains and back again. The time domain definition of the initial surges is shown in *appendix 7*. In particular, refer to *figure 7.2*.

Consider the simple system shown in *figure 36*. The initial surges are as indicated in the diagram. The discontinuities (nodes) are numbered. In any given observation interval there exist a finite number of alternate paths between the disconnector and the measuring point, each path being identified by an ordered number series representing the nodes visited. Once the system has been defined as a linked list of nodes, and the approximate propagation time between each node is known, it is a simple matter to construct a table of paths, as shown in *table 8*, by searching through the list.

Table 8 : Determined valid paths for a particular time period in the system depicted in *figure 36*.

Path Number	List of Nodes Visited	Path Number	List of Nodes Visited
1	3212121234	17	3454323454
2	32121234	18	345432345432354
3	3212123454		
4	321234		
5	32123454		
6	3212345432354		
7	3234		
8	323454		
9	3234543321234		
10	3234543234		
11	323454323454		
12	34		
13	3454		
14	3454321234		
15	345432123454		
16	34543234		

Consider for example *path 7* shown in *table 8*. (Bear in mind that all the listed paths are valid - ie they contribute to the final form of the VFT for a specified time period.) The information tells us that the surge first leaves the disconnector (initial *node, 3*). This negative surge (refer to *figure 36*) travels to *node 2*, encounters a discontinuity, and is reflected back to the observation point (*node 4*), passing through *node 3*. Hence the nodes visited may be listed as:

3, 2, 3, 4

Since the above surge was in fact reflected at *node 2*, a portion would also have been transmitted through that node. (See, for example, *path 4*.)

In the most general case, each such path is unique, in that it presents a different transfer characteristic to the initial step voltage. Each such transfer characteristic has associated with it a particular magnitude and phase component. These components are established from the transfer characteristics of all the duct sections falling on the path between the source (disconnector) and the observation point (capacitive divider). Furthermore, these transfer characteristics are not linear functions of frequency - the skin effect, particularly in the case where coatings are applied to the busbars, introduce a marked non-linearity. As suggested in *figure 37*, the time domain response associated with each path is individually determined, and these then superposed to give the final from of the VFT.

A dynamic data structure is used to establish the list of alternate paths. This allows the amount of computer memory used to expand or contract to suit the system being examined. It also implies that there may be a number of alternative paths connected to any node in the network. The number of alternative paths is thus a function of the system complexity, the time interval of interest, and the length of the shortest section of duct. Thus the available computing power places limits on the complexity of the systems that may be reasonably simulated. However, since interest is primarily in effects that should be immediately evident in the recorded VFT, this is not a severe limitation, and simulations are conducted on a personal computer. *Figure 38* explains the operation of the transient analysis model. Refer to *appendix 15* for the theoretical determination of ρ and τ, and *appendix 16* for a brief description of the software used in this part of the simulation.

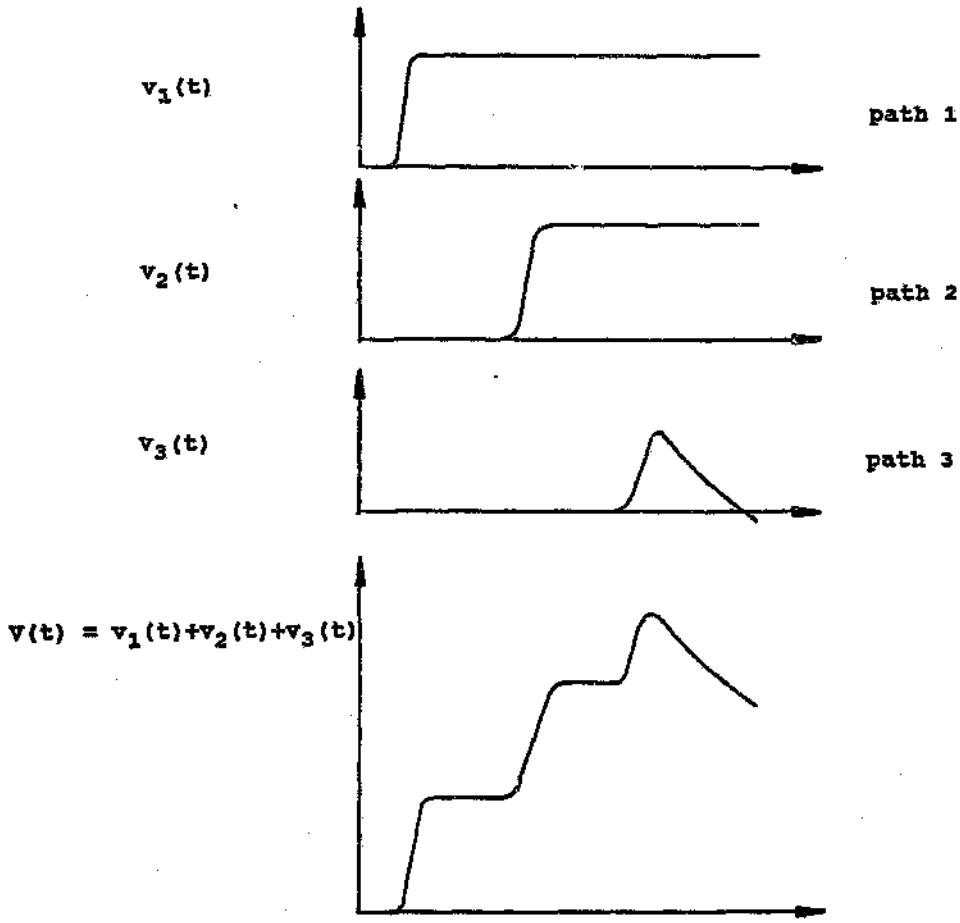


Figure 37 : Addition of the time domain components leads to the final form of the VFT.

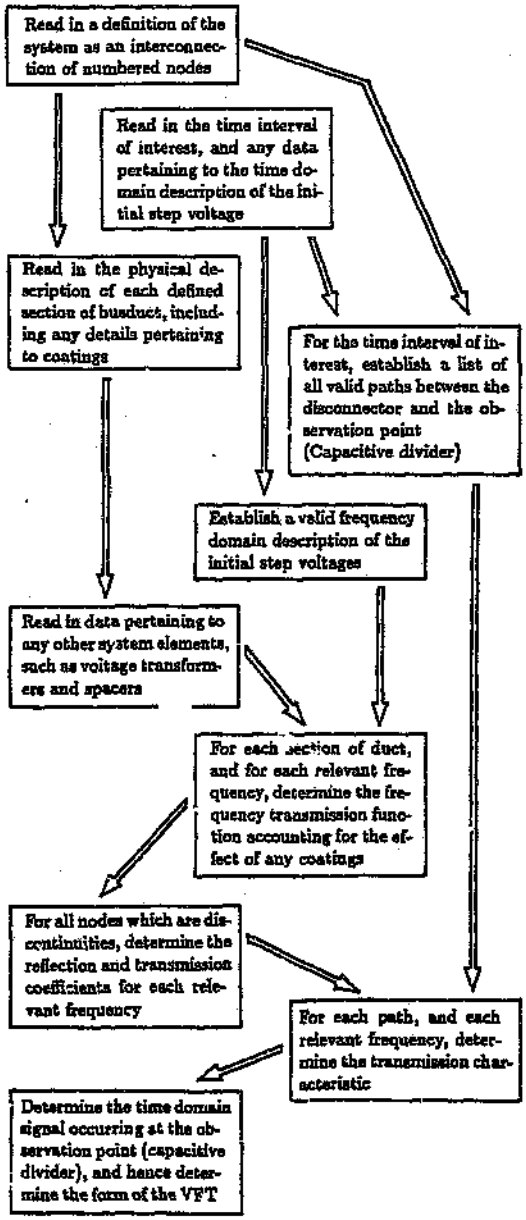


Figure 38 : Description of the operation of the transient analysis model.

6.2.3 Verification of the Transient Analysis Model

The validity of the model for a single section of duct has been established in *chapter 4* and elsewhere (Jandrell, 1987). The performance of the transient analysis model is tested against results obtained from a Bewley-Lattice-type model, similar in operation to TLTA (Fujimoto, 1985).

In order to verify the model, consider the system depicted in *figure 36*, and an observation interval of 150ns. For valid results, all that we need ensure is that the initial step voltages are of duration longer than this interval, and that Nyquist's criterion is observed when determining their Fourier components. The magnitude and phase associated with the characteristic impedance of each section of duct is automatically determined during execution of the model. Furthermore, the speed of travel of the transient voltage is a function of the busbar characteristics, and this delaying effect is also automatically determined.

This model allows us to isolate the time domain component of the final VFT emanating from any particular path. This is shown in *figure 39*. The figure also shows the final VFT occurring at the measuring point, and compares it to the Bewley-Lattice result. As expected, the transient analysis model performs accurately. The slight time shifts between the two results are, in fact, due to limitations imposed by the choice of the time step used for the Bewley-Lattice simulation. As the physical characteristics of aluminium conductors have been used in this simulation, there is little difference in the attenuation introduced between the two results. For the sake of comparison, the VFT formed in a system with a coating with physical characteristics $\sigma = 1,8 \times 10^6 S/m$, $\mu_R = 350$ is also shown.

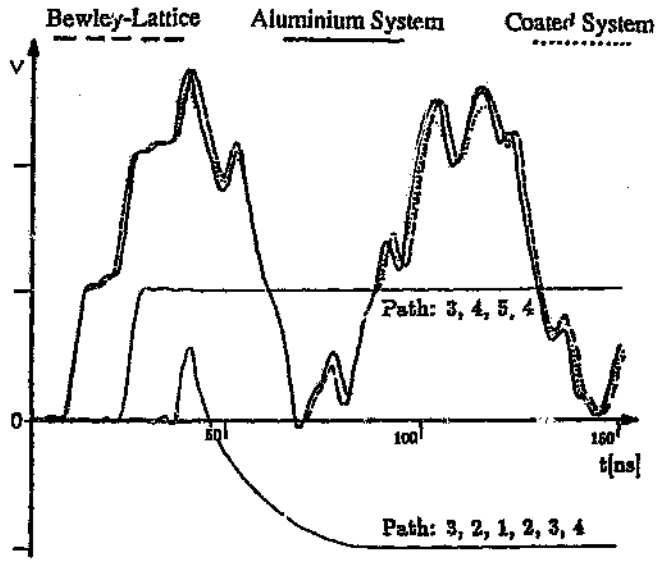


Figure 39 : Predicted form of the VFT for a simple busduct. Also shown are two of the time domain components making up the final form of the VFT recorded at the particular point in the duct.

It is therefore apparent that the program accurately models the transient response of an easily defined system, where the system response is predominantly that of the busbars. However, when more GIS elements are added, they need to be accounted for in order to retain the desired accuracy. Since the objective of the model presented here has been to account for the busbars and grounded enclosure, other system components are modelled as carefully dimensioned lumped elements.

6.2.4 A Theoretical Consideration

From the examination of pulse and surge responses of single continuous lengths of duct, it is expected that both peak magnitude attenuation and risetime increase will be introduced by this technique. Due to the nature of VFT formation at a particular location within a duct (eg the observation point), however, it is important to view these effects on a simulated VFT, where the scale of the improvement is more evident. The effects likely to be introduced are shown in *figure 40*, where multiple reflections in a short system depicted in *figure 36* are accounted for.

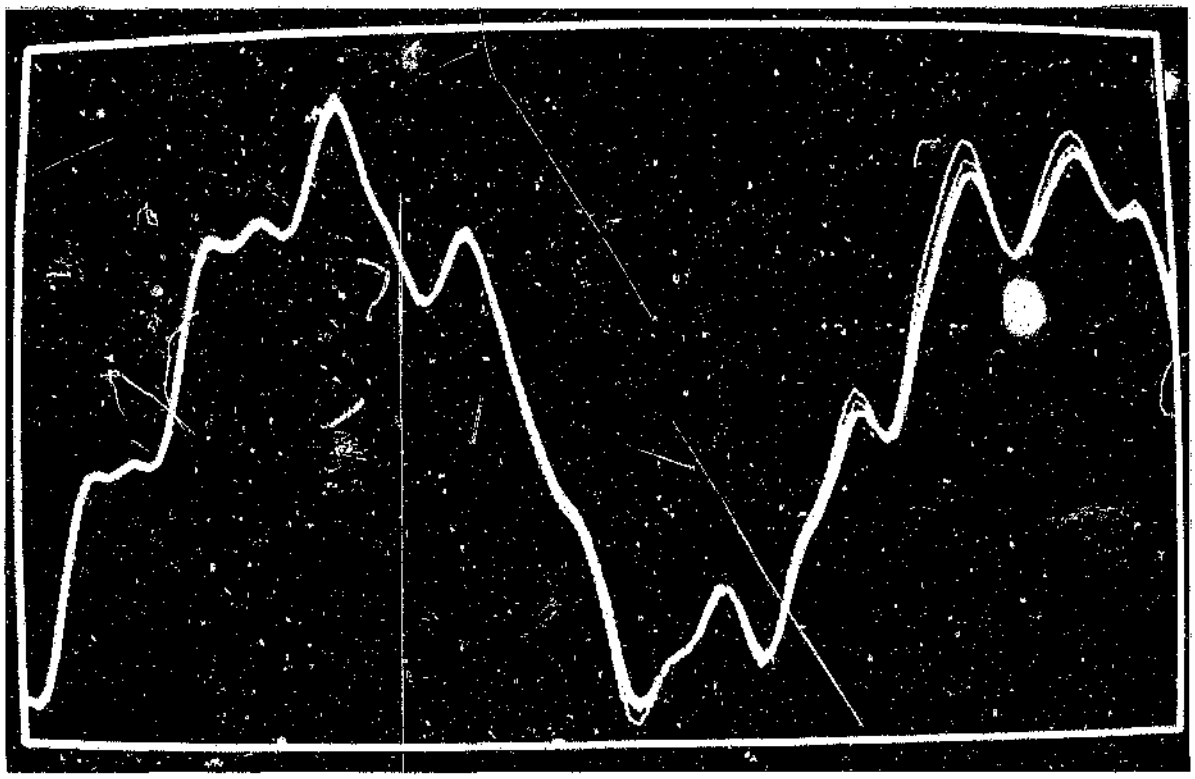


Figure 40 : Computer simulation of the effects likely to be introduced in the system depicted in *figure 36*. The three systems depicted are as follows : The one showing least attenuation is an all aluminium system, with $\sigma = 3,5 \times 10^7 [S/m]$. The system showing an intermediate amount of attenuation has coated busbars, where the coating has the characteristics $\sigma = 1,8 \times 10^6 [S/m]$ and $\mu_R = 350$. The system showing the most significant attenuation is similar to the previous one, but in this case the coating relative permeability has a value of $\mu_R = 1000$. As noted earlier, this shows the importance of the field intensity-related value of relative permeability.

Three important effects are evident:

- Risetime increase is evident on the leading edge of the second major peak. The greater the relative permeability, the greater the degradation. It must also be remembered that this effect is a function of transmission distance
- Peak magnitude, or envelope attenuation, is also evident on the second major peak. While this effect will be affected by transmission distance, it is also largely dependent upon system configuration

- As the propagation velocity is dependent upon the impedance of the system, the corresponding peaks of each of the three traces are slightly displaced relative to one another. This effect is also enhanced by transmission distance

It should therefore be stressed that this travelling wave model serves primarily to allow results like those above to be obtained in order to allow examination of the effects introduced by materials with various coatings applied.

6.3 The Effect of Ferromagnetic Busbars

In order to experimentally examine the effect of a ferromagnetic coating upon the attenuating characteristic of a section of duct, the system depicted in *figure 33* was used. While a technique of applying a ferromagnetic coating to an aluminium substrate was established, it proved impracticable to implement in the laboratory system shown. Instead, two similar systems were used. In one, the busbar was fabricated from aluminium. In the other, the busbar was fabricated from mild steel. Although the outer grounded enclosure was of the same material in both systems in accordance with the discussion in *chapter 4* this is of no consequence.

The tests were conducted at voltages which ensured that the peak magnitude reached by the transients was in excess of 200kV. This ensures an initial step voltage of magnitude similar to that used in previous predictions (Jandrell, 1988). (Refer also to *chapter 5*.) The high fields experienced under these conditions were expected to reduce the value of permeability, thus making the enhanced attenuation effect difficult to detect in the laboratory system used. *Figure 41* shows a superposition of the records made in the two systems. The mild steel system introduces a significant and increasing time delay. It must be noted that this time delay is associated with the phase angle associated with the various frequency components, and hence rise time increase.

When observed over a longer time interval, as shown in *figure 42*, an envelope attenuation is also discernible. While in this record the first peak of the mild steel system is greater in magnitude than that of the aluminium system, the subsequent peaks and troughs converge, showing that the envelope attenuation of the mild steel system is observably greater than that of the aluminium system.

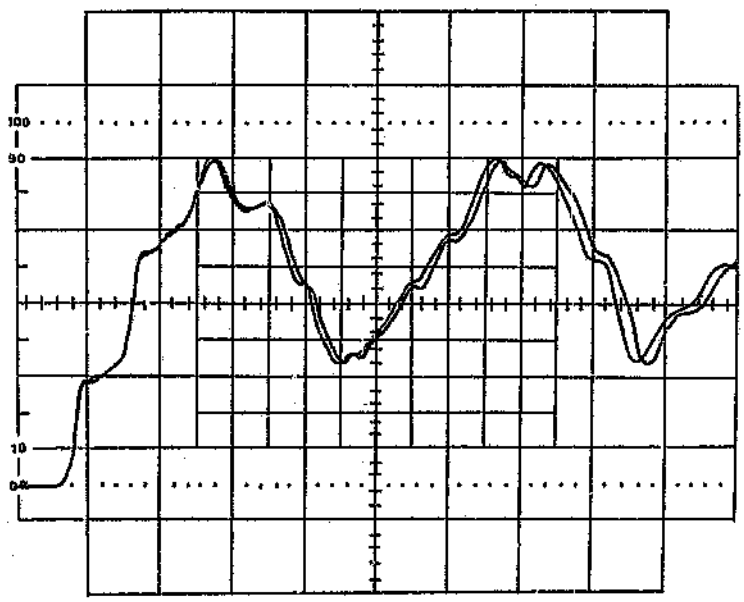


Figure 41 : Superposition of two VFTs. One was recorded in a standard aluminium system, while the other was recorded in a laboratory system similar in all aspects except that ferromagnetic busbars had been installed. Scales: 20ns per large division; 45,4kV per large division.

The results shown in *figure 43* indicate a clear increase in the risetime of the initial step in the mild steel system. The results of a simulation are also shown in *figure 43*. When using values of μ_R determined as described elsewhere (Jandrell, 1988), less risetime degradation than that shown in the recorded results is predicted. The records show an increase in the risetime in excess of 10% in the mild steel system. The simulation predicts only ~3% increase using a value of $\mu_R = 650$. The conductivities of the materials used in both systems have been measured, and may be considered constant.

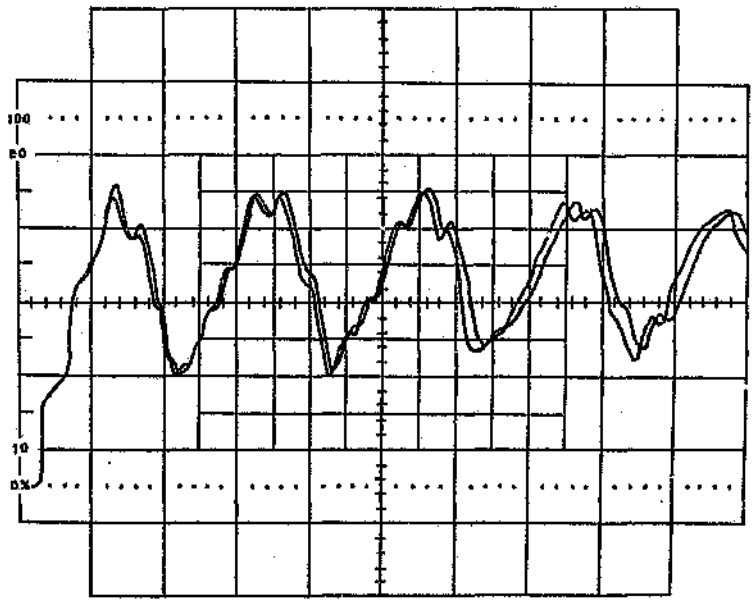


Figure 42 : Superposition of two VFTs shown over an increased time interval. Note the ever-increasing shift between corresponding features of the two traces, in accordance with the predicted decreased travel velocity in the more lossy system. Scales: 40ns per large division; 45,4kV per large division.

The enhanced degradation may only be justifiable accounted for by using a higher value of μ_R in the simulation. This has the effect of constricting the transient to an even thinner layer near the surface of the conductor, thus enhancing the attenuation. This is, in fact, exactly what happens. The deeper layers of the ferromagnetic have not yet saturated, and hence present a high permeability value to the flux as it penetrates and ultimately saturates the steel. This effect will now be briefly discussed. In order to place the discussion in the correct perspective, bear in mind that the fact that the model presented in *chapter 4* is defined in the frequency domain implies that it is really a steady state approach. It will be shown that the transient component of the skin effect can account for the increased attenuation recorded in the laboratory. (The merits of various techniques, including the Fourier technique, are discussed by Bickford (1967).)

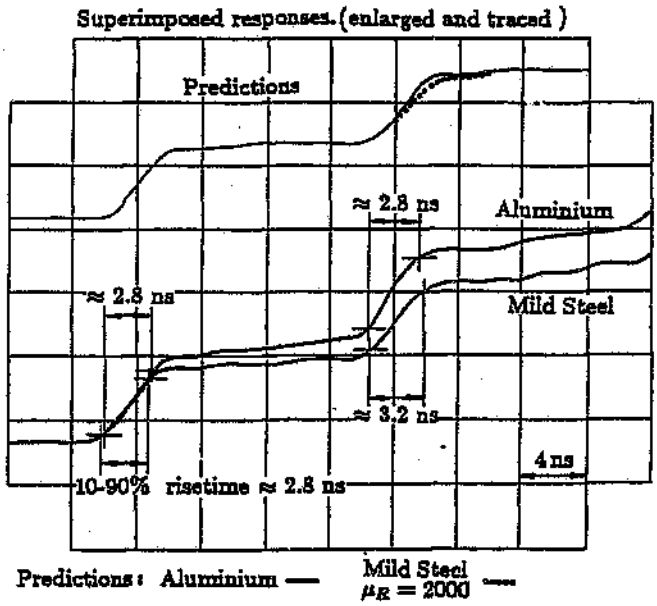


Figure 43 : The effect of a ferromagnetic busbar on the risetime of a VFT. While a distinct effect is evident, it is exceedingly difficult to quantify.

6.4 Consideration of the Transient Skin Effect in Coaxial Conductors

With particular regard to the increased risetime degradation recorded in the mild steel system, it is of important to consider the actual time taken for establishment of the flux within various conductors.

For example, it is important to distinguish between the so-called AC resistance (R_{AC}) and the transient resistance (R_{TR}) of the conductors. Both have been the subject of numerous investigations (Malewski, 1972; Miller, 1947; Nahman, 1962; Yen, 1982), and are defined in terms of the field penetration into the conductors. Importantly, determination of R_{AC} implies a steady state phenomena - frequency dependent, but not time dependent. R_{TR} is associated with a time dependent effect that would ultimately result in $R_{TR}=R_{AC}$ if the stimulation were to continue for sufficiently long. In the choice of the most suitable model to use for a particular application, care must be taken to assess the relevance of the model against the accuracy that can be expected.

In the determination of R_{TR}, a very important parameter is the time that it takes the fields to penetrate the conductor, as the value of R_{TR} represents the resistance seen by the current caused to flow in the conductor by the diffusion of the flux into them. This implies the association of a time constant with the development of the fields within the conductors. A simple model clearly showing this effect has been proposed by Yen (1982). For a continuous length of co-axial line where the inner and outer conductors are fabricated from the same homogeneous material, the line is divided into N longitudinal sections. Each of the N sections consists of M partial resistors and M-1 partial inductors derived directly from the skin effect differential equations. This concentric ring definition of a co-axial line, as well as the skin effect equivalent circuit, is shown in *figure 44*.

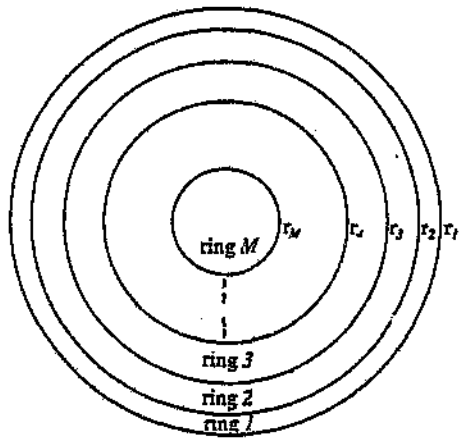


Figure 44(a) : Concentric ring definition of the centre conductor of a coaxial system.

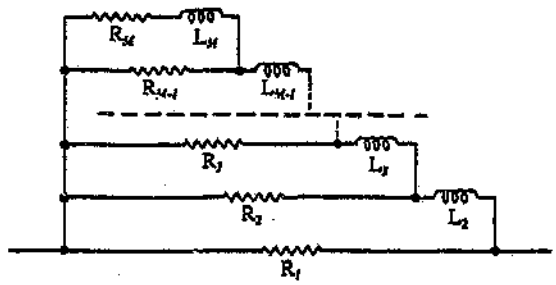


Figure 44(b) : The skin effect equivalent circuit (Yen, 1982).

A number of important observations pertaining to this model can be made:

- The effective resistance of the line is a function of time, where the partial resistances and partial inductances dictate the time constants associated with the transient current distribution within the conductor
- The current distribution at DC is uniform, as expected, and the DC resistance, R_o, is given by the parallel combination of the partial resistors
- The high frequency resistance is limited to the resistance of the outermost ring
- Under transient conditions, the current distribution is valid for an instant in time, and the series resistance, R_{TR}, is thus also valid only for that instant
- The partial resistances and inductances must be related to constant physical parameters of the material - the conductivity (σ) and permeability (μ) respectively

It is noted by Silvester (1966) that this technique is severely limited at the higher frequencies as the impedance at the highest frequency is fixed at the limiting value of partial resistance, defined in terms of the thinness of the outermost layer. The thinnest layer thickness also dictates the shortest time constant associated with the system.

For the systems of interest, it is thus important to quantify the time taken for establishment of the steady state condition under stimulation by a step wave with a very fast risetime. In this consideration, the skin depth, δ, is an important parameter as it dictates the thickness of the layers required in order to usefully model the transient component of the skin effect. Clearly, in order to introduce the time dependent effect, at least five layers should be used to define the steady state skin depth, δ The velocity at which the current penetrates the conductors is important.

Miller (1947) has shown from the skin effect differential equations for a cylindrical conductor, that for any (conductive) material a coefficient of current penetration (or diffusion), h, may be determined. Thus the velocity of current penetration, v_D, may be defined:

$$v_D = \frac{h}{\sqrt{t}}$$

where : v_D = current penetration velocity [m/s]. (Recall that the current propagates along the conductor in the direction of current flow. v_D defines the velocity of current penetration (diffusion) from the conductor surface into the conductor in a direction normal to the axial direction of current flow.)

h = coefficient of current penetration [m/$\sqrt{s}$].

t = time [s].

Two important observations may be made:

- v_D is not a constant, but decreases with time inversely as the square root of time
- At any time the approximate depth to which current has penetrated (diffused), δ', may be defined as:

ie $\delta' = 2h\sqrt{t}$

Using values of h determined by Miller (1947), v_D is shown in *figure 45* as a function of time for three materials - copper, aluminium and steel. In the case of the steel, the relative permeability (μ_R) has been assumed to be a constant of 1000.

The velocity of penetration is significantly more rapid in the copper and aluminium than in the steel. Furthermore, v_D is approximately 1,25 times more rapid in aluminium than in copper. Based on this information, it is important to quantify the time taken to reach the steady state skin depth in the materials. Due to the nature of the formation of a VFT, it is not the oscillation frequency that is of concern - rather it is the range of frequencies associated with the risetime of the initial step. The value of the steady state skin depth, δ, is thus dictated by frequencies of 25 to 120MHz.

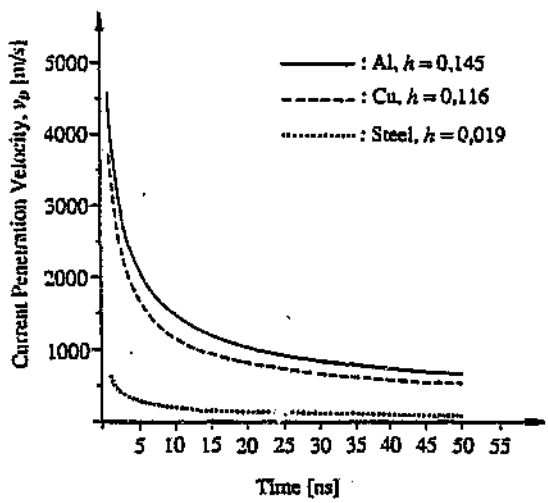


Figure 45 : Velocity of current penetration into a conductive material as a function of time, shown for three materials.

Consequently, concern must be with the time taken for the current to diffuse to a depth of $\leq 17\mu m$ (the steady state skin depth at 25MHz). The depth to which the current has penetrated is shown as a function of time in *figure 46*.

For the system used in this investigation, the risetime of the initial step was in the order of 5ns, implying that δ be set by frequencies of ≥ 100MHz. Under these conditions, δ is $\leq 8{,}5\mu m$. Clearly shown in *figure 5* is the short time (<1ns) taken to reach the steady state skin depth in an aluminium system. While the penetration into the steel is slow, the steady state skin depth is also small. Actual skin effect modelling of current carrying ferromagnetics under transient conditions has not been achieved, and experimental results are limited to the lower frequency ranges (Malewski, 1972).

While the technique illustrated in *figure 44* does present a viable approach to modelling the transient skin effect, it can be seen in the light of the above discussion that, in order to ensure accurate modelling of VFTs with risetimes in the 5-20ns range and having durations of some microseconds, the time constants associated with the skin effect model (and hence the time step Δt) would need to be in the order of one nanosecond. It has also been shown that the steady state skin depth for an aluminium system is reached during a time span equivalent to the risetime of the initial step. Furthermore, inclusion into the model of the effects of coatings is not trivial. All these limit the usefulness of this technique applied to GIS busducts. It nevertheless ensures an appreciation of both the physical processes involved and the limitations of frequency domain modelling of transient events.

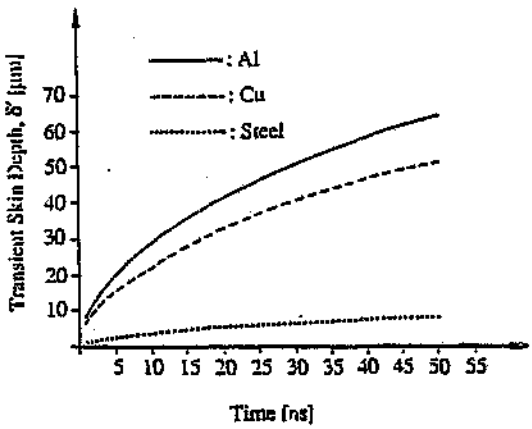


Figure 46 : Depth to which current has diffused into a conductive material, shown as a function of time for three materials.

Consequently, the travelling wave model that has been presented in this work is based on a frequency domain characterisation of the busducts. The nature of the skin effect resistance encountered during transient conditions manifests itself as an enhanced attenuating effect observed during experimentation.

6.5 Concluding Remarks

In reality, therefore, the fields take a finite amount of time to penetrate the conductors. While the assumption that the flux is instantaneously established within the busbars has been found to correlate well with observations made in an aluminium system, in the ferromagnetic case the transient skin effect is prominent. This is an advantage, as the attenuation will be enhanced because the flux penetration is small and the series resistance high.

CONCLUSION

It has been shown both in theory and in the laboratory that a ferromagnetic coating applied to the surfaces of the busbars in a GIS will introduce two effects, the one being largely the result of the other. Primarily, a rise time increase with distance travelled will be introduced. This will lead to a decrease in the peak magnitude of the VFT, as well as a reduction in its severity. This technique, being frequency dependent, allows the design of more robust disconnectors at the expense of more rapid inter-contact voltage collapse.

It has further been shown that coatings need only be applied to the busbars and not also to the inner surface of the outer grounded enclosure.

In order to reach these conclusions, a full frequency domain model of the busduct has been developed. The model allows the effect on the attenuation characteristic of different coatings applied to either one, or both, of the conductors in the system to be studied. The model has been shown to be accurate for a range of different conductors, and has emphasised the importance of the factor $\mu_R\sigma$ as a means of identifying suitable coating materials.

Using the model, various types and sizes of busduct have been characterised in the frequency domain.

Based on this model, a travelling wave model for VFTs has been presented. The Fourier technique has been used to allow the attenuating effects of various materials to be examined.

Laboratory results have shown that, in the case of ferromagnetics, more attenuation than that predicted using the model is recorded. This observation is ascribed to the transient skin effect, where the time taken to establish the steady state currents within the conductors must be accounted for. While this time is negligible for aluminium conductors, it is of great significance in ferromagnetic materials. However, this effect is an advantage in this application.

It must be concluded form this work that, while the proposed technique offers numerous advantages, it may not be economically viable at the time of writing. For example, in January 1988, the cost of the envisaged coating was R2 800 per meter. However, it is not envisaged that an entire GIS should be installed with coated conductors. It would be more appropriate to coat only a few metres on either side of the disconnector, thus attenuating the transient as it travelled towards adjacent sections and coupled equipment. Similarly, the technique could be applied to the busbar between the air bushing and the line trap outside a GIS substation.

The characteristics of suitable materials have been established, but it is concluded that extensive metallurgical research needs to be done before economically viable and suitable materials will be developed.

References

1. Alvinson, Ardito, Boeck, Feser, Fujimoto, Grandl, Koenig, Lightle, Luoni, Luxa, Muller, Rowe, Sabot (1988). "Very fast transient phenomena associated with gas insulated substations." Report by CIGRÉ working groups 33/13-09, August/September 1988.

2. Aron A, Fickert L, Reisinger F, Wais W (1987). "Fourier spectrum as a means of representation and evaluation of transient voltage surges in GIS." Paper 12.04, Fifth International Symposium on High Voltage Engineering, Braunschweig, August 1987.

3. Auriol Ph, Buret F, Helle G, Ma SZ (1988). "Dielectric withstand of SF_6 stressed by steep fronted waves." CIGRÉ paper 15-05, August/September 1988.

4. Banfai Gy, Philippovich Gy (1988). "Experience gained in the installation and operation of gas insulated substations for the 420kV grid." CIGRÉ paper 23-12, August/September, 1988.

5. Bargigia A, Porrino A, Rizzi G, Santagostino G, Mazzoleni B (1984). "Contribution to the choice of the dielectric withstand levels of SF_6 gas insulated substations." CIGRÉ paper 33-13, August/September 1984.

6. Bargigia A, Porrino A, Mazzoleni B, Mosca W, Rizzi G (1988). "Performance of metal clad disconnector and its impact on the insulation design of gas insulated substations." CIGRÉ paper 13-15, August/September 1988.

7. Bickford JP, Doepel PS (1967). "Calculation of switching transients with particular reference to line energisation." Proceedings of the IEE, vol 114, no 4, April 1967.

8. Boeck W, Taschner W, Gorablenkow J, Luxa G, Menten L (1986). "Insulating behaviour of SF_6 with and without solid insulation in case of fast transients." CIGRE paper 15-07. 1986.

9. Boeck W, Witzmann R (1987). "Main influences on the fast transient development in gas-insulated substations (GIS)." Paper 12.01, Fifth International Symposium on High Voltage Engineering, Braunschweig, August 1987.

10. Boeck W (1988). "Twenty years of gas-insulated substations - promises, problems and success of SF_6 applications from 125kV up to 800kV." Elektron, vol 5, no 3, March 1988.

11. Boeck W, Witzmann R (1989). "Critical GIS configurations with respect to VFT." Paper 23.10, Sixth International Symposium on High Voltage Engineering, New Orleans, August/September 1989.

12. Boggs SA, Chu FY, Fujimoto N, Krenicky A, Plessl A, Schlicht D (1982). "Disconnect switch induced transients and trapped charge in gas-insulated substations." IEEE Transactions on Power Apparatus and Systems, vol PAS-101, no 10, October 1982.

13. Boggs SA, Fujimoto N, Collod M, Thuries E (1984). "The modelling of statistical operating parameters and the computation of operation-induced surge waveforms for GIS disconnectors." CIGRÉ paper 13-15, August/September 1984.

14. Bosotti O, Mosca W, Rizzi G, Hashoff L, Kynast E, Luhrmann H (1982). "Phenomena associated with switching capacitive currents by disconnectors in metal enclosed SF_6 insulated switchgear." CIGRÉ paper 13-06, August/September 1982.

15. Bozorth RM (1951). "Ferromagnetics." D van Nostrand Company, Inc, 1951.

16. Branin FH (1967). "Transient analysis of lossless transmission lines." Proceedings of the IEEE (letters), vol 55, November 1967.

17. Cretchley DH, Esterhuizen WL, Ferrero GM (1988). "Design and construction of ESCOM's first 765kV transmission lines." Paper no 2, CIGRÉ Open Conference on EHV Transmission Systems, Johannesburg, October 1988.

18. Dakin TW, Luxa G, Opperman G, Vigneux J, Wind G, Winkelnkemper H (1974). "Breakdown of gases in uniform fields. Paschen curves for nitrogen, air and sulfur hexafluoride." Electra no 32, January 1974.

19. Dommel HW (1969). "Digital computer solution of electromagnetic transients in single- and multiphase networks." IEEE Transactions on Power Apparatus and Systems, vol PAS-88, no 4, April 1969.

20. Dower GT, Spicer AC (1988). "Experience with the erection, operation and maintenance of SF_6 gas insulated substations in Australia and New Zealand." CIGRÉ paper 23-02, August/September 1988.

21. Edlinger A, Mauthe G, Pinnekamp F, Schlicht D, Schmidt W (1984). "Disconnector switching of charging currents in metal-enclosed SF_6-gas insulated switchgear at EHV." CIGRÉ paper 13-14, August/September 1984.

22. Esmeraldo PCV, Salgado Carvalho FM (1988). "Surge propagation analysis: an application to the Grajaú 500kV SF_6 gas-insulated substation." CIGRÉ paper 33-01, August/September 1988.

23. Feng Y, Qiu Y, Song X (1987). "The influence of voltage waveshape on particle initiated breakdown voltages of gaps in SF_6 and SF_6/air mixtures." Paper 15.02, Fifth International Symposium on High Voltage Engineering, Braunschweig, August 1987.

24. Frantz RAJ, Broschk H, Dietschi M, Moyal J, Stentiford K (1990). "Service experience with SF_6 gas insulated switchgear in Southern Africa." Transactions of the SAIEE, vol 81, no 1, March 1990.

25. Frey W, Althammer P (1961). "The calculation of electromagnetic transients on lines by means of a digital computer." The Brown Boveri Review, vol 48, no 5/6.

26. Fujimoto N - Ontario Hydro Research Division (1985). "Transmission line transients analysis." Revision 2.4.0, March 1985.

27. Fujimoto N, Chu FY, Harvey SM, Ford GL, Boggs SA, Tahiliani VH, Collod M. "Developments in improved reliability for gas-insulated substations." CIGRÉ paper 23-11, August/September 1988.

28. Griscom SB, Skooglund JW, Hileman AR (1958). "Analytical studies of overvoltages caused by disconnecting-switch operation." IEEE Transactions on Power Apparatus and Systems, vol PAS-77, 1958.

29. Haack GR (1971). "Comment on 'Transient analysis of lossy transmission lines'." Proceedings of the IEEE (letters), vol 59, June 1971.

30. Hanada CN, Asano M, Borgonovo E, Elli E, Garbero L, Ebersohl G, Voisin G (1984). "Fast transient overvoltages in Porto Primavera 460kV SF_6 insulated substation." CIGRÉ paper 33-14, August/September 1984.

31. Hara M, Tobata H, Hidaka K, Yakabe H (1987). "Influence of conducting particles on insulating performance of conical spacer in SF_6 gas under DC voltage." Paper 15.03, Fifth International Symposium on High Voltage Engineering, Braunschweig, August 1987.

32. Hopkins RA, Ryan LE (1987). "Escom's first 765kV substations - Alpha and Beta. Design aspects relating to substation philosophy with particular reference to employment of GIS." Paper no 5, CIGRÉ Open Conference on EHV Transmission Systems, Johannesburg, October 1987.

33. Jandrell IR, Smart MH (1985). "Generation of pseudo switching impulses." Final year thesis report, University of the Witwatersrand, 1985.

34. Jandrell IR, Reynders JP (1987). "The attenuation of high frequency transient voltages in co-axial SF_6 insulated systems." Paper 12.05, Fifth International Symposium on High Voltage Engineering, Braunschweig, August 1987.

35. Jandrell IR, Reynders JP (1988). "The degradation of undesirable features of disconnect transients by means of a ferromagnetic skin." Transactions of the SAIEE, vol 79, no 2, July 1988.

36. Jandrell IR, Reynders JP (1989). "Travelling wave model for very fast transients in co-axial busducts." Paper 25.07, Sixth International Symposium on High Voltage Engineering, New Orleans, August/September 1989.

37. Jandrell IR, Reynders JP (1990). "A travelling wave model for VFTs, and some laboratory test results." Paper 2.5, South African Universities Power Engineering Conference, Stellenbosch, January 1990.

38. Kawada H, Ando K, Maeda T, Tamura M, Murakami Y, Nitta T (1988). "Application of diagnostic techniques to gas insulated switchgear; Japanese experience and the future." CIGRÉ paper 23-05, August/September 1988.

39. Kobayashi S, Yamagata Y, Nishiwaki S, Okubo H, Kawaguchi Y, Murakami Y, Yanabu S (1987). "Particle-initiated flashover caused by disconnector restriking surges in GIS." Paper 12.03, Fifth International Symposium on High Voltage Engineering, Braunschweig, August 1987.

40. Kynast E, Gorablenkow J, Luxa G, Patrunky H, Moritz G, Henningsen C (1984). "Investigations concerning the switching of disconnectors in an SF_6-insulated 380kV substation." CIGRE paper 33-02, August/September 1984.

41. Lalot J, Sabot A, Kieffer J, Rowe SW (1986). "Preventing earth faulting during switching of disconnectors in GIS including voltage transformer." IEEE Transactions on Power Delivery, vol PWRD-1, no 1, January 1986.

42. Lewis J, Pryor BM, Jones CJ, Irwin T (1988). "Disconnector operations in gas insulated substations. Overvoltage studies and tests associated with a 420kV installation." CIGRÉ paper 33-09, August/September 1988.

43. Liu YK (1968). "Transient analysis of TEM transmission lines." Proceedings of the IEEE (letters), vol 56, June 1968.

44. Lohmann VW, Brinzer R (1987). "World's first 800 kV GIS substation." Brown Boveri Review, vol 10, 1987.

45. Luxa G, Oppermann G, Vigreux J, Winkelnkemper H. "D.- Paschen curve for sulfur hexafluoride (SF_6)." Electra no 32, January 1974.

46. Luxa G, Kynast E, Pigini A, Bargigia A, Boeck W, Hiesinger H, Schlicht S, Wiegart N, Ullrich L (1988). "Recent research activity on the dielectric performance of SF_6, with special reference to very fast transients." CIGRÉ paper 15-06, August/September 1988.

47. Malewski R (1972). "Measurements of transient skin effect within nonlinear conductors." Paper T72 128-2, IEEE Winter Meeting. New York, January/February 1972.

48. Mallary ML (1985). "Conduction of flux at high frequencies in permalloy strips by small-angle rotations." Journal of Applied Physics, vol 57, no 1, April 1985.

49. Miller KW (1947). "Diffusion of electric current into rods, tubes, and flat surfaces." AIEE Transaction, vol 66, 1947.

50. Morf K, Doser B (1987). "New insullation coordination for line traps enhances reliability of PLC transmission." Brown Boveri Review, vol 9, 1987.

51 Nahman NS (1962). "A discussion on the transient analysis of coaxial cables considering high-frequency losses." IRE Transactions on Circuit Theory, vol CT-9, June 1962.

52. Nahman NS, Holt DR (1972). "Transient analysis of coaxial cables using the skin effect approximation $A + B\sqrt{s}$." IRE Transactions on Circuit Theory, vol 19, no 5, September 1972.

53. Nakanishi K, Ueda M, Harumoto Y, Kamiya M, Shiota H, Hosokawa M, Haginomori E, Kuwahura H (1984). "Charging current switching by disconnectors in gas insulated switchgear and some laboratory test methods." CIGRÉ paper 13 06, August/September 1984.

54. Narimatsu S, Yamaguchi K, Nakano S, Maruyama S (1981). "Interrupting performance of capacitive current by disconnecting switch for gas insulated switchgear." IEEE Transactions on Power Apparatus and Systems, vol PAS-100, no 6, June 1981.

55. Nishikawara KK, Cuk N, McCrae GG, Adams PTB (1979). "Specification and application of SF_6 compressed gas insulated switchgear - a utilities point of view." IEEE Paper F79, 74-4, May 1979.

56. Nishiwaki S, Kanno Y, Sato S, Haginomori E, Yamashita S, Yanuba S (1983). "Ground fault by restriking surge of SF_6 gas-insulated disconnecting switch and its synthetic tests." IEEE Transactions on Power Apparatus and Systems, vol PAS-102, no 1, January 1983.

57. Norman HB (1988). "Keynote address." Paper no 1, CIGRÉ Open Conference on EHV Transmission Systems, Johannesburg, October 1988.

58. Ozawa J, Yamagiwa T, Hosokawa M, Takeuchi S, Kozawa H (1986). "Suppression of fast transient overvoltage during gas disconnector switching in GIS." IEEE Transactions on Power Delivery, vol PWRD-1, no 4, October 1986.

59. Ramo S, Whinnery JR, van Duzer T (1967). "Fields and waves in communications electronics." John Wiley and Sons, Inc, Second Printing, January 1967.

60. Relton FE (1965). "Applied Bessel functions." Dover Publications Inc, 1965.

61. Reynders JP, Modry R, Meppelink J (1986). "Breakdown in a coaxial gap with the application of disconnector generated transients." Transactions of the SAIEE, vol 77, no 2, November 1986.

62. Reynders JP, Modry R, Meppelink J (1987a). "Volt-time curves of disconnector generated fast transients inside GIS." Paper 73, Fifth International Symposium on Gaseous Dielectrics, Knoxville, May 1987.

63. Reynders JP, Meppelink J (1987b). "Characteristics of disconnect switch transients and control of the subsequent electromagnetics interference." Paper no 6, CIGRÉ Open Conference on EHV Transmission Systems, Johannesburg, October 1987.

64. Rorden HL, Dils JD, Griscom SB, Skooglund JW, Beck E (1958). "Investigation of switching surges caused by 345kV disconnecting-switch operation." IEEE Transactions on Power Apparatus and Systems, vol PAS-77, 1958.

65. Seshadri S (1971). "Fundamentals of transmission lines and electromagnetic fields." Addison-Wesley Publishing Company, Inc, 1971.

66. Silveira VLA, Mannheimer WA, Braunovic M (1985). "Degradation of Cu-Sn/Pb surface layers on aluminium conductors by the action of an electric current." IEEE Transactions on Components, Hybrids, and Manufacturing Technology, vol CHMT-8, no 3, September 1985.

67. Silvester P (1966). "Modal network theory of skin effect in flat conductors." Proceedings of the IEEE, vol 54, no 9, September 1966.

68. Thione L (1984). "Special report for group 33." CIGRÉ paper 33-00, August/September 1984.

69. Thompson DA (1971). "Exchange eddy-current effects in thick magnetic films." IEEE Transactions on Magnetics, September 1971.

70. Thornley RFM, Kehr WD (1971). "The permeability-frequency response of 4-79 molybdenum permalloy foils." IEEE Transactions on Magnetics, September 1971.

71. van Thoor TJW (Editor) (1970). "Materials and technology volume 3 - metals and ores." Longman and JH De Bussy, 1970.

72. Weber LC, Elliot LC, Smith HM (1958). "Bus switching surges." IEEE Transactions on Power Apparatus and Systems, vol PAS-77, 1958.

73. Weck K-H (1988). "Special report for group 33." CIGRÉ paper 33-00, August/September 1988.

74. Witzmann R (1987). "Fast transients in gas insulated substations (GIS) - modelling of different GIS components." Paper 12.06, Fifth International Symposium on High Voltage Engineering, Braunschweig, August 1987.

75. Yen C-S, Fazarinc Z, Wheeler RL (1982). "Time-domain skin-effect model for transient analysis of lossy transmission lines." Proceedings of the IEEE, vol 79, no 7, July 1982.

Appendix 1 : The Free Charge Term Equals Zero For a Good Conductor

The approximations made here for good conductors are well known, and may be accurately applied in this analysis. Maxwell's equations cannot be derived from any more basic laws, but they are considered accurate only because they adequately predict a variety of electromagnetic phenomena. In order that they may be accurately applied, a number of further fundamental definitions have been established, one being the definition of conductor current:

$$\vec{J} = \sigma \vec{E}$$

where: σ is an intrinsic property of the material.

Thus assuming that the above Ohm's law applies, implies no free charge. As a good conductor may be readily visualised as a material in which free e^- drift through a lattice of immobile positive ions, it is clear that over a given volume the net charge is zero. As current flows, e^- leaving one side of the volume are immediately replaced with e^- entering the opposite side. Consequently, from Maxwell's equations:

$$\nabla \cdot \vec{D} = 0$$

$$\Rightarrow \quad \rho = 0$$

For all good conductors, the loss tangent is well known to be very large, and may be easily defined from Maxwell's equation $\nabla \times \vec{H} = \vec{J} + j\omega\vec{D}$.

Appendix 2 : The Total Current in a Planar Conductor

Ohm's Law:

$$\vec{J} = \sigma \vec{E}$$

$$\therefore \quad \frac{\vec{J}}{\sigma} = \vec{E}$$

where : σ is the conductivity of the material.

The surface electric field intensity, $\vec{E_s}$, is given by:

$$\vec{E_s} = \int \frac{\vec{J_s}}{\sigma} \cdot \vec{dl} \quad [V]$$

where : Closed path $\vec{dl}$ is along the surface of the conductor, in the direction of positive to negative voltage.

$\vec{J_s}$ is the surface current density (not easily visualised in the form of the definition).

In rectangular co-ordinates, for the nomenclature of *figure 10* and *11* (in the text of *chapter 4*), and *figure 4.1* of *appendix 4*, we need only consider the components in the z-direction:

=> the total current flowing in a planar conductor, I_z, is given by:

$$I_z = \int_0^{\infty} J_z dx$$

Appendix 3 : Determination of Equation (4) of *Chapter 4*

From Maxwell's equations, taking the curl:

$$\nabla \times \vec{E} = -\frac{\delta}{\delta t}(\mu\{\nabla \times \vec{H}\})$$

$$\therefore \quad \nabla(\nabla \cdot \vec{E}) - \nabla^2 \vec{E} = -\frac{\delta}{\delta t}\mu(\nabla \times \vec{H})$$

$$= -\frac{\delta}{\delta t}\mu(\sigma + j\omega\epsilon)\vec{E}$$

Since $\nabla \cdot \vec{E} = 0$, and from Ohm's law:

$$-\nabla^2 \frac{\vec{J}}{\sigma} = -\frac{\delta}{\delta t}\mu(\sigma + j\omega\epsilon)\frac{\vec{J}}{\sigma}$$

$$+\nabla^2 \vec{J} = \mu\sigma\frac{\delta}{\delta t}\vec{J}$$

$$\therefore \nabla^2 \vec{J} = j\omega\mu\sigma\vec{J}$$

Appendix 3 : Determination of Equation (4) of *Chapter 4*

From Maxwell's equations, taking the curl:

$$\nabla \times \vec{E} = -\frac{\delta}{\delta t}(\mu\{\nabla \times \vec{H}\})$$

$$\therefore \quad \nabla(\nabla \cdot \vec{E}) - \nabla^2\vec{E} = -\frac{\delta}{\delta t}\mu(\nabla \times \vec{H})$$

$$= -\frac{\delta}{\delta t}\mu(\sigma + j\omega\varepsilon)\vec{E}$$

Since $\nabla \cdot \vec{E} = 0$, and from Ohm's law:

$$-\nabla^2\frac{\vec{J}}{\sigma} = -\frac{\delta}{\delta t}\mu(\sigma + j\omega\varepsilon)\frac{\vec{J}}{\sigma}$$

$$+\nabla^2\vec{J} = \mu\sigma\frac{\delta}{\delta t}\vec{J}$$

$$\therefore \nabla^2\vec{J} = j\omega\mu\sigma\vec{J}$$

Appendix 4 : Field Penetration into a Homogeneous Planar Conductor

Consider the following plane conductor:

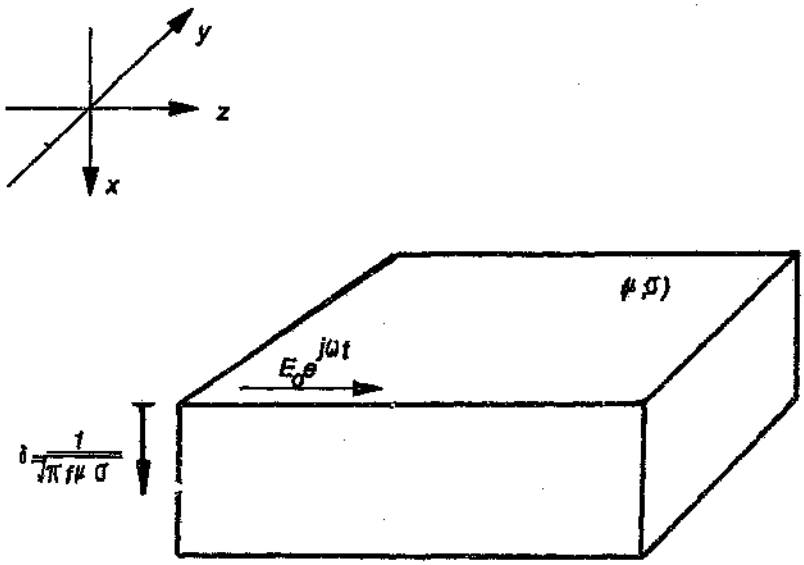


Figure 4.1 : Plane conductor with orientation of axes as used in the development of the model shown.

$$\vec{J} = \sigma\vec{E}$$

This is Ohm's law. Thus for the uniform field situation shown here, and with the electric field vector in the z direction as shown, there are no variations with y or z. That is, for vector $\vec{E}$, given in rectangular co-ordinates by:

$$\vec{E} = (E_x, E_y, E_z)$$

only the component in the z direction, E_z, concerns us. From Ramo (1967):

$$\frac{d^2E_z}{dx^2} = j\omega\mu\sigma E_z \qquad (4\text{-}1)$$

$$= \tau^2 E_z$$

where : $\tau^2 = j\omega\mu\sigma$

$$\therefore \quad \tau = (1+j)\sqrt{\pi f\mu\sigma}$$

$$= \frac{1+j}{\delta}$$

and : $\delta = \frac{1}{\sqrt{\pi f \mu \sigma}}$

δ is recognized as the simple "skin depth" for the particular material characterised by μ and σ.

The complete solution of (4-1) is in the form:

$$E_z = Be^{-\alpha x} + Ce^{\alpha x}$$

By inspection, $C = 0$, as E_z cannot be infinite at $x = \infty$.

It is easily shown from equation (1) above and with the boundary condition $E_z = E_o$ at $x = 0$ that (see also *chapter 4*, and *appendix 3*):

$$E_z = E_o e^{-\frac{x}{\delta}} e^{-j\frac{x}{\delta}} \qquad (4\text{-}2)$$

and

$$H_y = H_o e^{-\frac{x}{\delta}} e^{-j\frac{x}{\delta}} \qquad (4\text{-}3)$$

$$J_z = J_o e^{-\frac{x}{\delta}} e^{-j\frac{x}{\delta}} \qquad (4\text{-}4)$$

where : E_o = magnitude of the electric field at the conductor surface (as shown in the above figure).

H_o = magnitude of the magnetic field at the conductor surface.

J_o = magnitude of the current density at the conductor surface.

Therefore, from equations (4-2), (4-3) and (4-4), it is seen that the magnitudes of the fields and the current density decay exponentially with penetration into the conductor, and that δ has the significance of being the depth at which they have decayed to about 36,9% of their original (surface) value. Hence the definition of δ as the skin depth. Furthermore, we consider this to be the "simple" skin depth, as the conductor under consideration is homogeneous (as opposed to being made up of layer of material with different characteristics). In order to comply with accepted definition of surface impedance, we must now consider a surface area of 1m by 1m in extent. The surface impedance is considered for a unit width and unit length of a material. (For this reason, the surface resistance of materials, R_S, is often given in "Ohms per square" although its units are Ohms.)

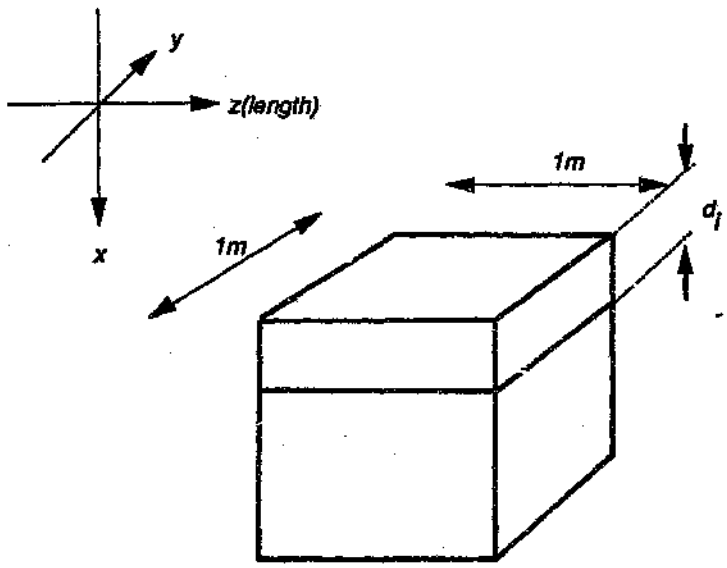


Figure 4.2 : A 1m by 1m block of coated material of infinite depth.

The internal impedance term per unit length, is the quotient of the electric field at the surface and the total current flowing within the (volume under consideration) conductor. The total current flowing in the plane conductor is found by integrating the current density, J_z of equation (4-4), from the surface of the conductor to an infinite depth. From *figure 4.2*:

$$\begin{aligned} I_z &= \int_0^{\infty} J_z dx \\ &= \int_0^{\infty} J_o e^{-\frac{(1+j)}{\delta}x} dx \\ &= \frac{J_o \delta}{1+j} \end{aligned} \qquad (4\text{-}5)$$

And, from Ohm's law, the electric field at the surface is given by:

$$E_{xo} = \frac{J_o}{\sigma} \qquad (4\text{-}6)$$

Therefore, from (4-5) and (4-6), the internal impedance (for unit width and unit length) is:

$$Z_S = \frac{E_{xo}}{I_z} = \frac{1+j}{\sigma\delta}$$

$$\therefore \quad Z_S = (1+j)\sqrt{\frac{\pi f \mu}{\sigma}}$$

From the real part of the equation for skin depth, δ, it is seen that the skin effect resistance of the plane conductor is exactly equal to the DC resistance of a plane conductor of depth δ. In *chapter 4* this analysis is extended to include a coating of thickness *d* on the surface of the semi-infinite plane. It is then further extended in order to model the internal impedance per unit length of a coaxial transmission line.

Appendix 5 : Data Requirement for the Program *Skin*

The program *Skin* is used to determine the propagation factor for variously defined co-axial systems. The output of the program is typically a plot of attenuation (generally in the units of $dB \cdot m^{-1}$) versus frequency [Hz]. In order the run the program, it is necessary to produce a data file of the following form:

1. testing [1 => f; 2 => t] {if testing is true, then a diagnostic printout runs during the program operation}

2. plotting [1 => f; 2 => t] {if plotting is true, then the output data is formatted for plotting attenuation [dB/m] versus frequency [MHz]}

3. time analysis [1 => f; 2 => t] {if time analysis is true, then the program interactively prompts the user in order to conduct a pulse or surge response study of the single section of busduct to be examined}

4. starting frequency [Hz] {The lowest frequency of interest in the analysis}

5. inner busbar coating conductivity [S/m]

6. inner busbar conductivity [S/m]

7. inner busbar coating relative permeability

8. inner busbar relative permeability

9. inner busbar coating thickness [m] {in the case where no coating is applied, this value would be entered as 0}

10. outer grounded enclosure coating conductivity [S/m]

11. outer groundcd enclosure conductivity [S/m]

12. outer grounded enclosure coating relative permeability

13. outer grounded enclosure relative permeability

14. outer grounded enclosure coating thickness [m] {in the case where no coating is applied, this value would be entered as 0}

15. inner busbar radius [m] {important in the determination of the external impedance terms}

16. outer grounded enclosure inner radius [m] {must be the inside radius of the enclosure as this is the surface into which the fields penetrate}

{The following input data can be entered interactively, and pertains to the time domain analysis of a single section of busduct. Note the definition of the input waveform in order to accord with the periodic nature of the Fourier technique}

17. line length [m] {note that this is the length of a continuous section of duct over which the response is to be determined in the time domain}

18. time between pulses [s] {refer to *appendix 7*}

19. pulse duration [s] {refer to *appendix 7*}

20. magnitude of pulse [kV]

21. frequency component limi i the harmonic content of the frequency domain analysis}

22 time component limit {sets the number of time domain samples in the calculations}

23. transmission coefficient {if the is a mismatch between the measuring circuit and the system under test, this frequency independent coefficient corrects the results for the influence of the mismatch}

The program *Skin* is simple to run, and executes accurately and efficiently. A more detailed description of its operation is to be found in *chapter 5*. The program is listed below. Irrelevant sections of code have been deleted. The choice of variable name and the nature of the language *Pascal* ensure that the code is easily understood. Indeed, the form of all input and output files is quickly established by glancing st the relevant procedures.

Appendix 6 : Consideration of the Bessel Function Solution

In order to accurately (and absolutely correctly) solve for the internal impedance term (ie the skin effect impedance) of a co-axial system, it is necessary to define the system in cylindrical co-ordinates. This generates equations which may be solved in terms of modified Bessel functions for the busbar, and modified Hankel functions for the outer grounded enclosure (Ramo, 1967). In order to establish methodically the accuracy of the planar approximation in the application suggested in this work, the inner busbar was defined in cylindrical co-ordinates in the case where no coating was applied. This produces a "Bessel" type equation solvable in Bessel functions. Also, the results of this analysis were compared to those obtained from the planar model in order to:

- Determine the lower frequency limit of accuracy of the planar approximation
- Develop a correction factor in order to extend the lower range of accuracy of the planar model

While the actual analysis is tedious, the pertinent results will be tabulated, conclusions drawn and comparisons made with well established published results. Thus in order to compare the performance of the planar model at different frequencies for a solid busbar, we use as a parameter the ratio of busbar radius to depth of penetration as recommended by Ramo (1967):

$$\frac{r_i}{\delta}$$

The equations for the uncoated case are well known, and are as follows: For the system defined in cylindrical co-ordinates:

$$\frac{J_z}{J_o} = \left\{ \frac{Ber\left(\frac{\sqrt{2}r}{\delta}\right) + jBei\left(\frac{\sqrt{2}r}{\delta}\right)}{Ber\left(\frac{\sqrt{2}r_i}{\delta}\right) + jBei\left(\frac{\sqrt{2}r_i}{\delta}\right)} \right\}$$

where : the symbols have their usual significance (Relton, 1965).

For the system defined in planar co-ordinates:

$$\frac{J_z}{J_o} = e^{-\frac{(r_i - r)}{\delta}} e^{-j\frac{(r_i - r)}{\delta}}$$

All the calculations were conducted for a BBC size BG2 busduct, with $r_i = 55$mm. This size was selected as it represents the realistic smallest radius of interest in this work. For the various values of r_i/δ the magnitude of the ratio of current density evaluated at some radius, r, to that at the surface is determined (refer to *figure 6.1*):

$$\left| \frac{J_z}{J_o} \right|$$

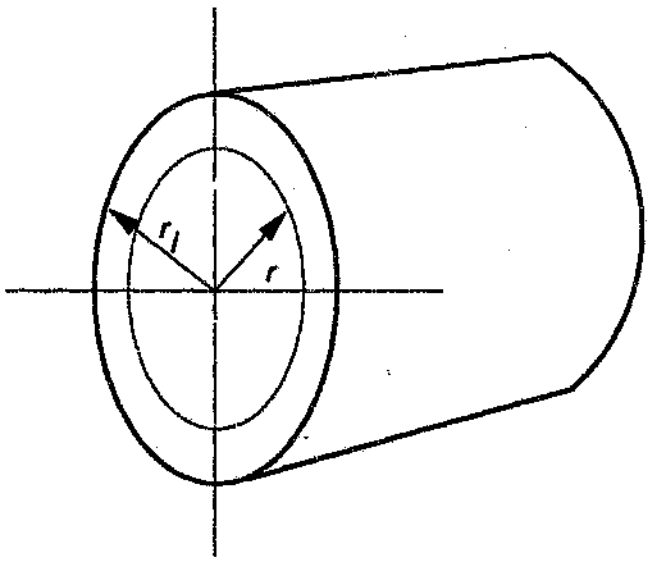


Figure 6.1 : A solid busbar defining the variable *r*.

Also evaluated is the angle of the ratio of the current density evaluated at radius r to the current density at the surface:

$$\angle \frac{J_z}{J_o}$$

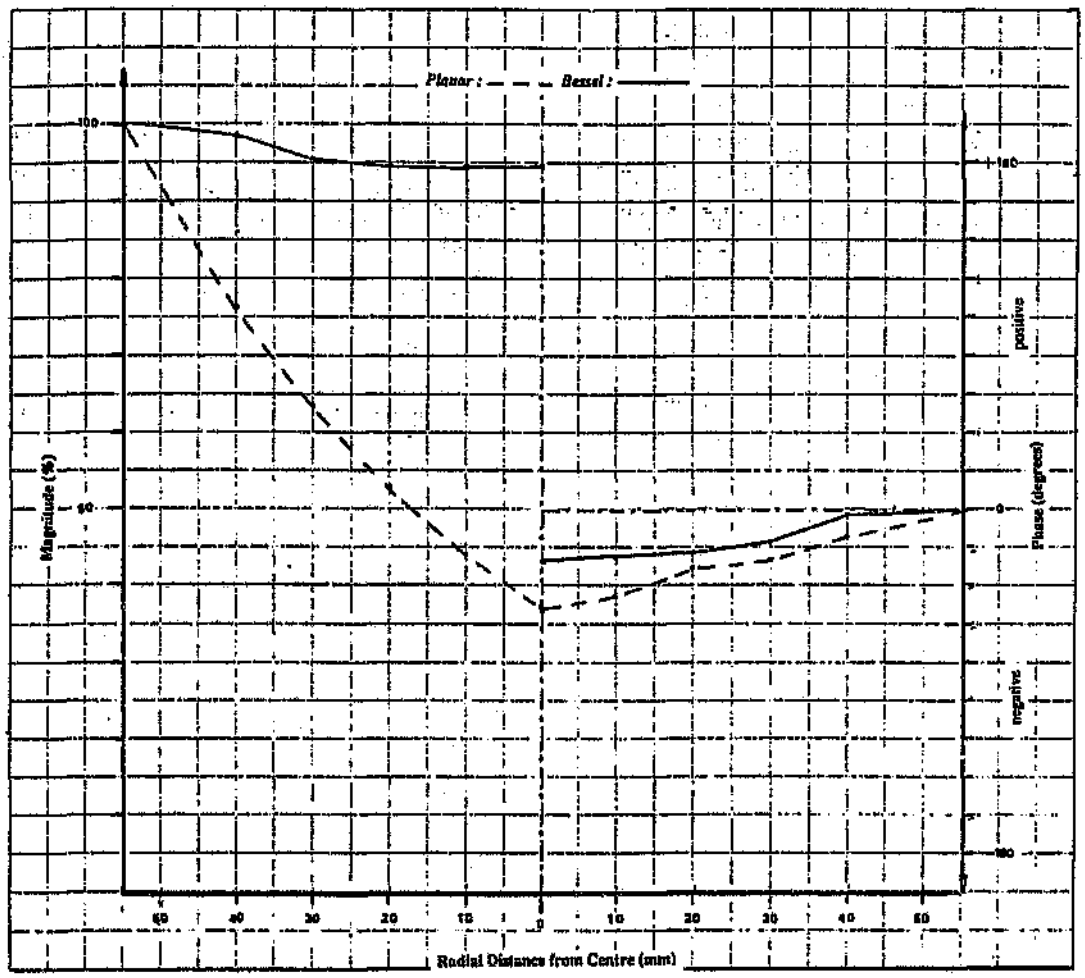


Figure 6.2 : Comparison of planar and bessel solution for $\frac{r}{\delta} = 1$, f = 2,39 Hz and $\delta = 0,055$m.

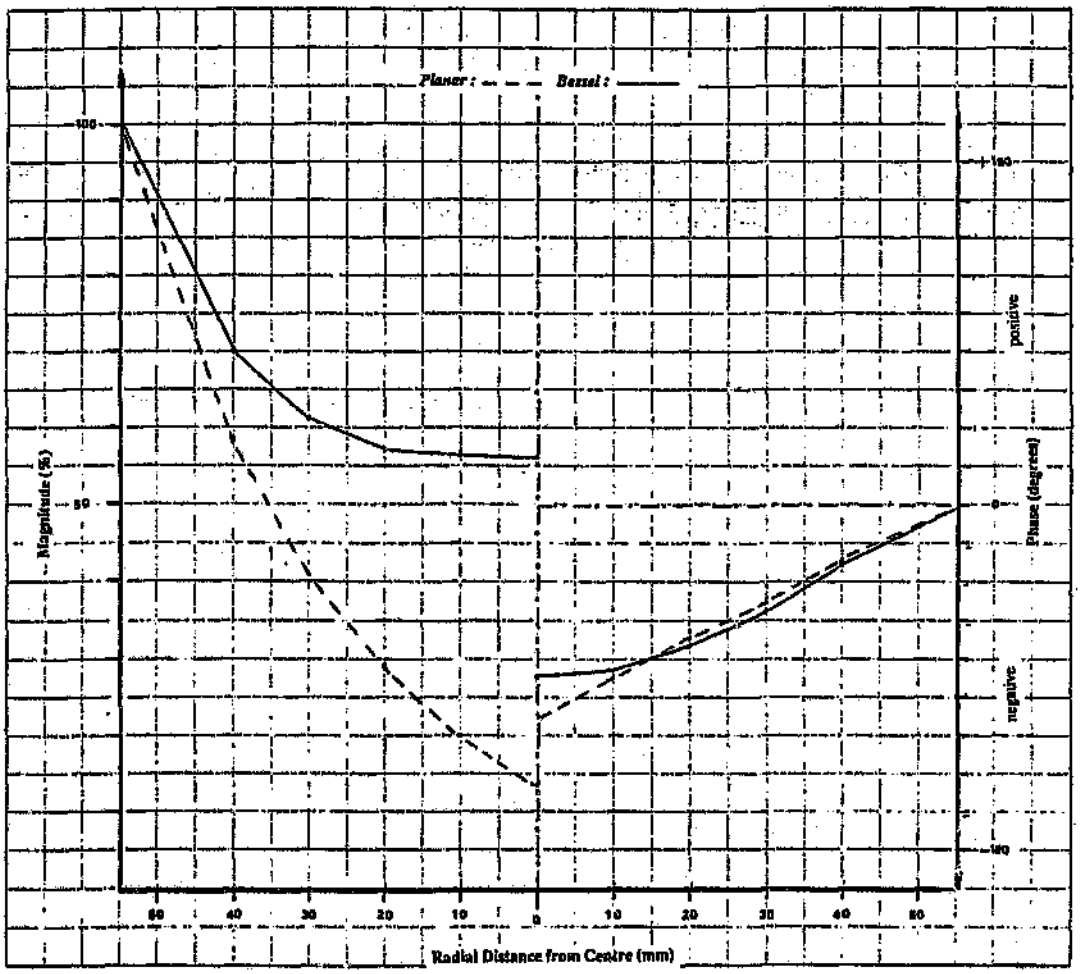


Figure 6.3 : Comparison of planar and bessel solution for $\frac{r_1}{\delta} = 2$, f = 9,56 Hz and $\delta = 0,028$m.

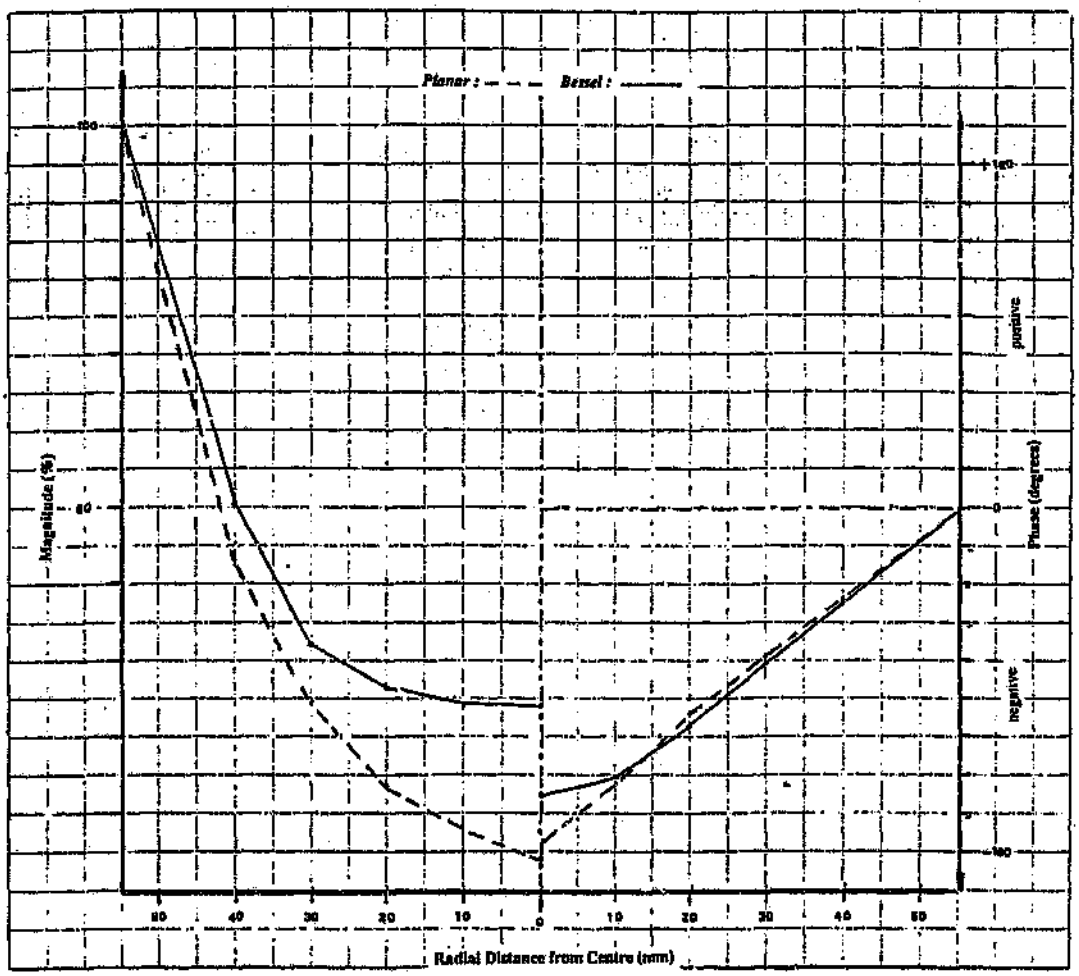


Figure 6.4 : Comparison of planar and bessel solution for $\frac{r_1}{\delta} = 3$, f = 21,53 Hz and $\delta \approx 0,018$m.

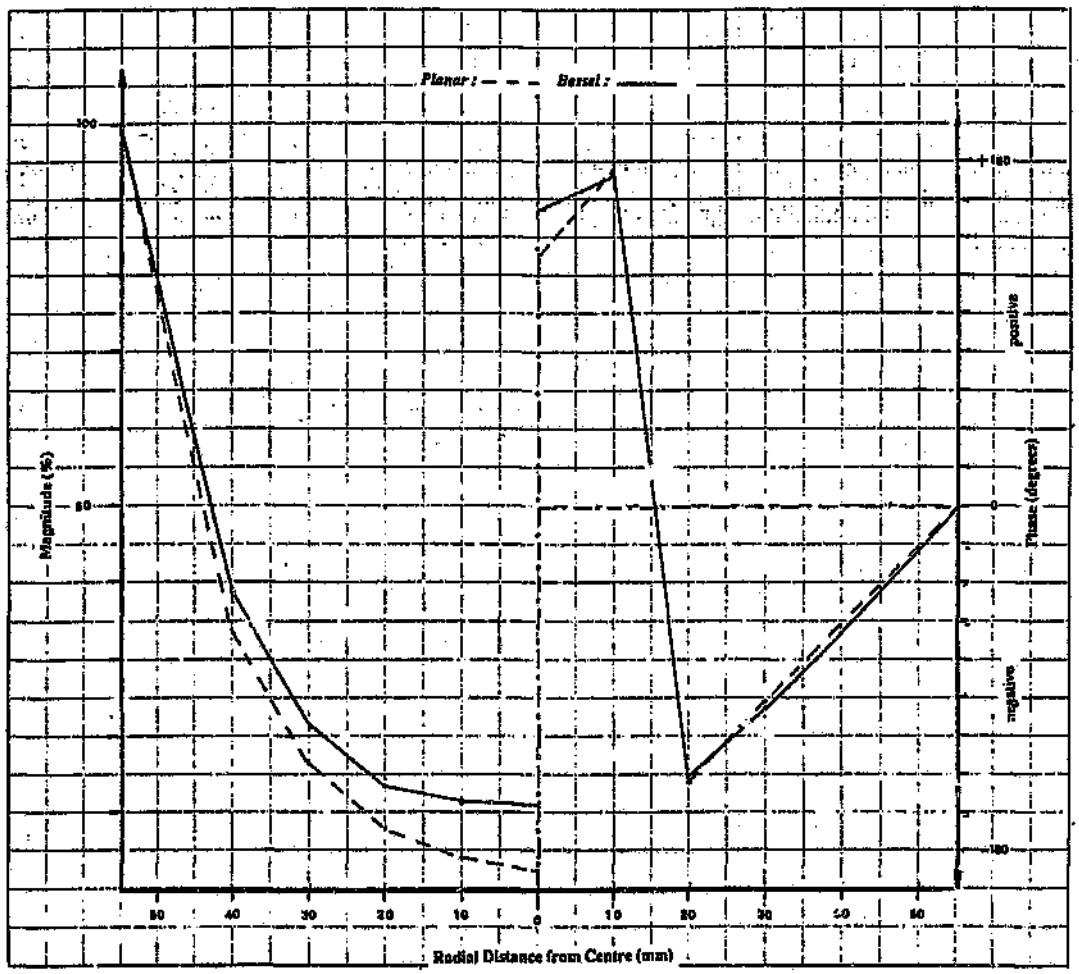


Figure 6.5 : Comparison of planar and bessel solution for $\frac{r_j}{\delta} = 4$, f = 38,27 Hz and $\delta = 0,014$m.

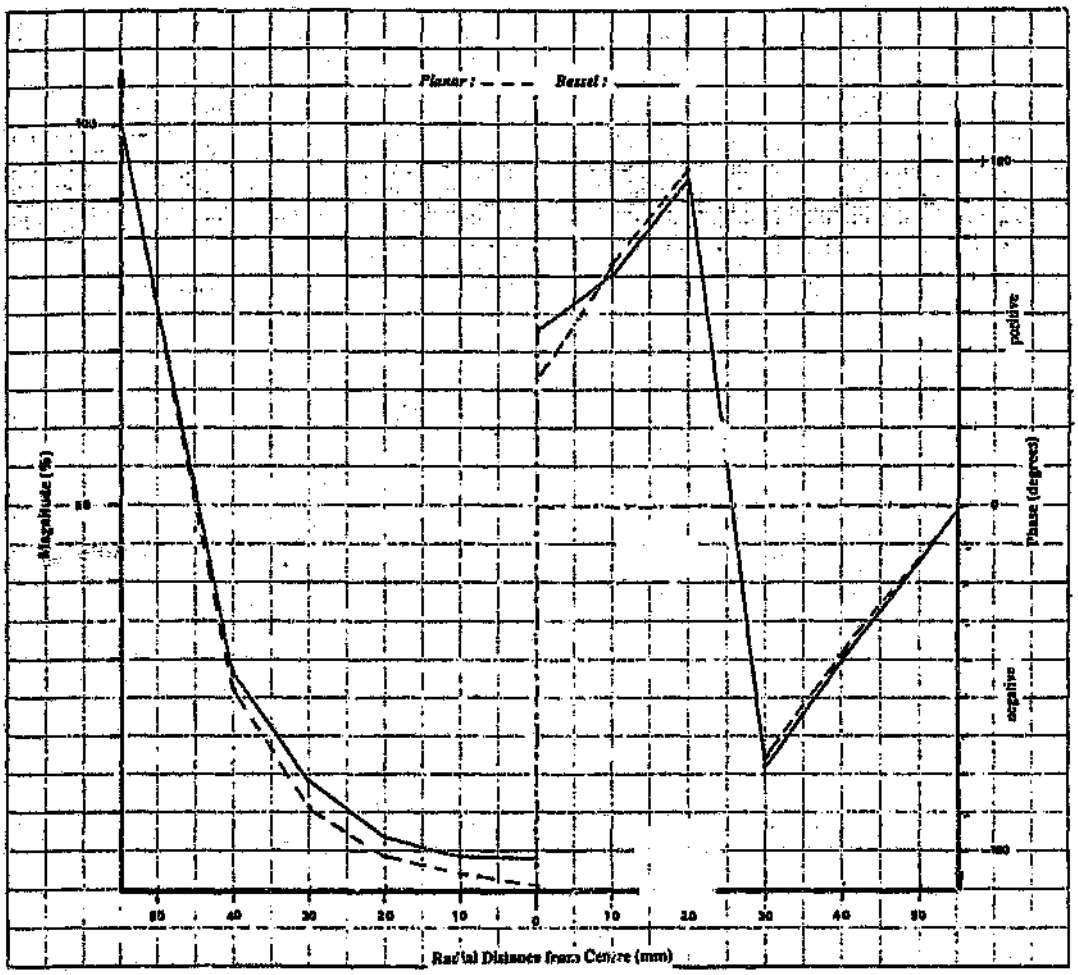


Figure 6.6 : Comparison of planar and bessel solution for $\frac{r_i}{\delta} = 5$, f = 59,76 Hz and $\delta = 0,011$m.



Figure 6.7 : Comparison of planar and bessel solution for $\frac{\gamma}{\delta} = 6$, f = 86,10 Hz and $\delta = 0,009$m.



Figure 6.8 : Comparison of planar and bessel solution for $\frac{r_i}{\delta}=7$, f = 117,20 Hz and $\delta = 0,008$m.

From the comparisons between the Bessel solutions and the planar approximations shown in *figures 6.2 through 6.9*, it is easily shown that the maximum difference between the two is 10% at a frequency of 35Hz. Consequently, if an error of 10% can be tolerated, the planar solution can be safely used down to 35Hz. At 35Hz. $\delta = 14,4$mm. The ratio of r_i to δ is then 3,83. Here the percentage error is defined in terms of the value at the surface, ie:

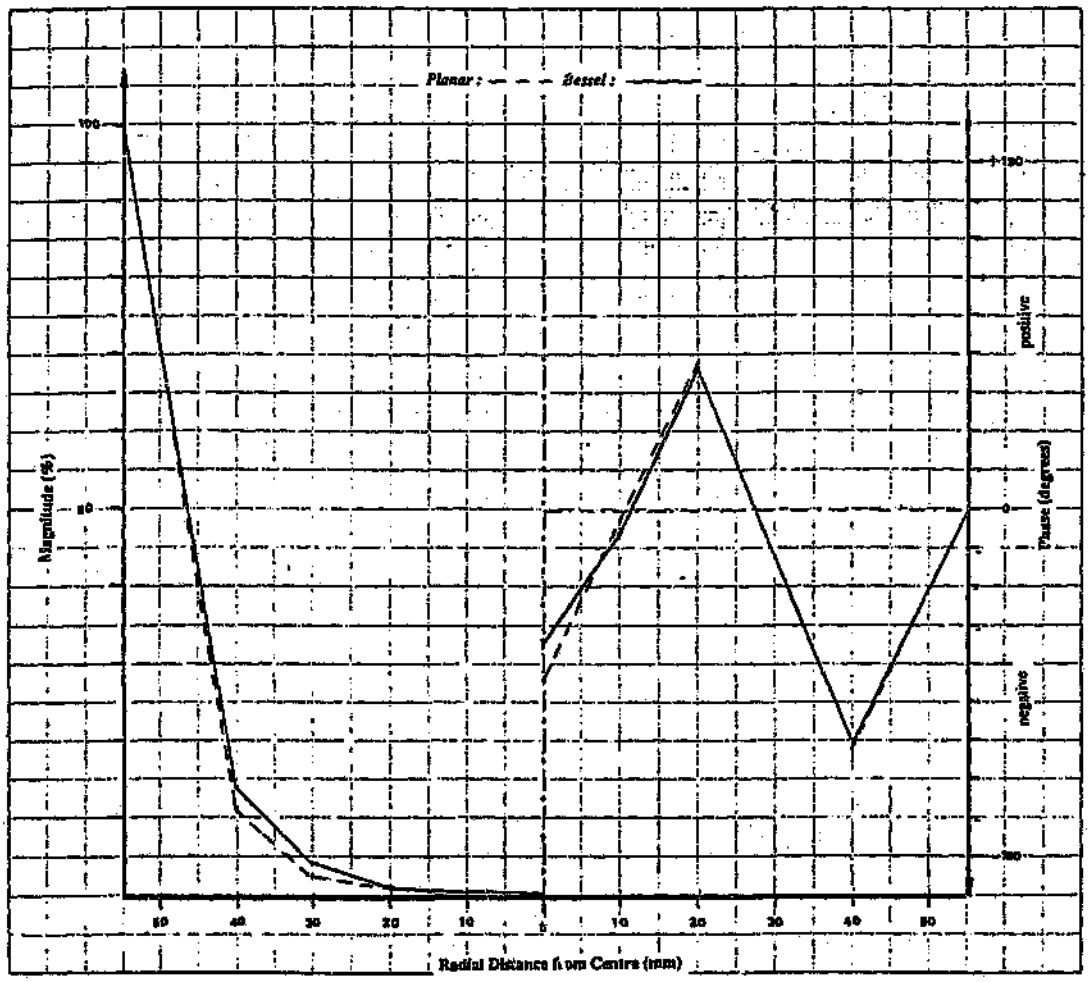


Figure 6.9 : Comparison of planar and bessel solution for $\frac{r_1}{\delta} = 8$, $f \approx 153{,}07$ Hz and $\delta = 0{,}007$m.

$$\text{Error} = \frac{|J_{z(\text{Bessel})}| - |J_{z(\text{planar})}|}{|J_o|} \times 100 \quad [\%]$$

A further very important consideration is the fact that the trans' ,on for the DC value of resistance, Rd, to the higher frequency value given by the real part of $z(s)$ is not automatically defined by the planar solution. It is defined in the cylindrical solution. In order to extend the low frequency range of the planar model, Ramo (1967) suggests a correction equation of the form:

$$\Re\{z(s)\} = Rd + 1/48\left(\frac{r_1}{\delta}\right)^4$$

They obtain this result from a series expansion of the correct results. However, a more accurate and conveniently found solution is of the following form:

$$\Re\{z(s)\}_{\text{Bessel}} = \zeta \cdot Rd + \Re\{z(s)\}_{\text{planar}}$$

where : ζ is a correction factor determined from the results tabulated below. The table was, as before, produced for a BBC size BG2 busduct. At 10Hz the error is minimal, but below that the correction is no longer adequate. In order to bound the error to within 5%, this correction is included in the model for all frequencies up to 200Hz. No correction for the imaginary component has been considered.

The planar solution equations are easily obtained from *chapter 4*, while the following equation (Ramo, 1967) was used to determine the internal resistance term for the cylindrically defined system:

$$\Re\{z(s)\} = \sqrt{\frac{\pi f \mu}{\sigma}} \frac{1}{\sqrt{2}\pi r_i} \left\{ \frac{Ber\left(\frac{\sqrt{2}r_i}{\delta}\right) Bei'\left(\frac{\sqrt{2}r_i}{\delta}\right) - Bei\left(\frac{\sqrt{2}r_i}{\delta}\right) Ber'\left(\frac{\sqrt{2}r_i}{\delta}\right)}{\left(Ber'\left(\frac{\sqrt{2}r_i}{\delta}\right)\right)^2 + \left(Bei'\left(\frac{\sqrt{2}r_i}{\delta}\right)\right)^2} \right\}$$

where : The symbols have their usual significance (Relton, 1965).

Table 6.1 : Tabulated comparison between the real component predicted by the planar solution and the Bessel solution leading to the determination of a suitable correction factor.

$\frac{R_{Bessel}}{R_d}$	Frequency Hz	Skin depth (δ)m	R_{Bessel} $\mu\Omega \cdot m^{-1}$	$\Re\{z(s)\}$ (R_{planar}) $\mu\Omega \cdot m^{-1}$	Correction factor ζ
1,000	0	∞	-	3,006	0,000
1,021	1	0,085	3,069	0,972	0,698
1,010	2	0,060	3,035	1,375	0,552
1,102	5	0,038	3,314	2,173	0,380
1,162	7	0,032	3,494	2,572	0,307
1,249	9	0,028	3,753	2,916	0,278
1,283	10	0,027	3,856	3,073	0,260
1,510	15	0,022	4,539	3,765	0,257
1,711	20	0,019	5,142	4,346	0,265
2,047	30	0,016	6,153	5,374	0,276
2,317	40	0,013	6,964	6,147	0,272
2,555	50	0,012	7,681	6,873	0,269
2,966	70	0,010	8,917	8,132	0,261
3,500	100	0,009	10,52	9,720	0,266
4,225	150	0,007	12,70	11,90	0,266
4,830	200	0,006	14,52	13,75	0,256
5,369	250	0,005	16,41	15,37	0,256
6,307	350	0,005	18,96	18,18	0,259
7,116	450	0,004	21,39	20,67	0,256

With reference to *table 6.1*, and for satisfactory results, a value of $\zeta = 0,256$ is suggested.

While the above has only accounted for the uncoated busbar of a busduct, the influence of the outer grounded enclosure is easily incorporated (assuming it to be made from the same uncoated material). If we denote $\Re\{z(s)\}_{\text{busbar}}$ by R_i, and $\Re\{z(s)\}_{\text{outer grounded enclosure}}$ by R_g, then:

$$\frac{R_i}{R_g} \propto \frac{r_g}{r_i}$$

It should furthermore be stressed that, for this analysis, it is not important to account for the coating material, as the coating should only being to exert its influence at frequencies in the kHz range. The substrate material dominates the impedance characteristics of the system at the lower frequencies. The inclusion of the correction factor ζ allows us to use this model to very accurately characterise typical high voltage busducts in the frequency domain. It also allows us the knowledge that the time domain simulation, limited in its lowest frequency by our choice of repetition frequency, gives an accurate indication of the system response for the frequencies of interest.

Appendix 7 : Time Domain Definition Used in the Fourier Technique

It is certainly not the purpose of this appendix to discuss the Fourier transform; instead it is important to define the parameters used during the running of the program *Skin*. It is also important to note our decision to define the rising edge (of both the pulse and the surge) as a sinusoidal half cycle. In our experience this closely matched the rising edge of the transients recorded in the laboratory. The surge defined in this appendix is also used in the travelling wave model discussed in a later chapter.

In both waveforms:

- T_r represents the risetime of the waveform, this being a half cycle of the defining sinusoid.
- T_b represents the time between the rising edges of the pulses of surges. This time defines the fundamental frequency of the periodic waveform used in the time domain analysis.

For the surge waveform only:

- T_d represents the duration of the surge voltage. This is an important consideration, as in the travelling wave model the time interval during which observations are to be made, the surge must remain at its peak value. In order to define the negative surge also used in the travelling wave model, the constants defining the surge become negative.

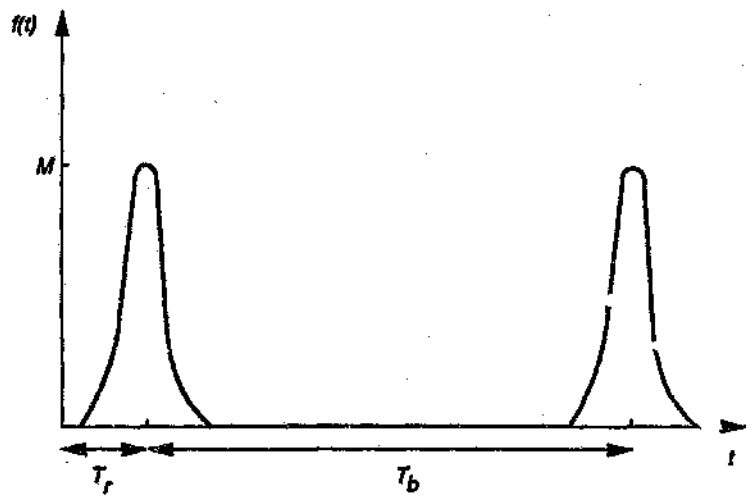


Figure 7.1 : Definition of the pulse used in the model, particularly for the Fourier time domain definition.

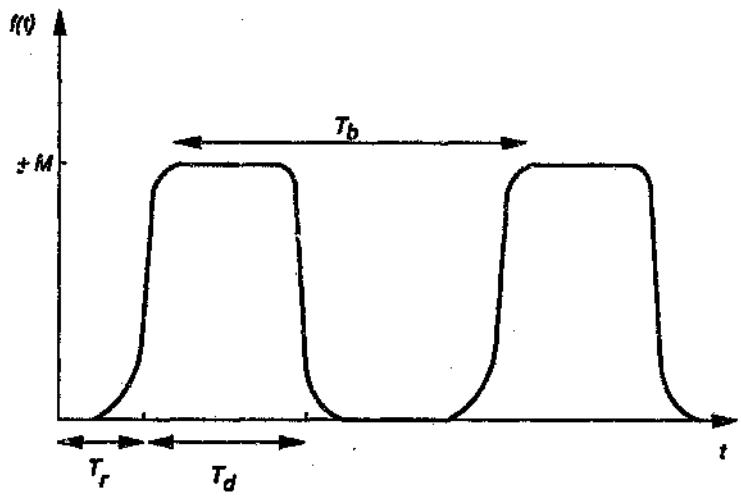


Figure 7.2 : Definition of the surge used in the model, particularly for the Fourier time domain definition.

Appendix 8 : Low Voltage Experimental Results

A number of experiments were conducted on scaled down laboratory test rigs. The details of the rigs are to be found in *chapter 4*.The test rigs had the following dimensions:

- All aluminium system:

  $r_i = 5,18\text{mm}$

  $r_g = 22,2\text{mm}$

- All mild steel system:

  $r_i = 5,13\text{mm}$

  $r_g = 22,1\text{mm}$

- Copper busbar (the aluminium grounded enclosure of the all aluminium systems was used for the copper system):

$r_i = 6,11\text{mm}$

The physical attributes of the materials used were determined as described in *appendix 12*. In all the experiments the same experimental equipment and procedure was used:

- *Oscilloscope* : Tektronix 7834 storage oscilloscope with 400MHz frame bandwidth.
- *High impedance input amplifier* : Tektronix 7A16 with 200MHz bandwidth.
- *Time base* : Tektronix 7B85 with 400MHz bandwidth.
- 50Ω *termination* : Tektronix 011-0049-01, 2W.
- *Pulse generator* : Hewlett Packard 8004A, repetition rate of 0,909MHz and pulse width of 8ns.
- *High impedance probe* : Tektronix P6106 with a 10MHz bandwidth. This probe was inadequate, and disallowed accurate recordings being made for the pulse under consideration in these experiments.

In order to overcome the mismatch between the 50Ω measuring circuit and the test rig, the overall transfer coefficient between the source and the scope was determined and incorporated in the simulation in order to account for the reflections at the discontinuities. It is thus necessary to account for the initial reflection of the pulse as it reaches the test rig. A determined portion appears on the scope, and another determined portion travels into the rig. The returned pulse then again reaches the source end, and a further determined portion appears on the scope. If all the characteristic impedances of the system are known, it is a simple matter to calculate the overall transfer coefficient. See *figure 8.1*, where an example is considered.

In order to determine the characteristic impedance of the test rig, the well known frequency independent equation for a co-axial system was used:

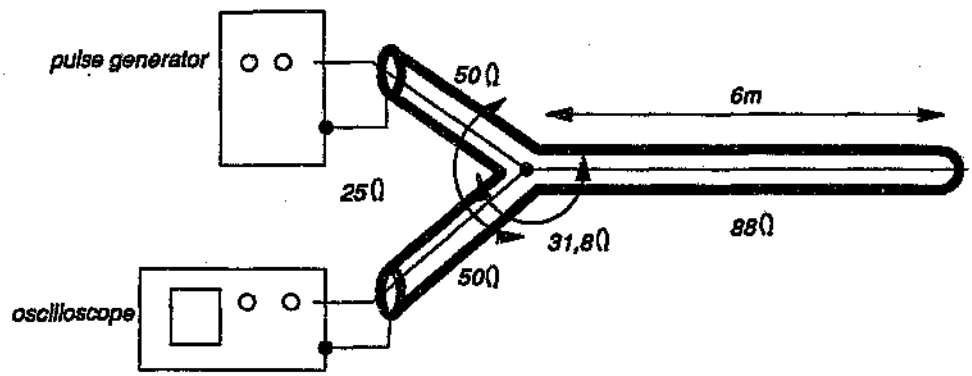


Figure 8.1 : The test circuit used, indicating the various characteristic impedances.

$$Z_o = 138 \log\left(\frac{r_o}{r_i}\right)\Omega$$

In all these cases, the test rig was 6m long. This implies that the pulse would travel for 12m within the test rig. Predictions in the time domain were thus based on a 12 m length of duct. It should be noted that, because of the low voltages used in these experiments, a low field value of μ_R of 50 was used in the study to the nickel coated copper busbar (Seshadri, 1971). The results of the predictions and the records may be found in *chapter 4*. In that chapter, the results are shown corrected for the transfer coefficient. The *figures 8.2* and *8.3* show the predicted results without the transfer coefficient accounted for in the case of the copper system. Plots for both the coated and uncoated cases are shown.

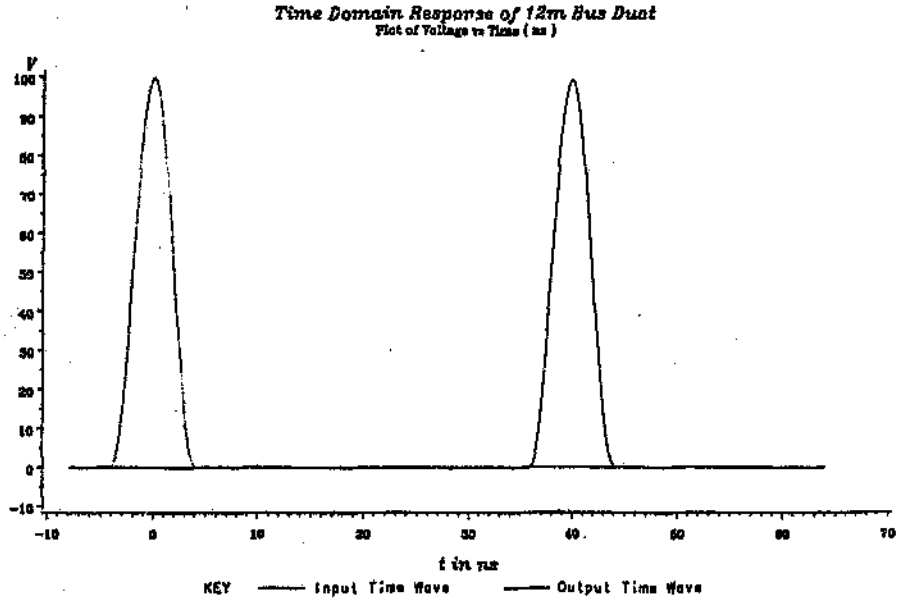
Description : Time domain plot of Cu bar within Al grounded shield. r_1 = 5.11e^{-3}, r_2 = 2.21e^{-2}. Plot shows actual response within the length of Bus Duct.

Inner Bus Conductivity : 5.8e^{7} S/m

Inner Bus Rel Perm : 1

Outer Shield Conductivity : 3.54e^{7} S/m

Outer Shield Rel Perm : 1



Output of program SKIN

Figure 8.2 : Uncoated case with system characteristics as described in the figure.

A further experiment was conducted using a length of RG-58 C/U co-axial cable. Recall from *appendix 6* that the physical dimensions of the system under consideration, particularly the ratio of r_i/δ, has a marked influence upon the accuracy of the model.

Using a Mitutoyo micrometer (serial no 5244529) the dimensions shown in *figure 8.4* were found to apply to the cable:

Description : Time domain plot of Cu bar within Al grounded shield, $r_1 = 8,11e^{-3}$, $r_2 = 2.21e^{-2}$. Nickel Coating is applied to the Cu bar. Plot shows actual response within the length of Bus Duct.

Inner Bus Coating Conductivity : $1,4e^{7}$ S/m

Inner Bus Conductivity : $5,8e^{7}$ S/m

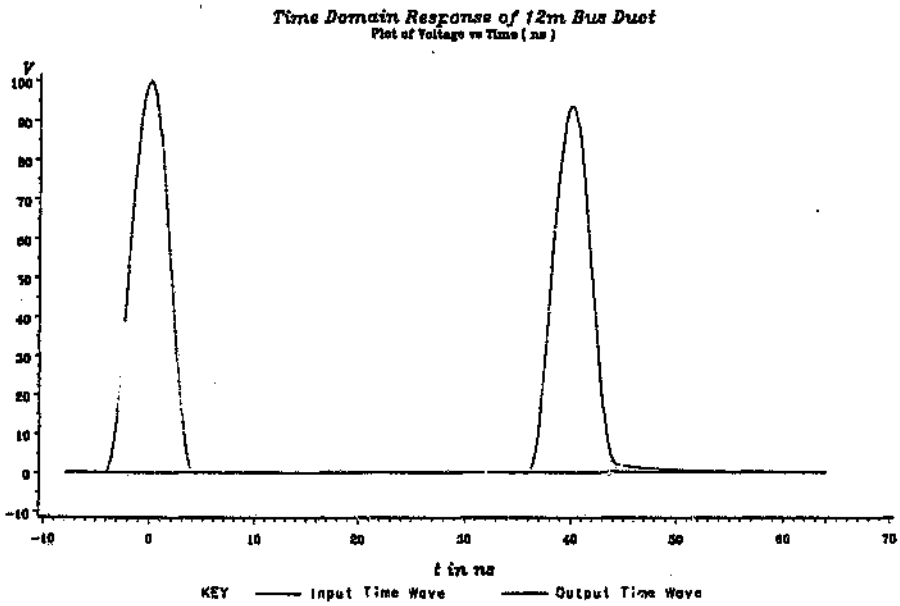
Inner Bus Coat Rel Perm : 50 (low field)

Inner Bus Rel Perm : 1

Coating Thickness : $20e^{-6}$ m

Outer Shield Conductivity : $3.54e^{7}$ S/m

Outer Shield Rel Perm : 1



Output of program SKIN

Figure 8.3 : Coated case with system characteristics as described in the figure.

Furthermore:

- Dielectric is polyethelene, $\varepsilon_R = 2,3$
- Conductors are copper, with $\sigma = 5,7 \times 10^7 S \cdot m^{-1}$
- Furthermore, each filament is 0,174mm thick, and each is tinned

The model developed in this work cannot account for each individual filament. Instead, we assume a solid copper conductor coated with a 10μm layer of tin It should be further stressed that the coating thickness was not measured. Instead it was determined from published data on the frequency domain performance of the cable (refer to *figure 8.5*). Furthermore, predictions of the pulse attenuation were made over a range of coating thicknesses.

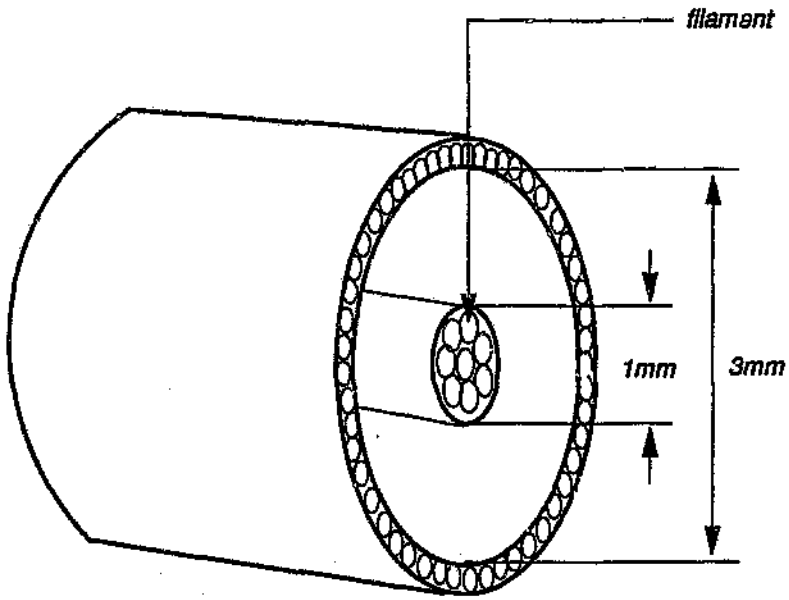


Figure 8.4 : Representation of a typical co-axial conductor.

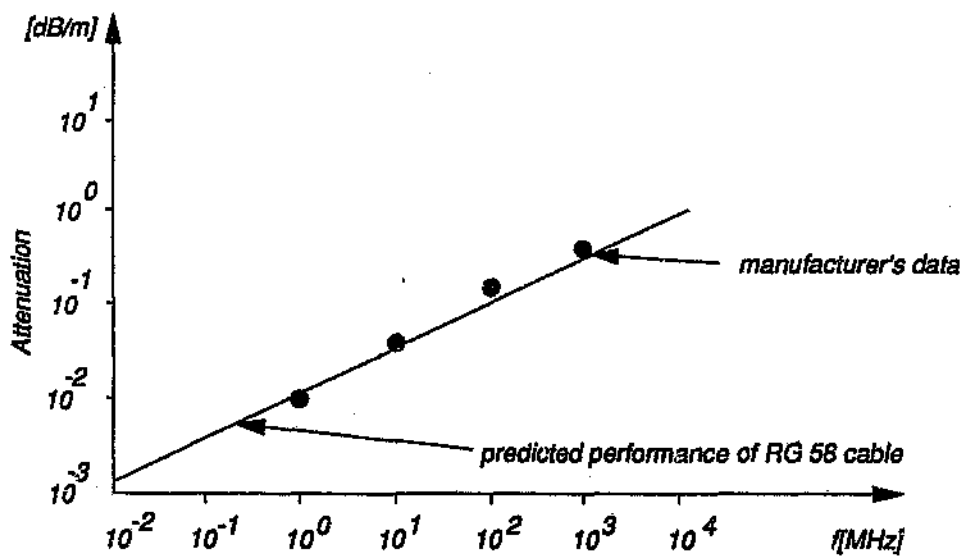


Figure 8.5 : Frequency domain performance of RG 58 C-U cable.

On this assumption, it is easy to determine the skin depth for the two materials of interest at 10MHz (approximately the repetition frequency of the pulse generator):

- In tin it is 53µm, ie less than 5,5% of the inner diameter

- In copper, the skin depth is 21μm, less than that for the tin

Furthermore, with the correction factor introduced in *appendix 6*, we conclude that the model should produce valid results. Recall that in *appendix 6* it was shown that a correction factor could easily be introduced to extend the accuracy of the model down to approximately 10Hz. At 10Hz, the ration of r_i/δ is 2. This implies a skin depth of 25% of the inner diameter! Thus we concluue that the model should be adequate. The experiment showed ~55% returned on the oscilloscope. This is shown in *figure 8.6*.

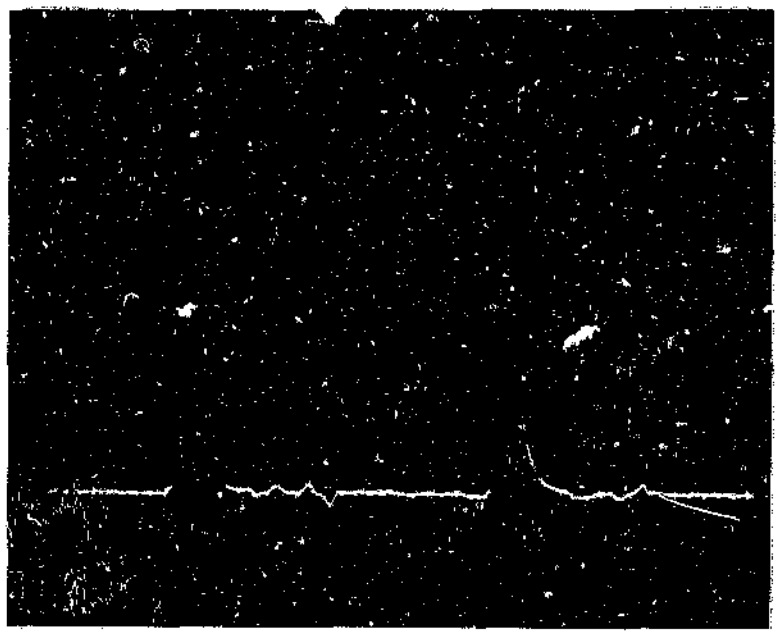


Figure 8.6 : Photographic record of pulse response of a length of RG 58 C/U cable. Scales: 10ns per large division; 400mV per large division.

This implies that ~83% of the original pulse was returned after corrections for the transfer coefficient have been made. The table below shows the predicted returns for varying coating thicknesses.

While there a numerous loss mechanisms not accounted for by this model in the case of RG 58 C/U cable, it is gratifying to see such close agreement between predicted and recorded results in all cases.

Shown in *figure 8.7* is the frequency domain performance of a hypothetical transmission line. This is included as it also shows the predicted performance based on a high frequency model (Nahman, 1962). As expected, the high frequency model and the model presented in this work converge at the higher frequencies indicating both the wide bandwidth and the accuracy of the mode here presented.

Table 8.1 : Predicted pulse response of RG 58 C/U cable for differing coating thickness.

Coating Thickness μm	Percentage (peak) of pulse returned
5	86
10	80
15	75
20	74

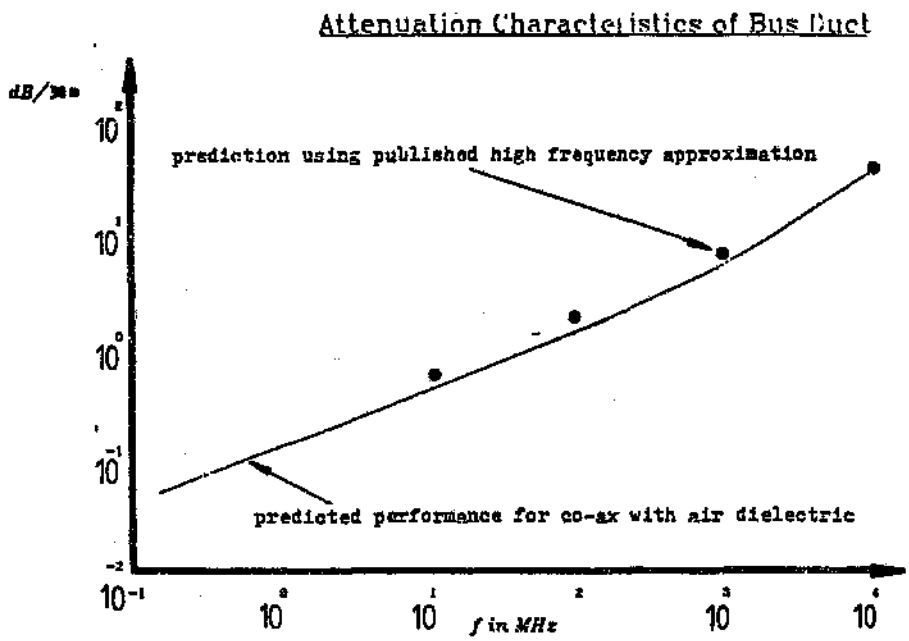


Figure 8.7 : Comparison between the predicted and published performance of a hypothetical cable (Nahman, 1962).

For completeness, the frequency domain performance of the coated system (the response of which is depicted in *figure 8.3*) is shown in *figure 8.8*.

Description : Frequency domain plot of Cu bar within Al grounded shield, $r_1 = 6,11e^{-3}$, $r_2 = 2.21e^{-2}$. Nickel Coating is applied to the Cu bar.

Inner Bus Coating Conduct : $1,4e^{7}$ S/m

Inner Bus Conductivity : 5 " S/m

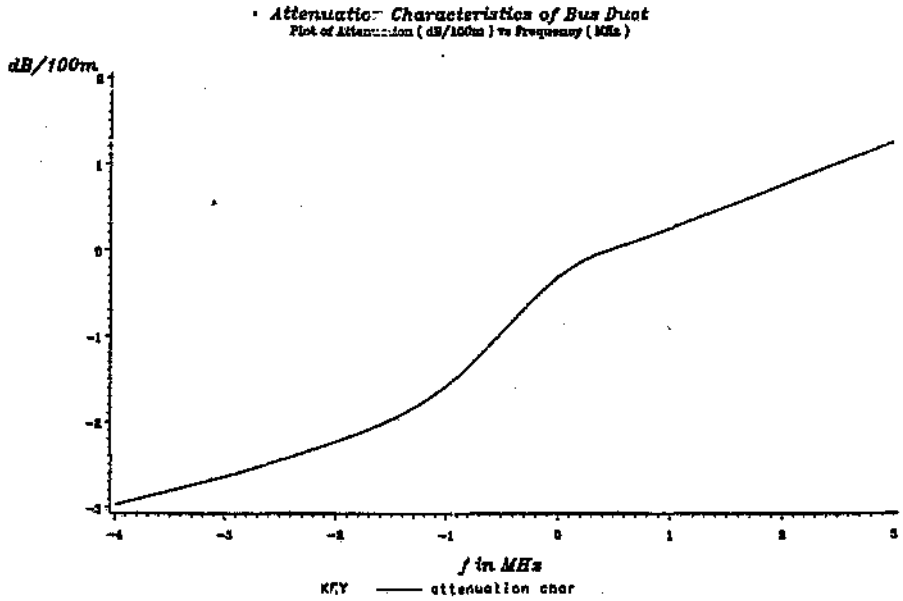
Inner Bus Coat Rel Perm : 50 (low field)

Inner Bus Rel Perm : 1

Coating Thickness : $20e^{-6}$ m

Outer Shield Conductivity : $3.54e^{7}$ S/m

Outer Shield Rel Perm : 1



Output of program SKIN

Figure 3.8 : Frequency domain characteristic of the system described in the figure.

Appendix 9 : Theoretical Analysis of SF_6 Busducts

This appendix discusses the attenuation of high frequency transients in co-axial SF_6 insulated busducts. Emphasis is placed upon the theoretical predictions of the performance of such a system. A model described in *chapter 4* is used to generate the predictions. The results show a dramatic effect, but utilise unrealistic values of μ_R. The saturation effects were ignored, and permeability values were selected to be the highest possible for the materials selected.

Figure 9.1 shows the predicted time domain response of a BG-2 size aluminium system to a representative pulse. Also in this figure is the response that would result if the same system were constructed entirely from a ferromagnetic material with a *relative permeability of 1500*. It should be noted that in all these figures, the time domain response is given for *15 m of busduct*; and the attenuation is given *per 100 m*.

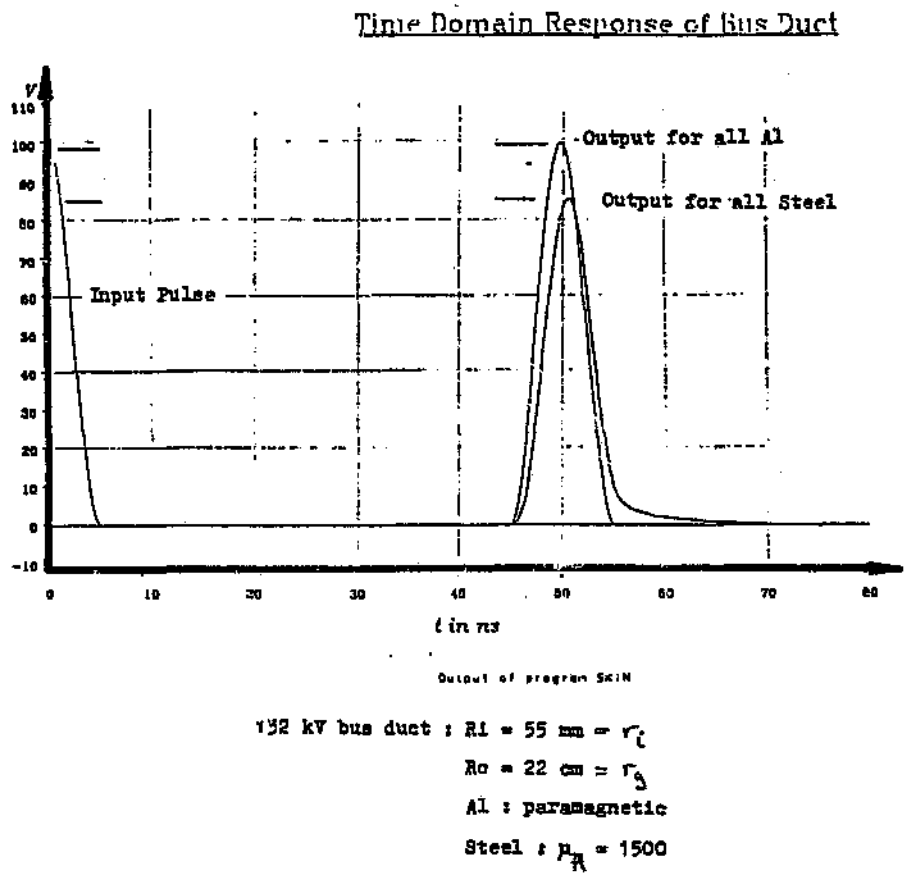


Figure 9.1 : Time domain response for a completely aluminium, and a completely steel system.

The entire manufacture of either one or both of the conductors from such a ferromagnetic material is undesirable. Not only would this increase the physical weight of the system - it would also mean that the power frequency voltages would be accordingly attenuated. This detracts from the objectives of this work.

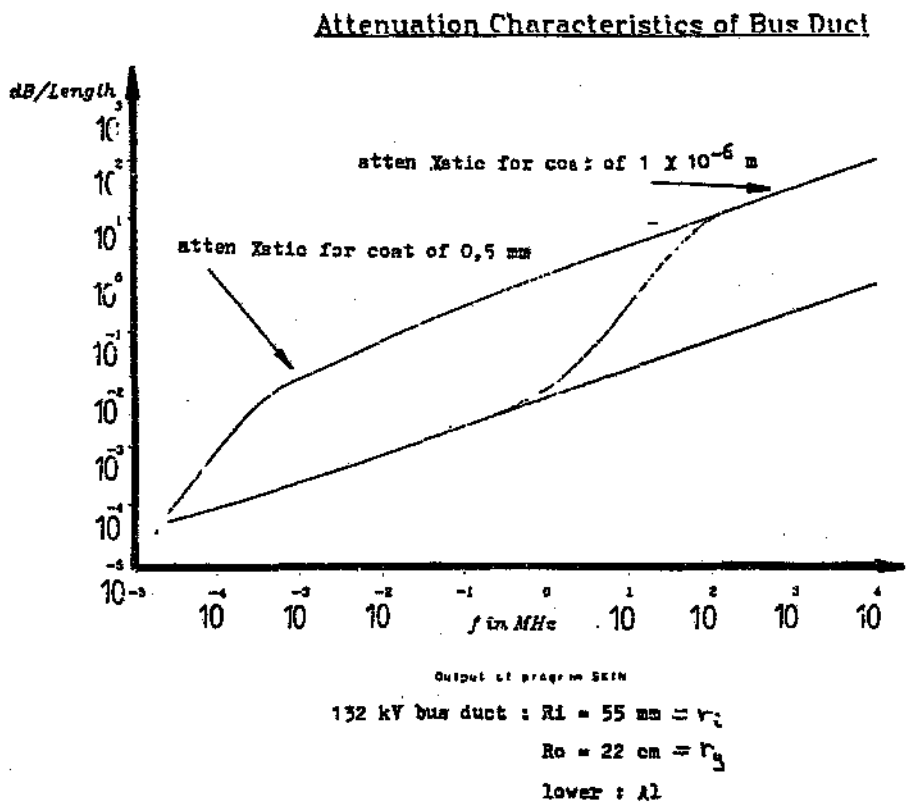


Figure 9.2 : The attenuation characteristics of a typical high voltage system, showing the effect of applying a ferromagnetic coating with a relative permeability of 1500 to the inner conductor only.

Figure 9.2 shows the attenuation characteristics of the BG-2 system. It also shows the effect introduced by coating the inner conductor with different thicknesses of a ferromagnetic material. A representative time domain response is shown in *figure 9.3*. From this figure, it may be seen that an attenuation of approximately 10% is introduced over 15m. An attenuation of 15% is introduced if a material with value of $\mu_R = 3000$ is used instead. This effect is shown in *figure 9.4*. The attenuation characteristic of such a system is shown in *figure 9.5*. Once again, the lower frequency transmission characteristics have not been affected.

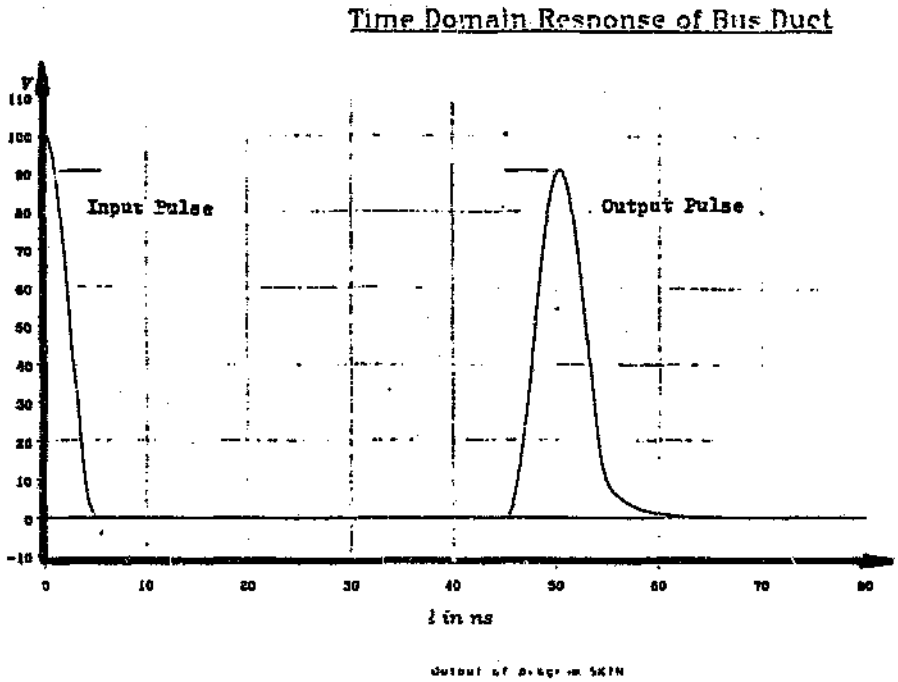


Figure 9.3 : Time domain response for a system with a 1μm coating of steel on the inner conductor.

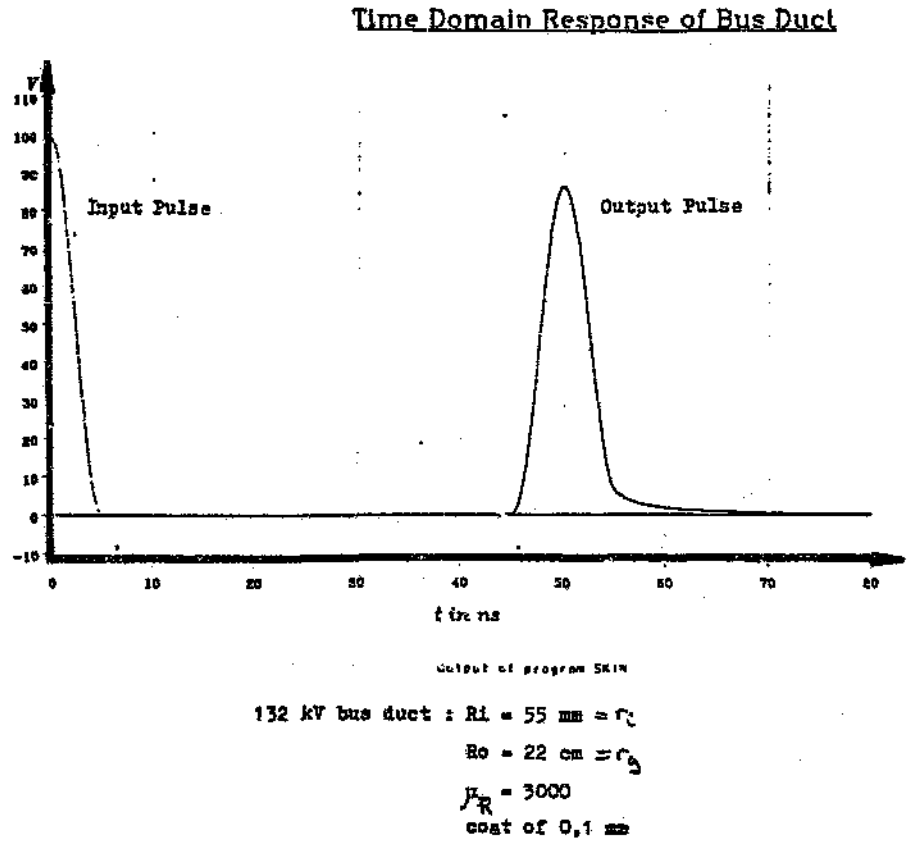


Figure 9.4 : Attenuation introduced over a 15m length by increasing the relative permeability of the coating. A value of $\mu_R = 3000$ instead of $\mu_R = 1500$. The effect of permeability is significant.

Figure 9.6 shows the effect of coating only the inner bus bar with a conductive material with a μ_R value of 30 000. The result is dramatic, but unrealistic. The objectives of a metallurgical survey should thus be to develop a material that would have as high a permeability value as possible *at the high fields* expected under transient conditions. Furthermore, the material should be conductive in order to more successfully constrain the increased attenuation characteristics to the high frequency range. This implies the importance of being able to use a thin coating of the material, and at the same time ensuring that the 50Hz fields penetrate well beyond the coating thickness, ensuring that the majority of the current flows within the aluminium substrate (busbar).

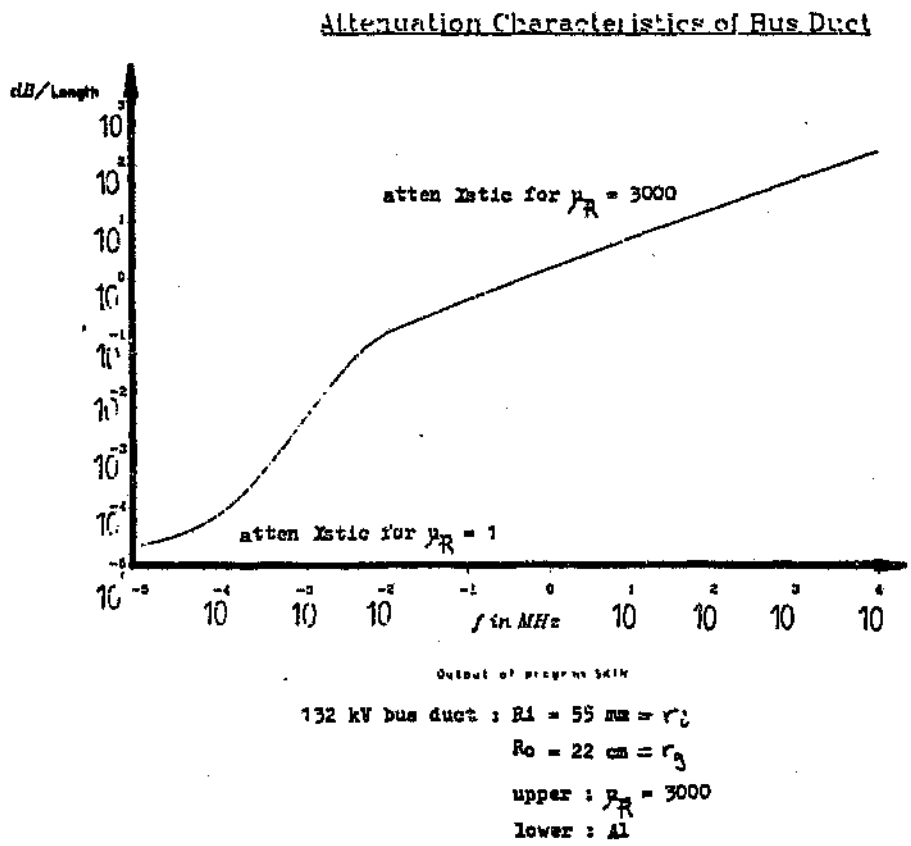


Figure 9.5 : Attenuation characteristic for a system coated with a 0,1mm coating of a material with a relative permeability of 3000.

It is important to realise from this discussion that the following observations apply to this type (ie busbar coating) of controlling technique:

- Any material with the characteristics of a dielectric that is used as a coating will introduce an increased attenuation to the 50Hz fields. Bearing in mind the fact that ideally power is transmitted exclusively within the fields generated between two perfect conductor, the dielectric is exclusively responsible for losses. We don not have prefect conductors, however, and the fields penetrate the conductor material. In a gas insulated system, the losses are almost entirely within the conductors. Thus a conductive coating can be well utilised to take full advantage of the frequency dependent penetration of the fields. The frequency domain characteristics presented in this appendix adequately demonstrate the dominance of the substrate transmission characteristic at the lower frequencies. Furthermore, it is advantageous that the transmission is at a relatively pure 50Hz, with few higher frequency harmonics present

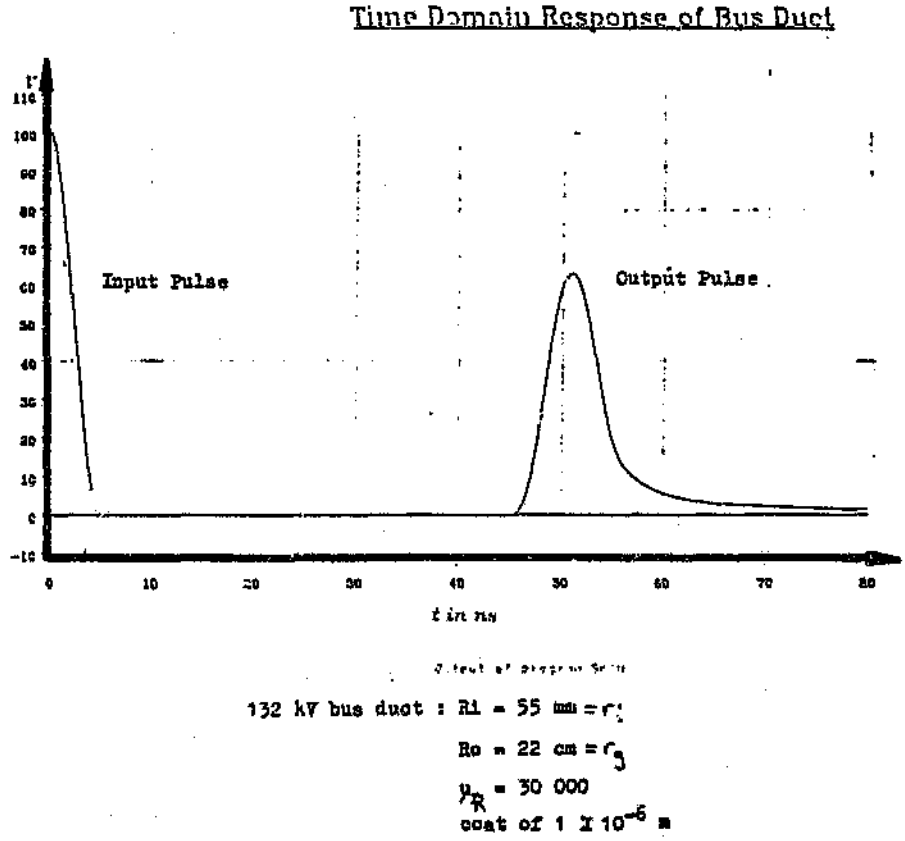


Figure 9.6 : Attenuation over 15m due to a highly permeable coating. The value of relative permeability used in this simulation is, of course, unrealistic. It does however emphasis both the effect of the parameter, and the ease with which its importance can be over-estimated. The significance of the magnetic field intensity had not been fully appreciated during the early stages of this work. Similarly, the enhancing effects of the transient skin effect within a ferromagnetic were initially not fully appreciated during the final stages of this work.

- Researchers claiming dramatic attenuation like those presented here have not accounted for the high fields present under transient conditions. Care must also be taken to fully understand attenuations introduced by ferrimagnetic materials with high values of permittivity. They fall within the gambit of materials in the point above

Appendix 10 : The Effects of Magnetic Field Intensity

This appendix is included for completeness. Its importance, however, should not be under-estimated, as it is from the careful study of predictions like these in which the various parameters are changed and the effects noted, that a true appreciation of the technique is gained. From numerous simulation studies like these it is possible to put limits to the material characteristics that are of importance to the effectiveness of the technique. There can be no doubt that experimentation alone would never have provided the information made available by the simulation method. The reasons for this are numerous, but some of the more important are:

- The magnetic field intensity during experimentation is difficult to control
- The permeability value is not a measurable quantity
- It was financially unjustifiable to fabricate the numerous variations of the test system used

It proved far more viable, for example, to conduct a simulation, and then, by examining the experimental results, determine the value of permeability that would have resulted in the observed effects. It was this philosophy that lead to the appreciation of saturation effects within the materials. It similarly lead to the appreciation of the advantageous effects of transient field penetration within a ferromagnetic material.

The predictions are shown for various systems with the dimensions of the BBC BG-2 size busduct. On each file is included a description of the physical system under consideration, thus each file has printed on it the permeability and conductivity of the coatings used. For each system under consideration, the frequency domain characteristic of the system is shown, followed by the time domain pulse response. Particularly the effect of permeability is shown. The effect of coating thickness is also evident, especially in the frequency domain where it is very graphically portrayed.

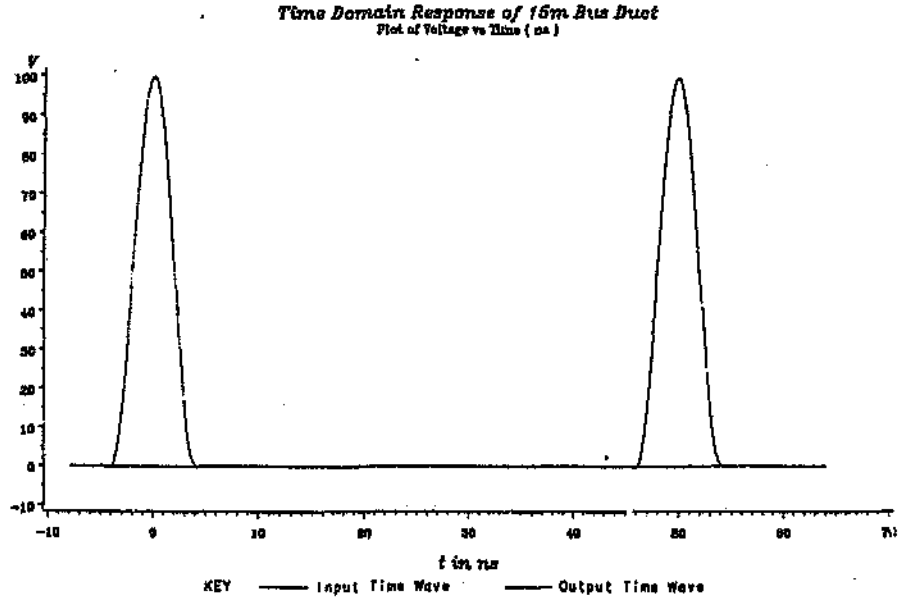
Description : Time domain plot of typical 132 KV Bus Duct, with r_1 = $55e^{-3}$, r_g = $20e^{-2}$. Bus Bar and Grounded Shield uncoated Aluminium. Plot shows actual response within the length of Bus Duct.

Inner Bus Conductivity : $3.54e^{7}$ S/m

Inner Bus Rel Perm : 1

Outer Shield Conductivity : $3.54e^{7}$ S/m

Outer Shield Rel Perm : 1



Output of program SKIN

Figure 10.1 : Time domain response. Uncoated case.

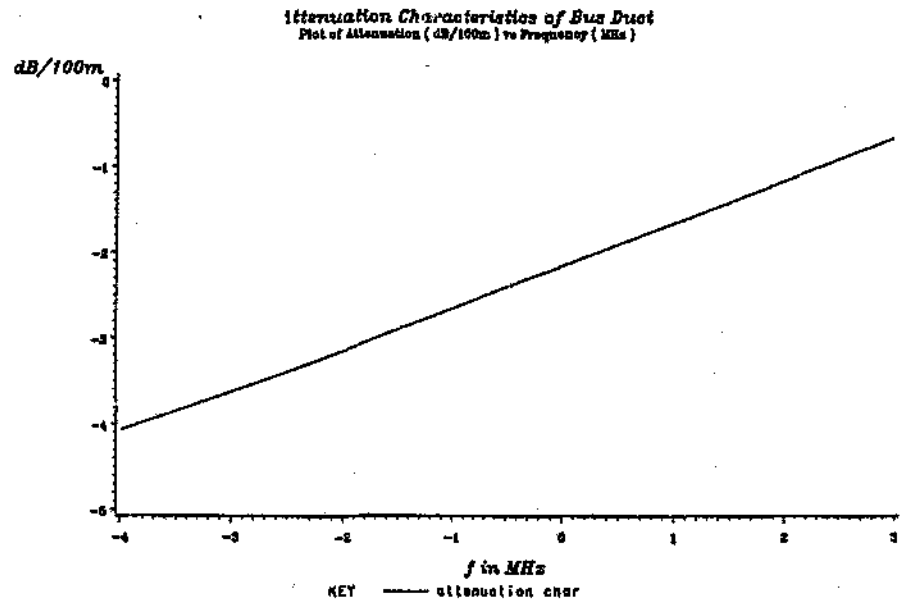
Description : Frequency domain plot of typical 132 KV Bus Duct, with r_i = $55e^{-3}$, r_g = $20e^{-2}$. Bus Bar and Grounded Shield uncoated Aluminium.

Inner Bus Conductivity : $3.54e^{7}$ S/m

Inner Bus Rel Perm : 1

Outer Shield Conductivity : $3.54e^{7}$ S/m

Outer Shield Rel Perm : 1



Output of program SKIN

Figure 10.2 : Frequency domain performance. Uncoated case.

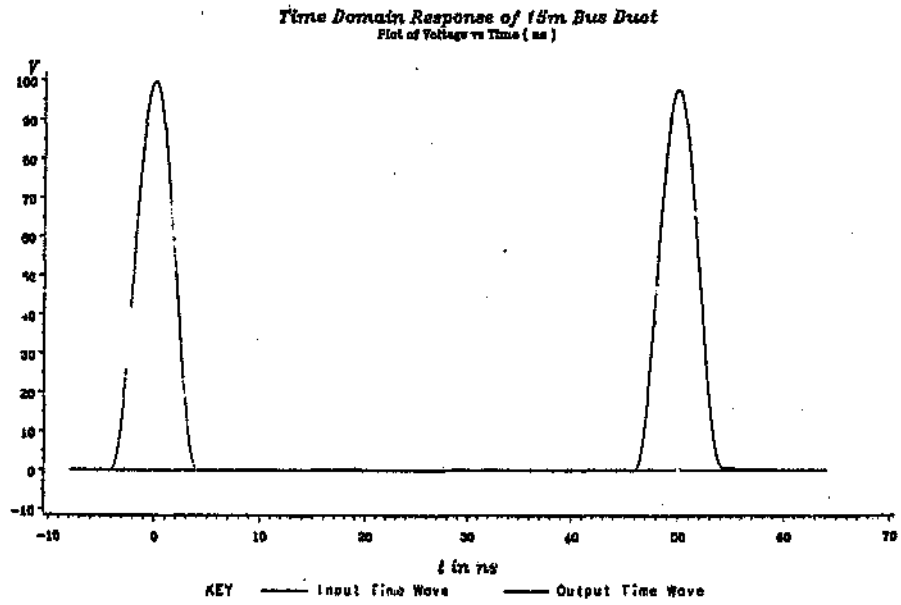
Description : Time domain plot of typical 132 KV Bus Duct, with r_1 = $55e^{-3}$, r_2 = $20e^{-2}$. Bus Bar and Grounded Shield uncoated Mild Steel. Plot shows actual response within the length of Bus Duct.

Inner Bus Conductivity : $1.0e^7$ S/m

Inner Bus Rel Perm : 120 (low field)

Outer Shield Conductivity : $1.0e^7$ S/m

Outer Shield Rel Perm : 120 (low field)



Output of program SKIN

Figure 10.3 : Time domain response. Uncoated case.

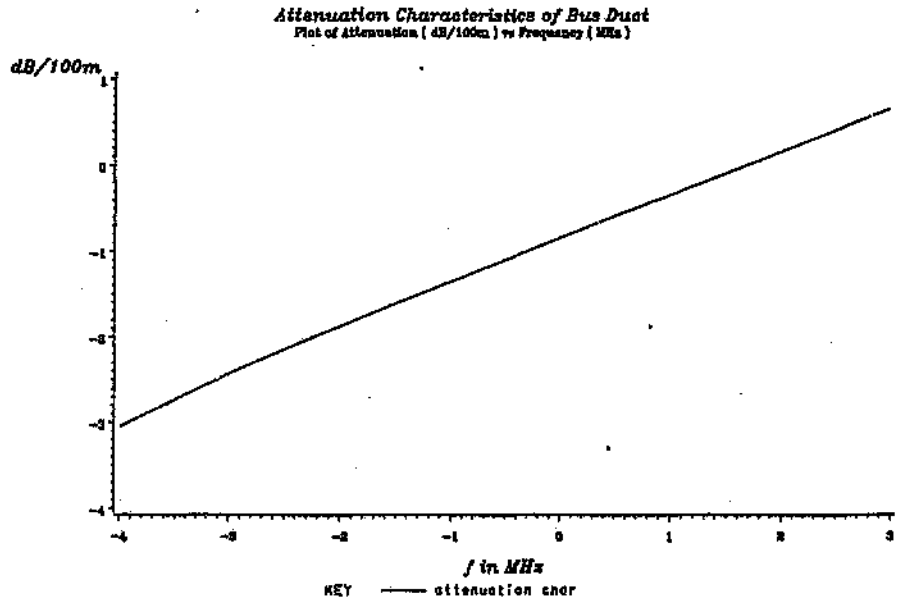
Description : Frequency domain plot of typical 132 kV Bus Duct, with r_1 = $55e^{-3}$, r_g = $20e^{-2}$. Bus Bar and Grounded Shield uncoated Mild Steel.

Inner Bus Conductivity : $1.0e^{7}$ S/m

Inner Bus Rel Perm : 120 (low field)

Outer Shield Conductivity : $1.0e^{7}$ S/m

Outer Shield Rel Perm : 120 (low field)



Output of program SKIN

Figure 10.4 : Frequency domain performance. Uncoated case.

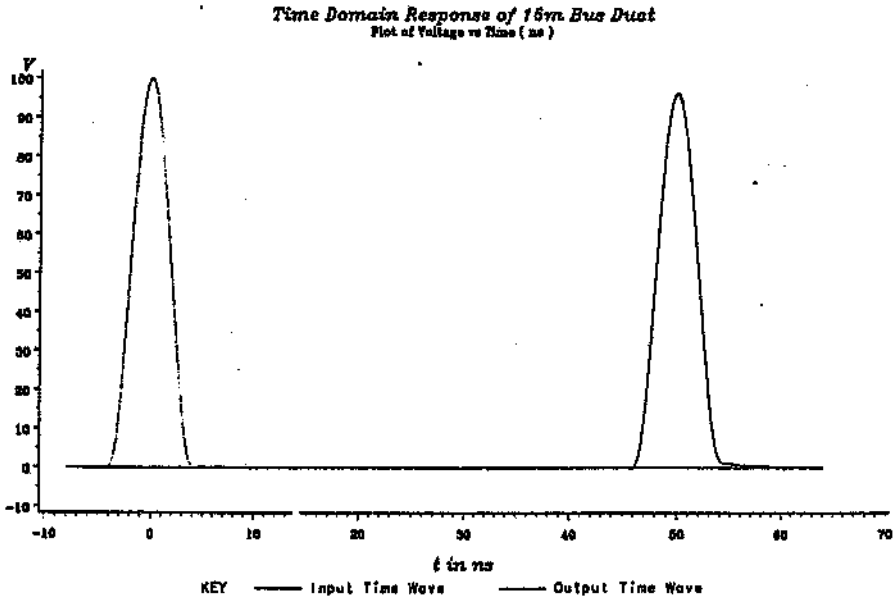
Description : Time domain plot of typical 132 kV Bus Duct, with r_i = $55e^{-3}$, r_g = $20e^{-2}$. Bus Bar and Grounded Shield uncoated Mild Steel. Plot shows actual response within the length of Bus Duct.

Inner Bus Conductivity : $1.0e^{7}$ S/m

Inner Bus Rel Perm : 400 (high field)

Outer Shield Conductivity : $1.0e^{7}$ S/m

Outer Shield Rel Perm : 400 (high field)



Output of program SKIN

Figure 10.5 : Time domain response. Uncoated case.

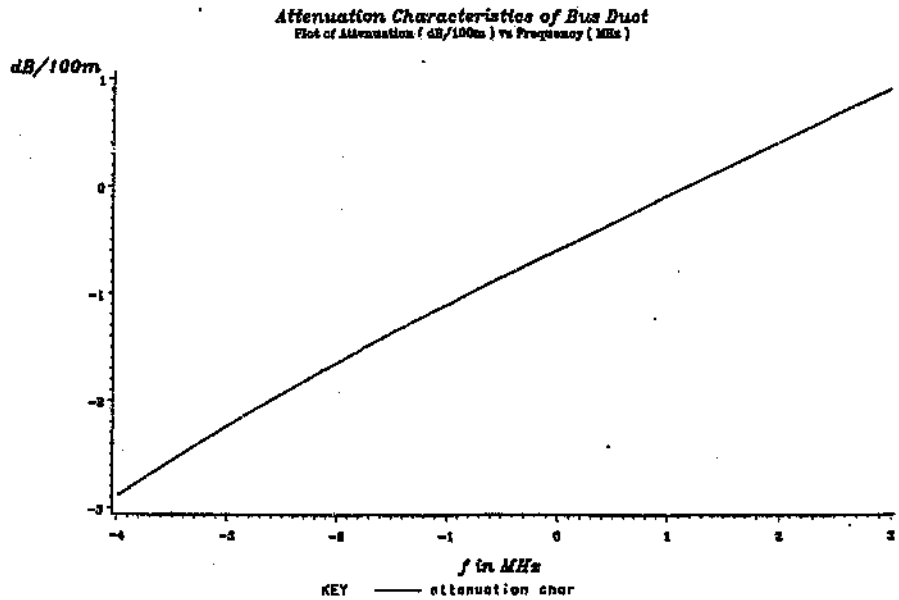
Description : Frequency domain plot of typical 132 kV Bus Duct, with r_i = $55e^{-3}$, r_g = $20e^{-2}$. Bus Bar and Grounded Shield uncoated Mild Steel.

Inner Bus Conductivity : $1.0e^{7}$ S/m

Inner Bus Rel Perm : 400 (high field)

Outer Shield Conductivity : $1.0e^{7}$ S/m

Outer Shield Rel Perm : 400 (high field)



Output of program SKIN

Figure 10.6 : Frequency domain performance. Uncoated case.

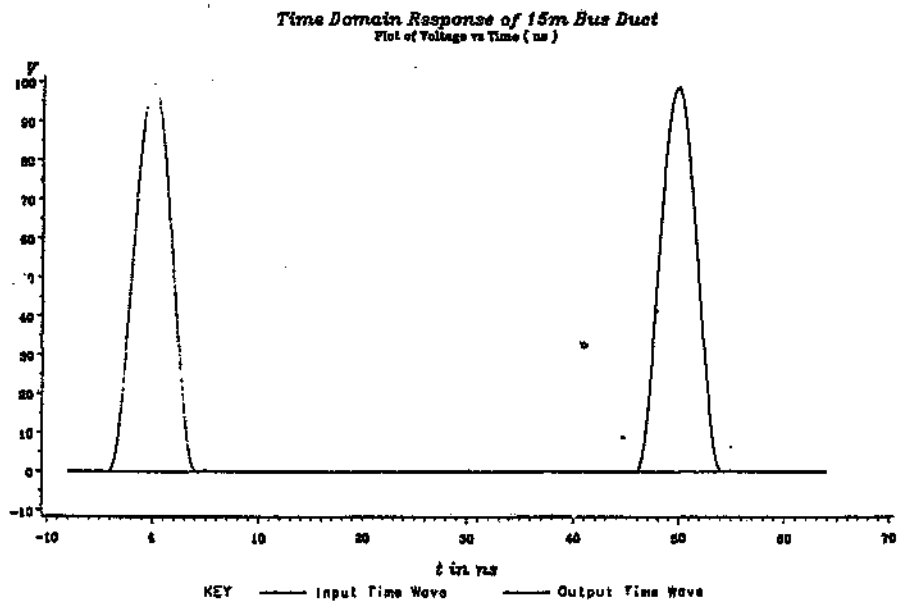
Description : Time domain plot of typical 132 kV Bus Duct, with $r_i = 55e^{-3}$, $r_g = 20e^{-2}$. Bus Bar of Aluminium within a Grounded Shield of Mild Steel. Plot shows actual response within the length of Bus Duct.

Inner Bus Conductivity : $3.64e^{7}$ S/m

Inner Bus Rel Perm : 1

Outer Shield Conductivity : $1.0e^{7}$ S/m

Outer Shield Rel Perm : 400 (high field)



Output of program SKIN

Figure 10.7 : Time domain response. Uncoated case.

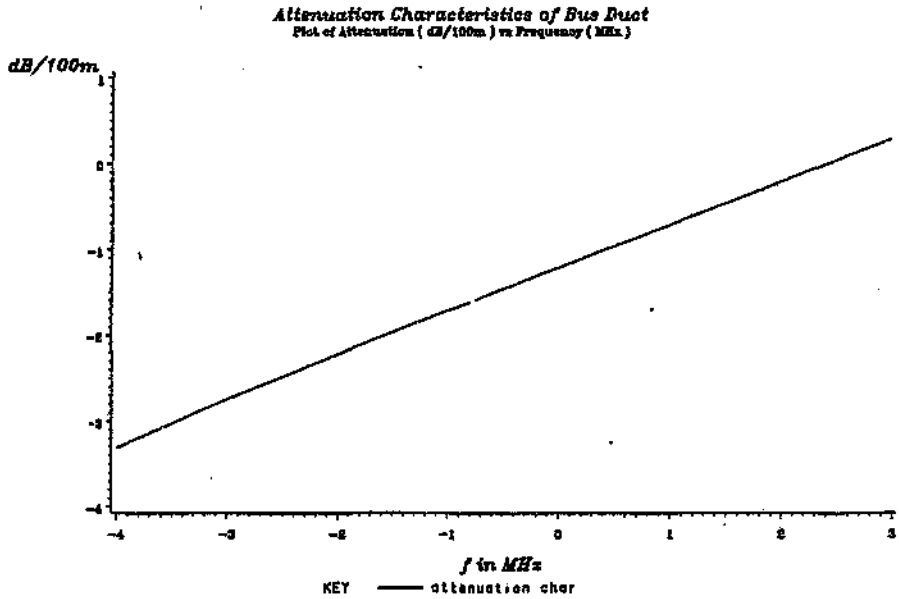
Description : Frequency domain plot of typical 132 KV Bus Duct, with r_1 = $55e^{-3}$, r_2 = $20e^{-2}$. Bus Bar of Aluminium within a Grounded Shield of Mild Steel.

Inner Bus Conductivity : $3.54e^{7}$ S/m

Inner Bus Rel Perm : 1

Outer Shield Conductivity : $1.0e^{7}$ S/m

Outer Shield Rel Perm : 400 (high field)



Output of program SKIN

Figure 10.8 : Frequency domain performance. Uncoated case.

Description : Time domain Plot of typical 132 kV Bus Duct, with $r_i = 55e^{-3}$, $r_s = 20e^{-2}$. Bus Bar of Aluminium with a Mild Steel coating, within a Grounded Shield of Aluminium. Plot shows actual response within the length of Bus Duct.

Inner Bus Coating Conductivity : $1.0e^{7}$ S/m

Inner Bus Conductivity : $3.54e^{7}$ S/m

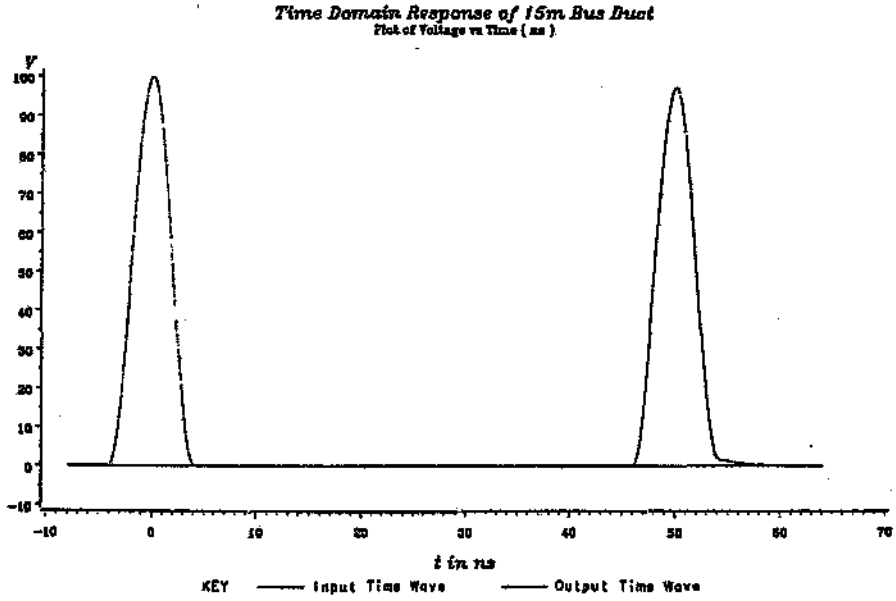
Inner Bus Coat Rel Perm : 400 (high field)

Inner Bus Rel Perm : 1

Coating Thickness : $1e^{-6}$ m

Outer Shield Conductivity : $3.54e^{7}$ S/m

Outer Shield Rel Perm : 1



Output of program SKIN

Figure 10.9 : Time domain response. Coated case.

Description : Frequency domain plot of typical 132 kV Bus Duct, with r_i = $55e^{-3}$, r_g = $20e^{-2}$. Bus Bar of Aluminium with a Mild Steel coating, within a Grounded Shield of Aluminium.

Inner Bus Coating Conductivity : $1.0e^{7}$ S/m

Inner Bus Conductivity : $3.54e^{7}$ S/m

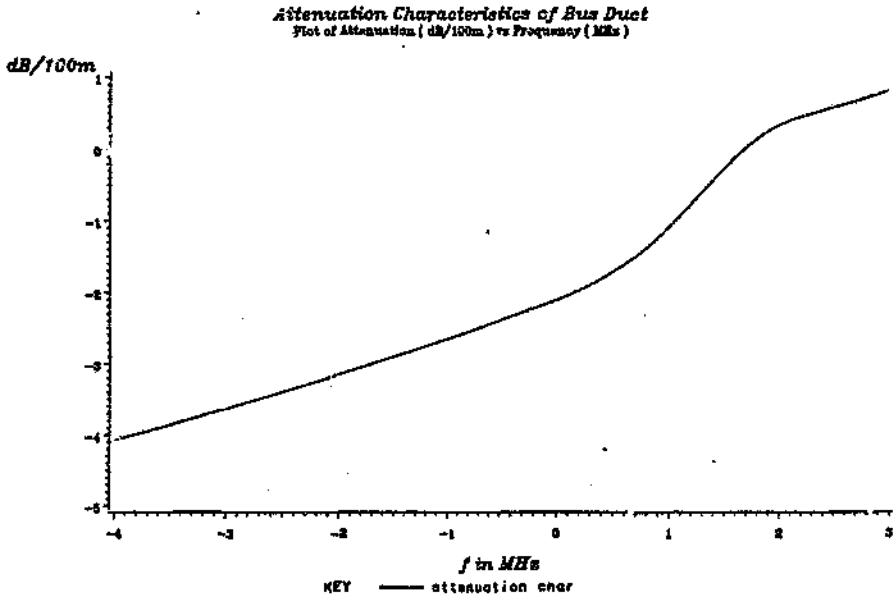
Inner Bus Coat Rel Perm : 400 (high field)

Inner Bus Rel Perm : 1

Coating Thickness : $1e^{-6}$ m

Outer Shield Conductivity : $.54e^{7}$ S/m

Outer Shield Rel Perm : 1



Output of program SKIN

Figure 10.10 : Frequency domain performance. Coated ca

Description : Time domain plot of typical 132 kV Bus Duct, with r_i = $55e^{-3}$, r_s = $20e^{-2}$. Bus Bar of Aluminium with a Mild Steel coating, within a Grounded Shield of Aluminium. Plot shows actual response within the length of Bus Duct.

Inner Bus Coating Conductivity : $1.0e^{7}$ S/m

Inner Bus Conductivity : $3.54e^{7}$ S/m

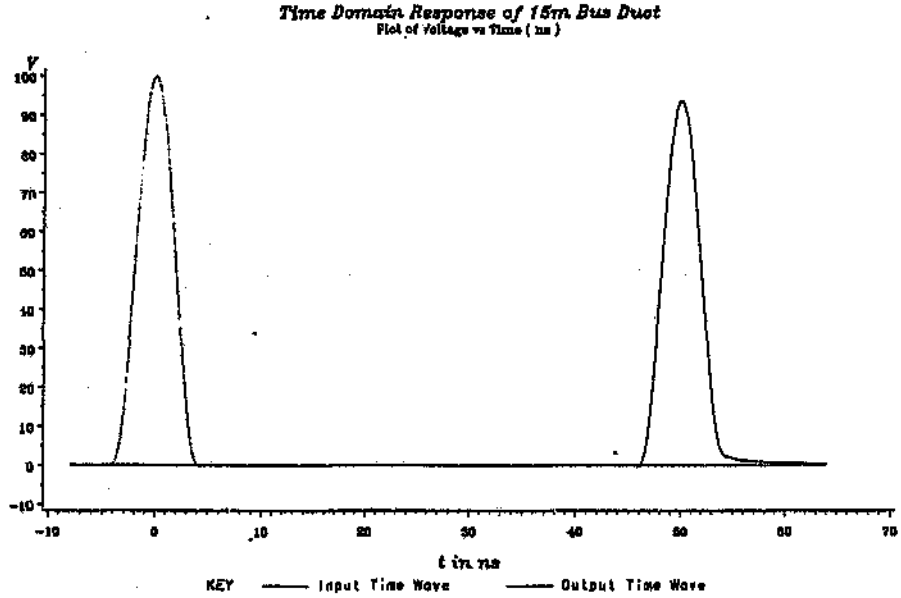
Inner Bus Coat Rel Perm : 2000 (maximum value)

Inner Bus Rel Perm : 1

Coating Thickness : $4.5e^{-6}$ m

Outer Shield Conductivity : $3.54e^{7}$ S/m

Outer Shield Rel Perm : 1



Output of program SKIN

Figure 10.11 : Time domain response. Coated case.

Description : Frequency domain plot of typical 132 kV Bus Duct, with r_i = $55e^{-3}$, r_g = $20e^{-2}$. Bus Bar of Aluminium with a Mild Steel coating, within a Grounded Shield of Aluminium.

Inner Bus Coating Conductivity : $1.0e^{7}$ S/m

Inner Bus Conductivity : $3.54e^{7}$ S/m

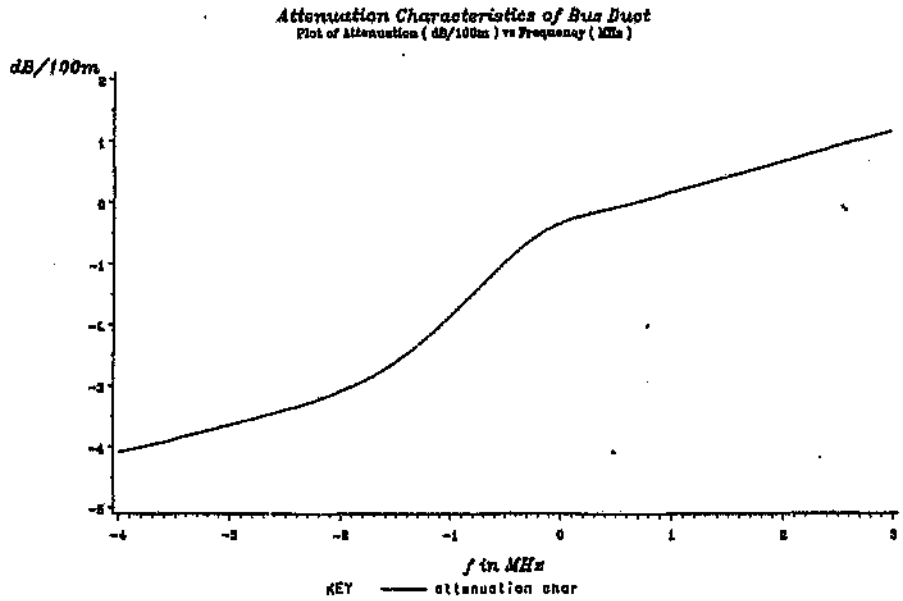
Inner Bus Coat Rel Perm : 2000 (maximum value)

Inner Bus Rel Perm : 1

Coating Thickness : $4.5e^{-6}$ m

Outer Shield Conductivity : $3.54e^{7}$ S/m

Outer Shield Rel Perm : 1



Output of program SKIN

Figure 10.12 : Frequency domain performance. Coated case.

Description : Time domain plot of typical 132 kV Bus Duct, with r_1 = $55e^{-3}$, r_2 = $20e^{-2}$, Bus Bar of Aluminium with a Vanadium Permendur coating. within a Grounded Shield of Aluminium. Plot shows actual response within the length of Bus Duct.

Inner Bus Coating Conductivity : $3.8e^{6}$ S/m

Inner Bus Conductivity : $3.54e^{7}$ S/m

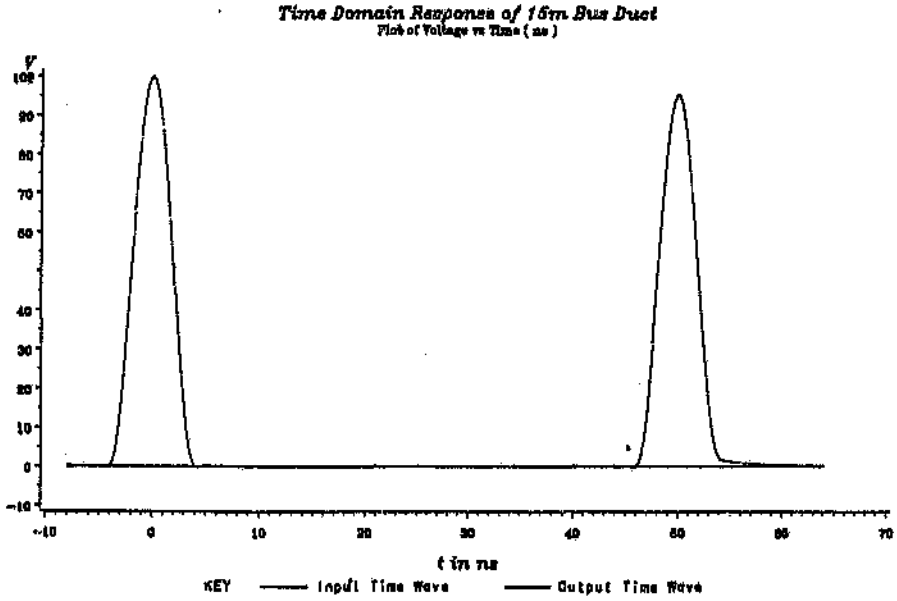
Inner Bus Coat Rel Perm : 381 (high field)

Inner Bus Rel Perm : 1

Coating Thickness : $16.5e^{-6}$ m

Outer Shield Conductivity : $3.54e^{7}$ S/m

Outer Shield Rel Perm : 1



Output of program SKIN

Figure 10.13 : Time domain response. Coated case.

Description : Frequency domain plot of typical 132 KV Bus Duct, with r_i = $55e^{-3}$, r_g = $20e^{-2}$, Pus Bar of Aluminium with a Vanadium Permendur coating, within a Grounded Shield of Aluminium.

Inner Bus Coating Conductivity : $3,8e^{6}$ S/m

Inner Bus Conductivity : $3,54e^{7}$ S/m

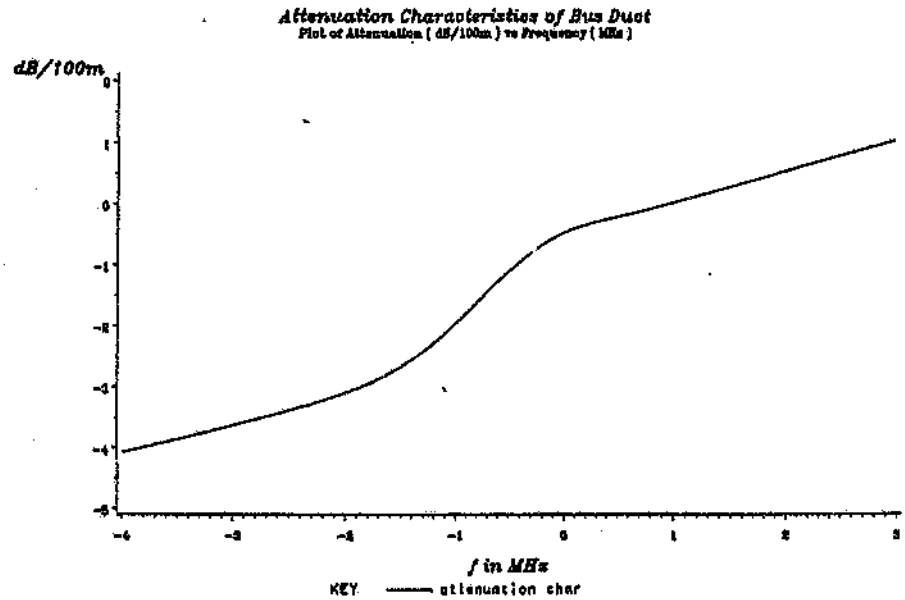
Inner Bus Coat Rel Perm : 361 (high field)

Inner Bus Rel Perm : 1

Coating Thickness : $16,5e^{-6}$ m

Outer Shield Conductivity : $3,54e^{7}$ S/m

Outer Shield Rel Perm : 1



Output of program SKIN

Figure 10.14 : Frequency domain performance. Coated case.

Description : Time domain plot of typical 132 kV Bus Duct, with r_1 = $55e^{-3}$, r_2 = $20e^{-2}$. Bus Bar of Aluminium with an Alperm coating, within a Grounded Shield of Aluminium. Plot shows actual response within the length of Bus Duct.

Inner Bus Coating Conductivity : $7.0e^{5}$ S/m

Inner Bus Conductivity : $3.54e^{7}$ S/m

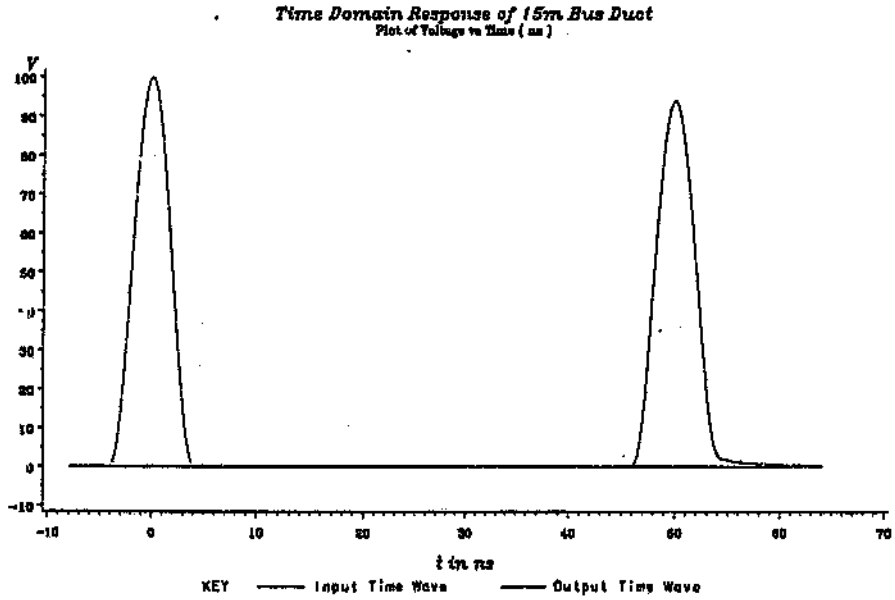
Inner Bus Coat Rel Perm : 127 (high field)

Inner Bus Rel Perm : 1

Coating Thickness : $67e^{-6}$ m

Outer Shield Conductivity : $3.54e^{7}$ S/m

Outer Shield Rel Perm : 1



Output of program SKIN

Figure 10.15 : Time domain response. Coated case.

Description : Frequency domain plot of typical 132 kV Bus Duct, with r_1 = $55e^{-3}$, r_2 = $20e^{-2}$. Bus Bar of Aluminium with an Alperm coating, within a Grounded Shield of Aluminium.

Inner Bus Coating Conductivity : $7.0e^{5}$ S/m

Inner Bus Conductivity : $3.54e^{7}$ S/m

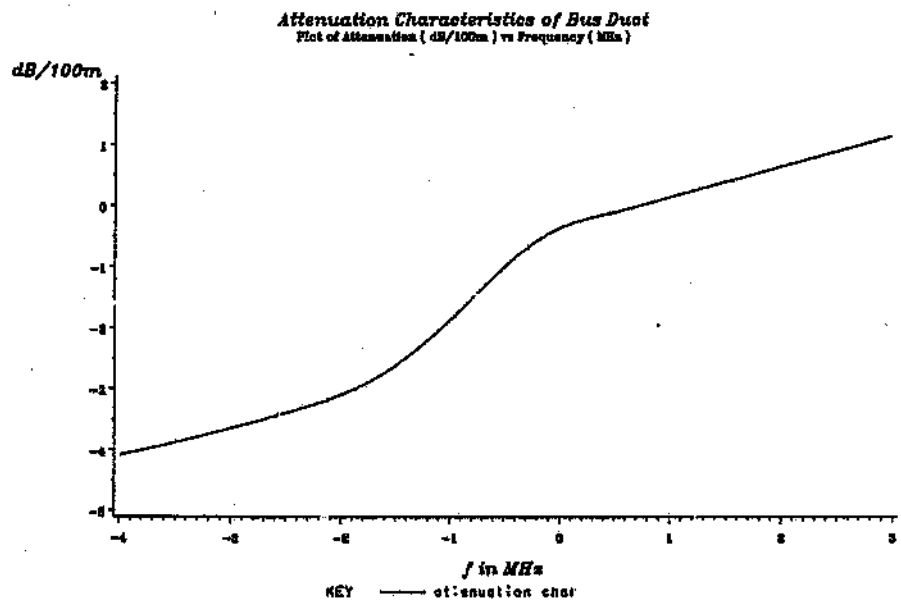
Inner Bus Coat Rel Perm : 127 (high field)

Inner Bus Rel Perm : 1

Coating Thickness : $67e^{-6}$ m

Outer Shield Conductivity : $3.54e^{7}$ S/m

Outer Shield Rel Perm : 1



Output of program SKIN

Figure 10.16 : Frequency domain performance. Coated case.

Appendix 11 : Physical Attributes of Four Materials Considered for Use in this Application

This appendix documents the physical characteristics of four sample materials considered for use in this application. The percentage composition was obtained from the manufacturer, or detailed by the metallurgist for the manufacturer. The permeabilities and conductivities were determined as detailed in *appendix 12*.

Sample 1

Percentage composition:

C 0,070; *Ni* 59,35; *Mn* 0,71; *Si* 0,15;

Cu 0,06; *S* 0,005; *P* 0,007; *Fe* *Balance*

Conductivity:

$2,697 \times 10^6$ [S/m]

Permeability:

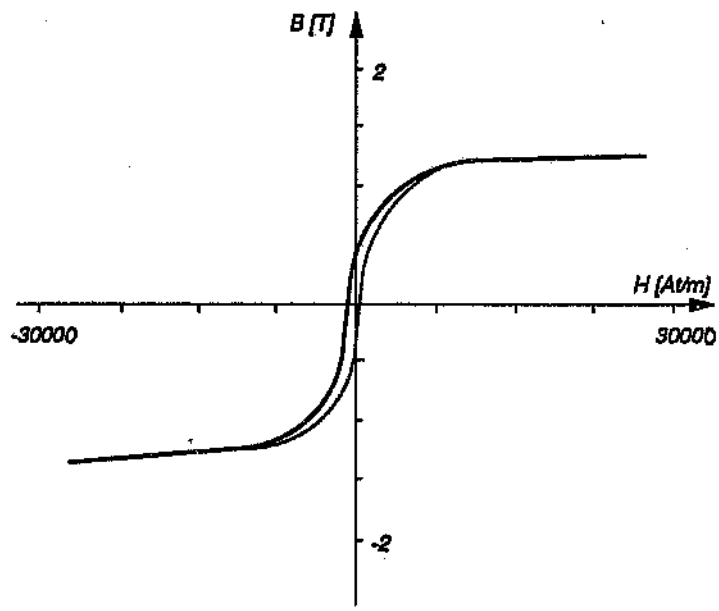


Figure 11.1 : B-H curve for *sample 1*.

Sample 2

Percentage composition:

C 0,102; *Cr* 29,95; *Ni* 9,73; *Mn* 1,95; *Si* 0,40;

P 0,022; *S* 0,0011; *Mo* 0,09; *Fe* *Balance*

Conductivity:

$1,145 \times 10^6$ [S/m]

Permeability:

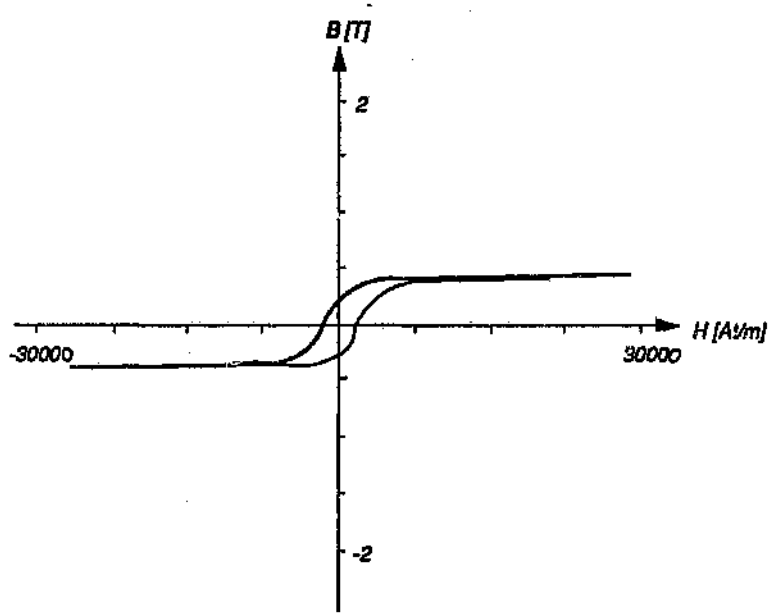


Figure 11.2 : B-H curve for *sample* 2.

Sample 3

Percentage composition:

C 0,03; *N* 0,03; *Ni* 1,5; *Mn* 1,5; *Si* 1,0; *P* 0,03;

S 0,03; *Cr* (11,0 – 12,0); *Ti* $4 \cdot (C+N)$; *Fe* *Balance*

Conductivity:

$1{,}759 \times 10^6$ [S/m]

Permeability:

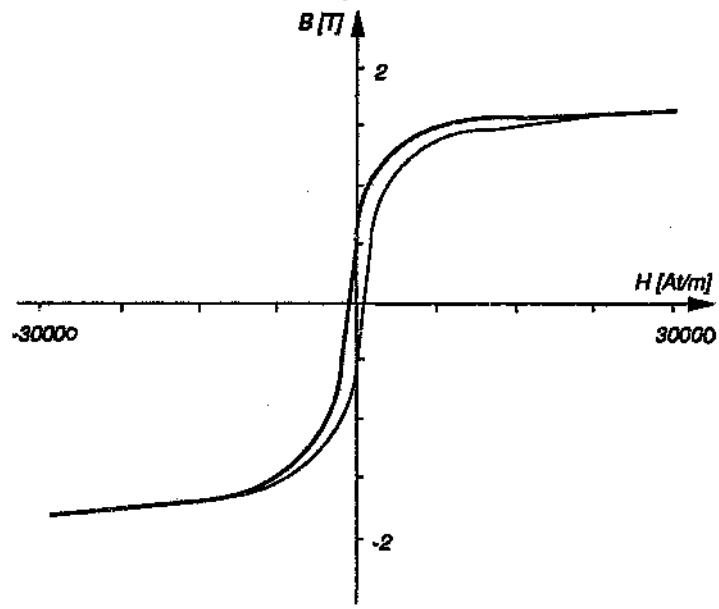


Figure 11.3 : B-H curve for *sample 3*.

Sample 4

Percentage composition:

Cr 5; *Co* 40; *Fe* 55

Conductivity:

$2,108 \times 10^{6}$[S/m]

Permeability:

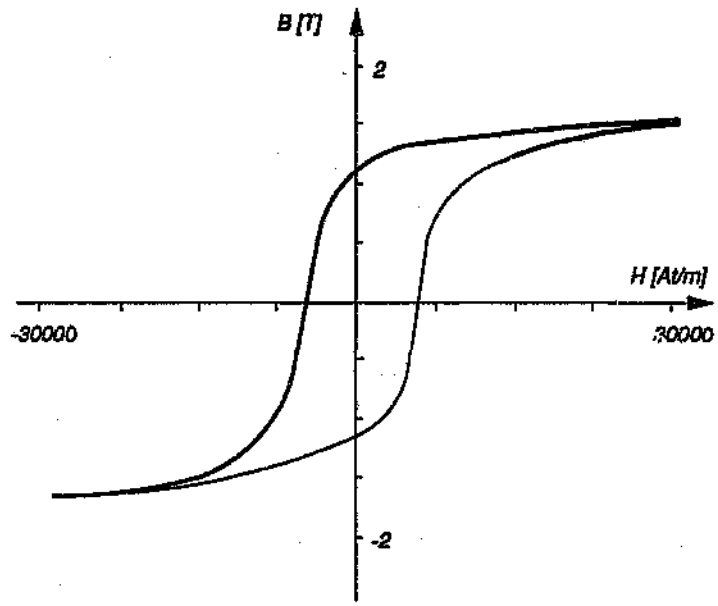


Figure 11.4 : B-H curve for *sample 4*.

Appendix 12 : Methods of Determining Material Characteristics

This appendix briefly outlines the techniques used to establish the conductivity and permeability of the four samples considered from a theoretical perspective for use in this application. It must be noted that the techniques were simple and established. The conductivity was determined by running a known smooth DC current through the sample, while the permeability was determined with the aid of a Koepsel permeameter.

For both these measurements, the same sample of material was used, the physical dimensions of the samples being determined by the capabilities of the permeameter. Samples 1 and 2 were in the form of 5mm long rods of 300mm length, while samples 3 and 4 were in the form of 5mm by 5mm square cross-section rods of 300mm length, as depicted in *figure 12.1*

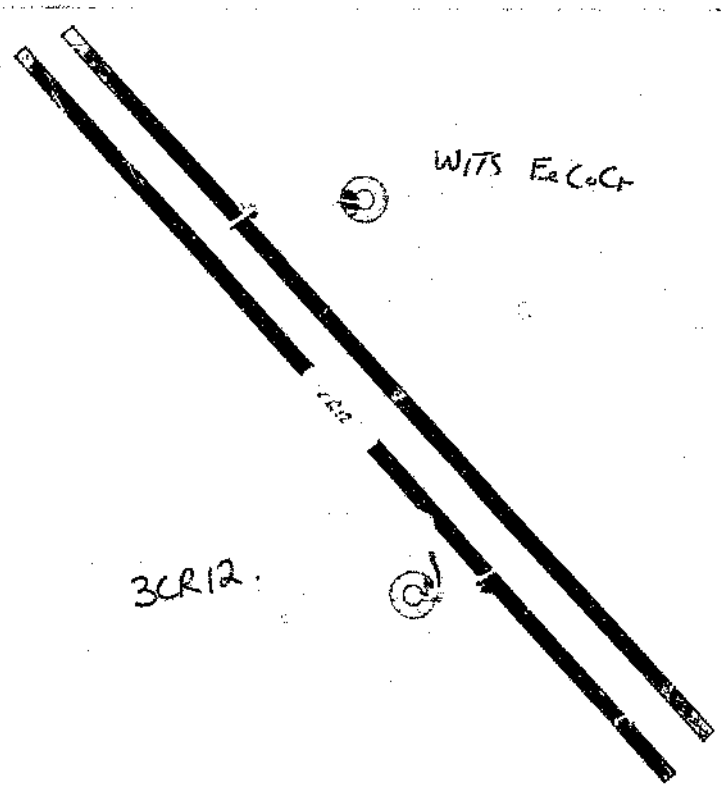


Figure 12.1 : During preparation of the samples, care was taken not to heat the metal unnecessarily. Three samples of each material were prepared, and in the case of 3CR12 (sample 3) tests were conducted both with and across the rolling direction. Little difference was detected.

In the determination of the conductivity, 10A was permitted to flow through the samples. Measurements were made at 25°C. Measurements were made within 30 seconds of the current application. Prior to current application, the current was run through an identical sample, but no measurement was made on that sample. The current was adjusted on the identical sample in order to minimise changes in the circuit while the sample under test was in circuit. While current was injected at the ends of the sample, the voltage was made over a 250 and a 150mm length. This was so as to ensure that the current was evenly distributed over the entire cross-section of the sample over the length over which the measurement was made.

The Koepsel apparatus is intended for the commercial determination of the normal hysteresis curve of ferromagnetic materials with the dimensions stipulated above. The tests are easily conducted and the results are accurate. It must be noted that the instrument was first set so that the earth's magnetic field had no effect upon its operation. Tabulated results, as well as instrumentation details, are available on request.

Appendix 13 : Magnetic Field Intensity within a Typical Busduct

If we were to consider a typical 132kV busduct, the per phase voltage is:

$$76,21\text{kV}$$

$$= 1,0\text{pu}$$

Hence an initial surge rising to a peak value of 0,7pu (say) attains a voltage level of:

$$53,9\text{kV}$$

With a 75Ω (realistic) characteristic impedance, this implies an initial surge current of:

$$718,6\text{A}$$

Thus, with a busbar diameter of 110mm, the busbar surface field intensity is:

$$\vec{H} = 2080 \quad [\text{A/m}]$$

$$\therefore \quad 4 \times \vec{H} = 8320 \quad [\text{A/m}]$$

The selection of four times the expected magnetic field intensity is arbitrary, but nevertheless allows us to examine the operation of the technique under excessively high field intensities.

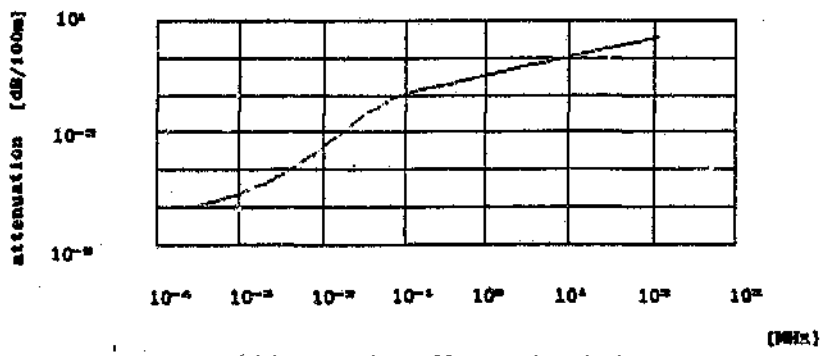
Appendix 14 : Theoretical Examination of the Effectiveness of the Four Samples

This appendix does not pretend to be an extremely detailed examination of the performance of the four samples. Rather it serves to allow comparison of the performance, and aid in the understanding of the combined effects of the conductivities and permeabilities of the materials. It also shows the dramatic difference between soft and hard magnetic materials. It also emphasises the importance of field intensity on the performance of the material, and shows a curious effect in sample 4, where the high field attenuation is higher due to the form of the B-H curve. Unfortunately this effect is countered by the generally poor performance of this sample. A similar argument may be applied to sample 2, which is a harder material - the difference between high and low field performance is smaller than for the other samples, but the performance is in general poorer. The surge response is included for completeness, but is only really of user in samples 3 and 4 where the effect is clear and insignificant respectively.

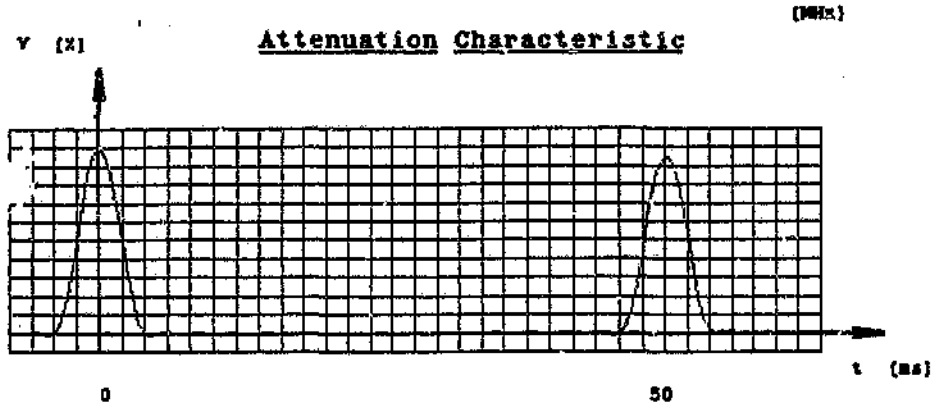
Particular note should be taken of the frequency domain performance, and the pulse attenuation. While the graphic display is rather poor, the pulse attenuation was printed out from within the simulation for each test.

Performance Records for the Four Samples

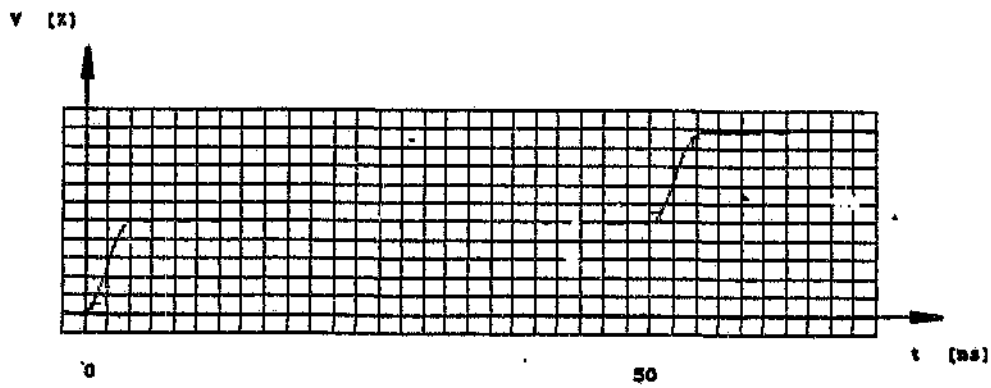
Sample 1 - H = 2080 [A/m]



Attenuation Characteristic



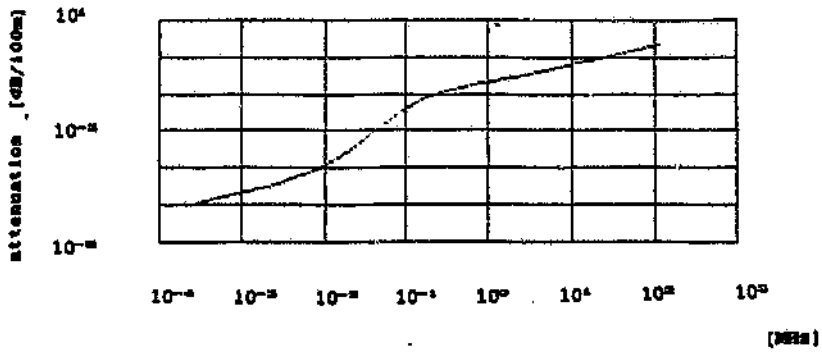
Pulse Response - 4,9 % Attenuation



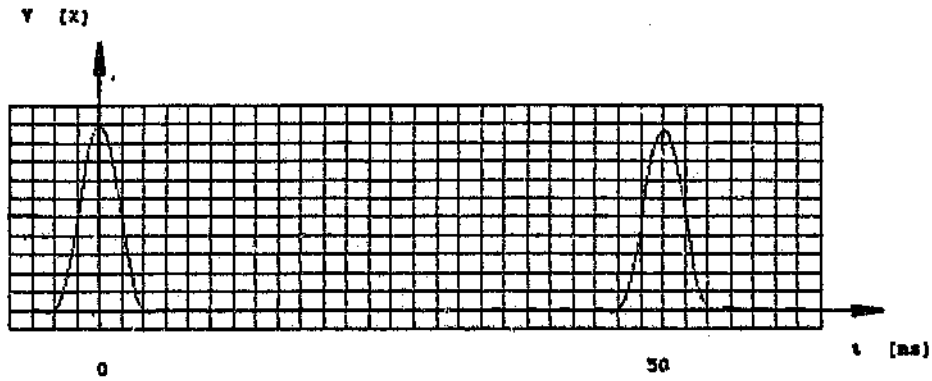
Surge Response

Figure 14.1

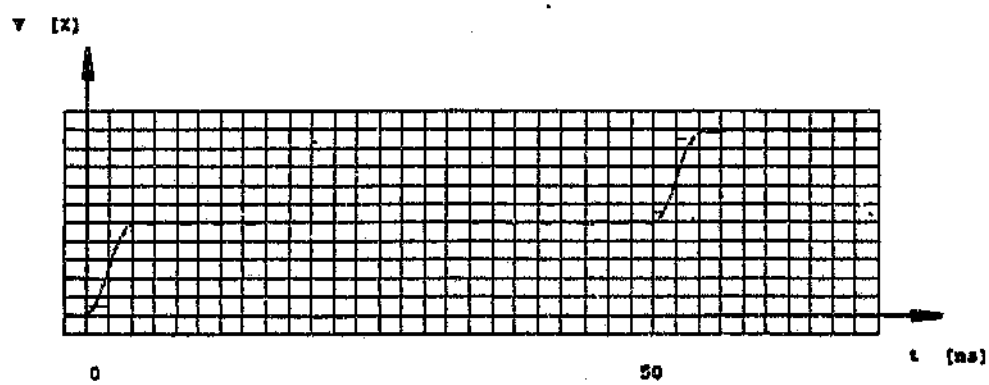
Sample i = H = 6320 [A/m]



Attenuation Characteristic



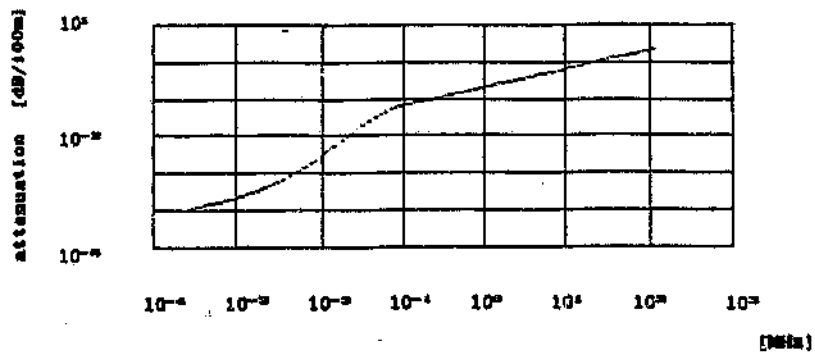
Pulse Response - 2,93 % Attenuation



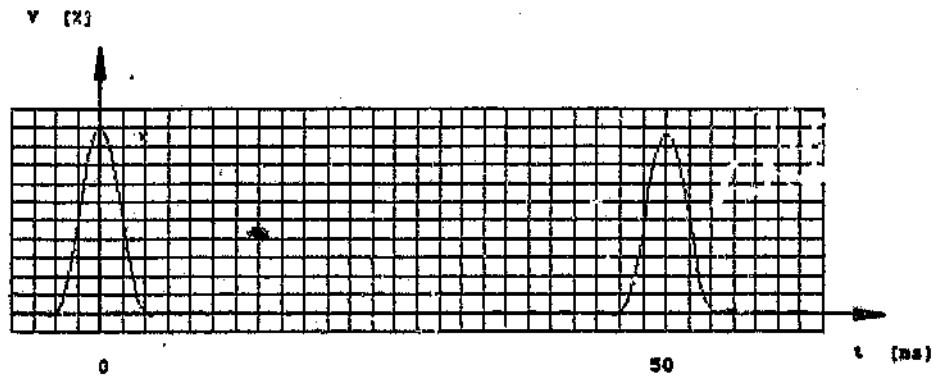
Surge Response

Figure 14.2

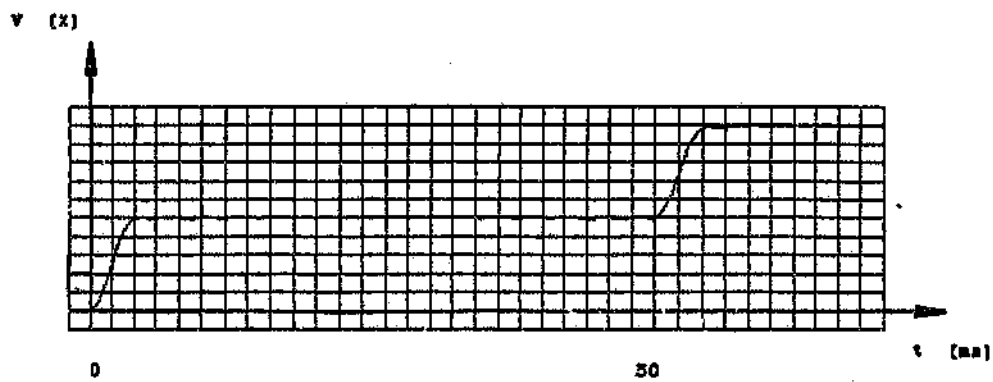
Sample 2 - H : 2080 [A/m]



Attenuation Characteristic



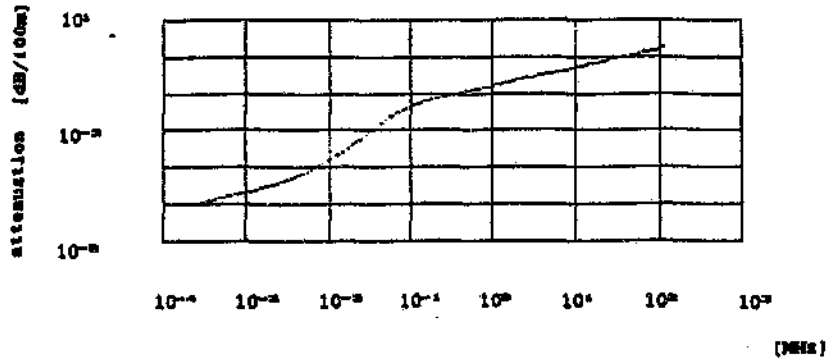
Pulse Response - 3,00 % Attenuation



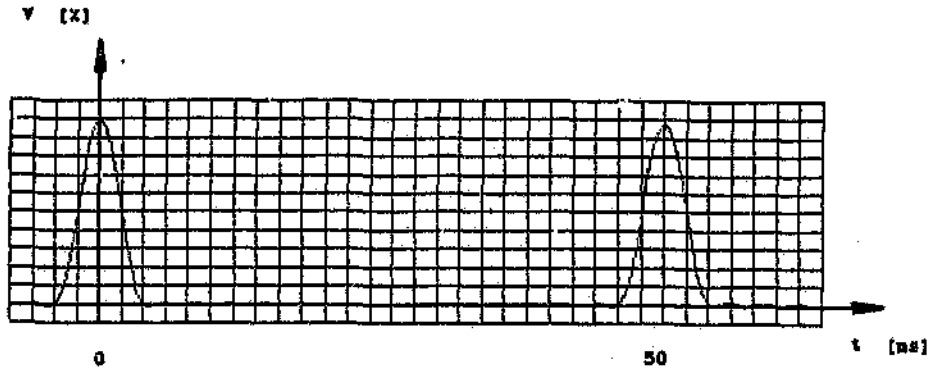
Surge Response

Figure 14.3

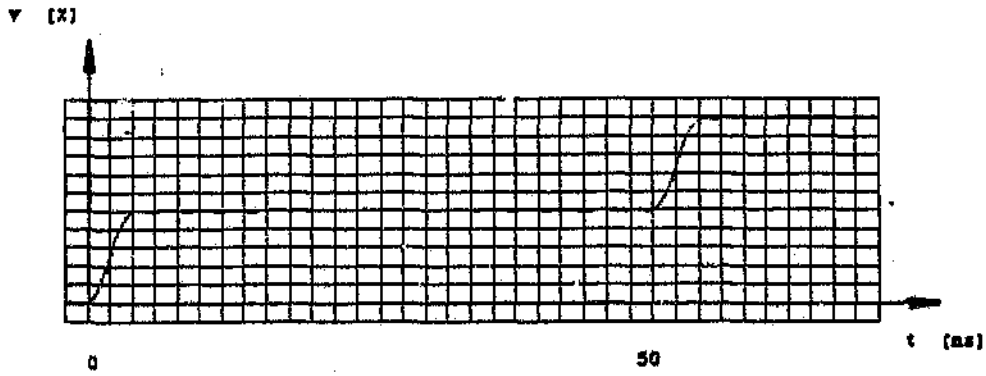
Sample 2 - H = 8320 [A/m]



Attenuation Characteristic



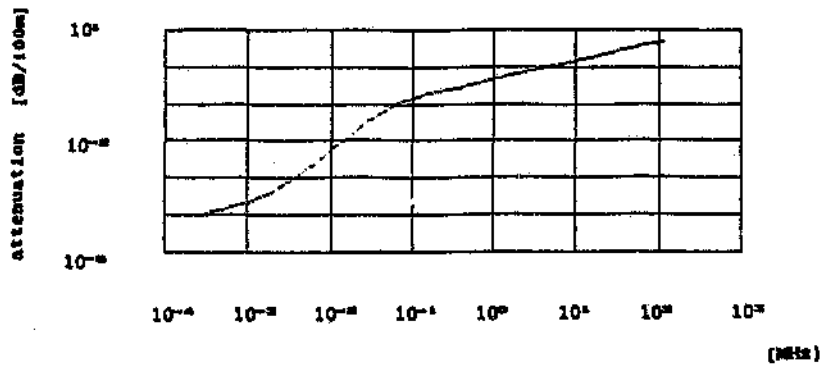
Pulse Response - 2,34 % Attenuation



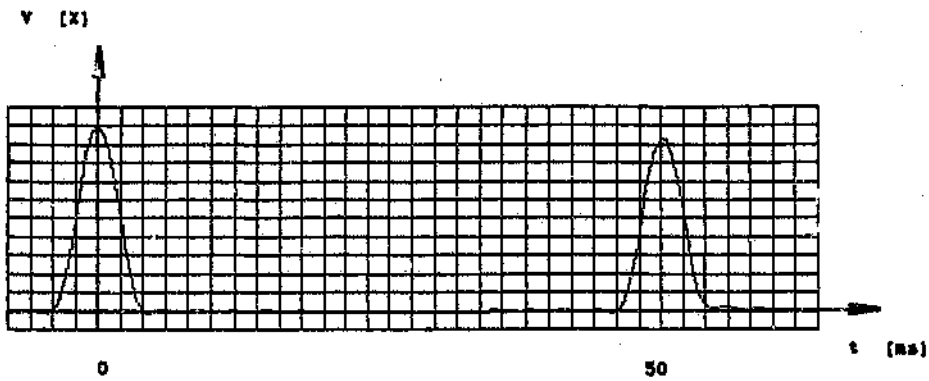
Surge Response

Figure 14.4

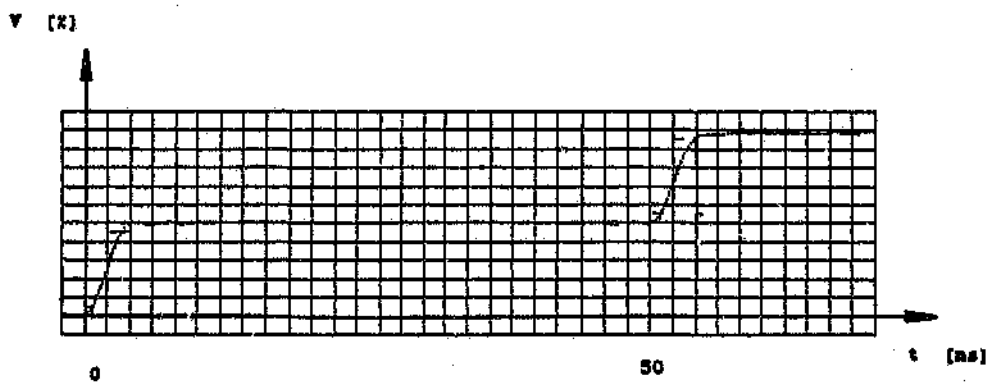
Sample 3 - H = 2080 [A/m]



Attenuation Characteristic



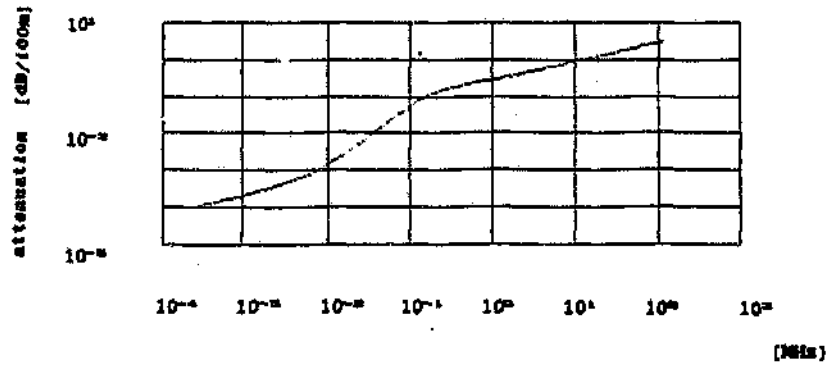
Pulse Response - 6,75 % Attenuation



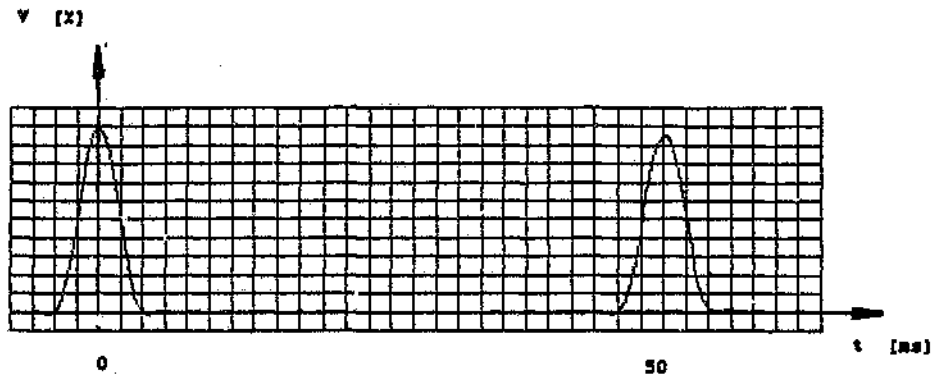
Surge Response

Figure 14.5

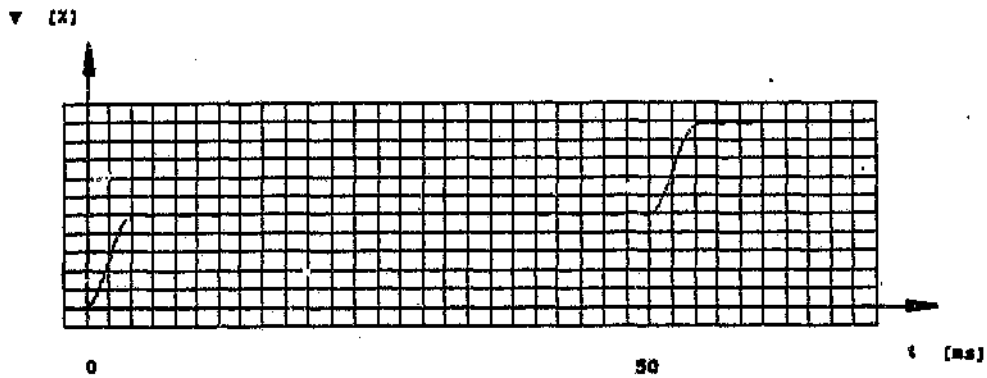
Sample 3 - H = 6320 [A/m]



Attenuation Characteristic



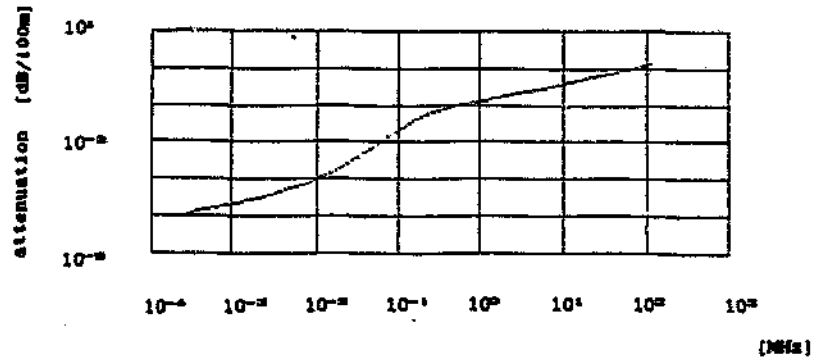
Pulse Response - 4.13 % Attenuation



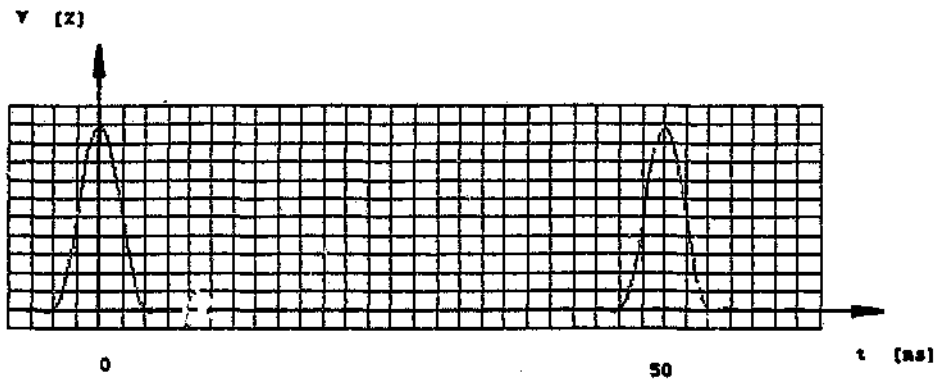
Surge Response

Figure 14.6

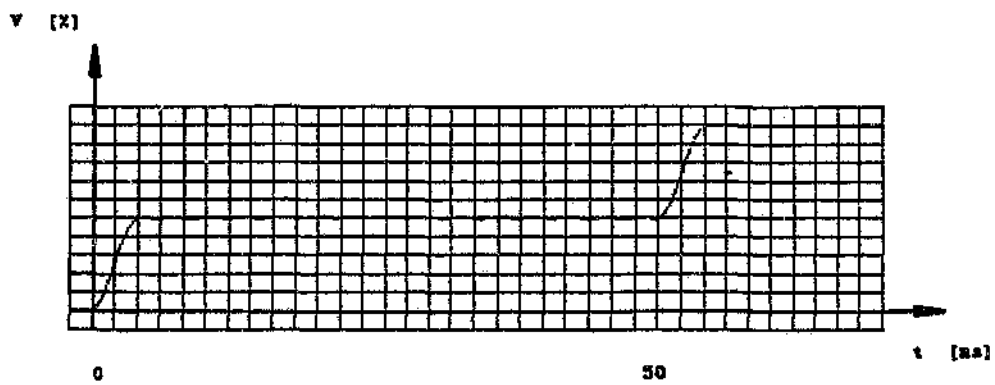
Sample 4 - H = 2080 [A/m]



Attenuation Characteristic



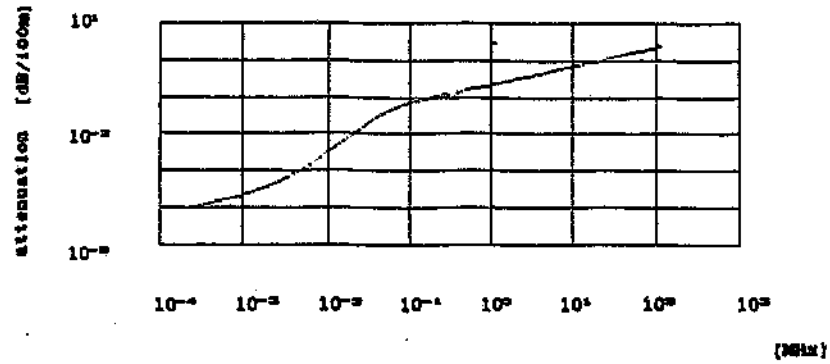
Pulse Response - 1,79 % Attenuation



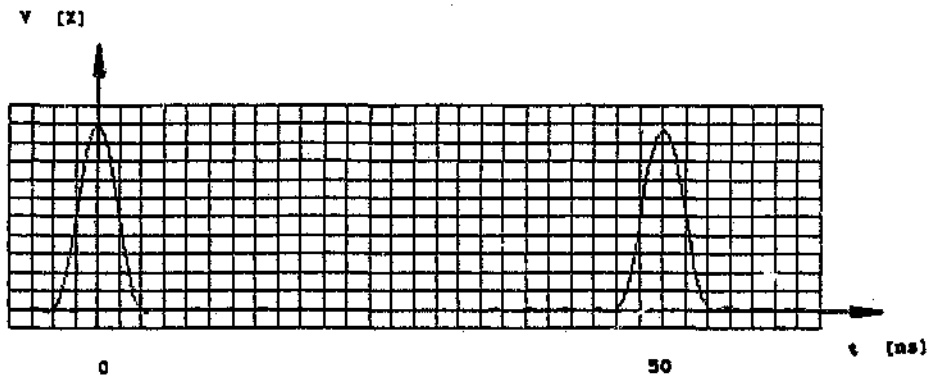
Surge Response

Figure 14.7

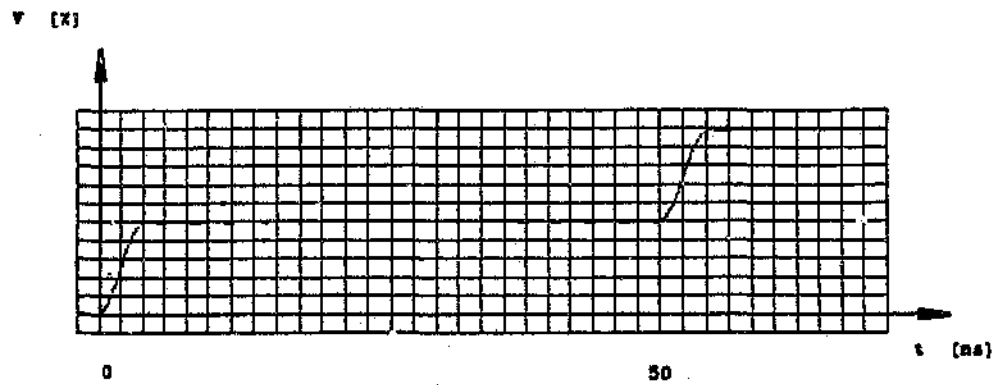
Sample 4 - H = 8320 [A/m]



Attenuation Characteristic



Pulse Response - 3,19 % Attenuation



Surge Response

Figure 14.8

Appendix 15 : Consideration of Reflection and Transmission Coefficients

This appendix serves to explain the determination of the frequency dependent reflection and transmission coefficients, $\rho(f)$and $\tau(f)$. In general, any discontinuity in a SF_6 vessel may have a spacer located at it. For the purposes of this model, spacers are simply modelled as capacitors for the transient conditions. It is well known that if a discontinuity is short (with respect to the wavelength of the signal), then the input impedance of the discontinuity appears to be that of the load. Consequently a spacer, being very short even at frequencies of up to 120MHz, should by rights appear to be the characteristic impedance of the busduct connected on the other side. This is evident from the equation:

$$Z_x = Z_o \cdot \frac{Z_L + Z_o \tanh(\gamma x)}{Z_o + Z_L \tanh(\gamma x)}$$

where : the symbols have their usual meanings, and the nomenclature is shown in *figure 15.1*.

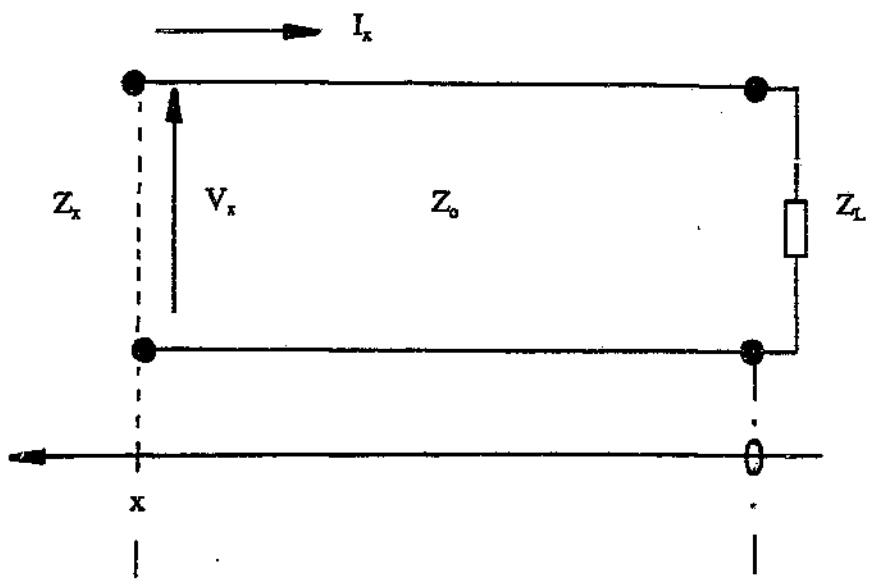


Figure 15.1 : Input impedance of a transmission line terminated in a load impedance.

Under transient conditions, however, the frequency components making up the waveform have not in actual fact encountered the load, and consequently the impedance transfer equation does not apply. For a similar reason the term "surge impedance" is more correctly applied for characteristic impedance under transient conditions.

While the analysis is in fact tedious when frequency dependent effects are included, it is pertinent here to note the definition of the reflection coefficient with and without a spacer at the discontinuity. Also note in the definition that the "direction" in which the particular wave is travelling determines the reflection coefficients as they pertain to the characteristic impedances Z_{o1} and Z_{o2}. Recall the well known equation:

$$\rho_v = \frac{Z_{o2} - Z_{o1}}{Z_{o2} + Z_{o1}}$$

Thus we can model the reflection coefficient for a wave moving from a line with characteristic impedance Z_{o1} to a line with a characteristic impedance Z_{o2} with a capacitor to ground at the point of intersection as follows:

$$\rho_v = \frac{(Z_{o2} - Z_{o1}) - Z_{o1}Z_{o2} \cdot s \cdot C}{(Z_{o2} + Z_{o1}) + Z_{o1}Z_{o2} \cdot s \cdot C}$$

where : $s = j\omega$

It can therefore be easily shown that:

$$|\rho_v| = \frac{1}{\{(Z_{o2} + Z_{o1})^2 + (Z_{o1}Z_{o2}C2\pi f)^2\}} \sqrt{\{(Z_{o2} - Z_{o1})^2 - (Z_{o1}Z_{o2}C2\pi f)^2\}^2 + \{2(Z_{o2} - Z_{o1})(Z_{o1}Z_{o2}C2\pi f)\}^2}$$

and:

$$\angle\rho_v = arctan\left\{\frac{2(Z_{o2} - Z_{o1})(Z_{o1}Z_{o2}C2\pi f)}{(Z_{o2} - Z_{o1})^2 - (Z_{o1}Z_{o2}C2\pi f)^2}\right\}$$

Similar equations may be found for the transmission coefficient. For the model, these equations are generalised as functions of frequency and position in the system. This is more clearly seen in the program itself. The program is thus of the most general form where a capacitor at each discontinuity may be incorporated. Furthermore, in the program, for each discontinuity, the transmission and reflection coefficients are determined for the 'left' and the 'right' side of the discontinuity.

Appendix 16 : Consideration of the Travelling Wave Model

The travelling wave model is packaged in three distinct parts:

- Determination of the "path array" for a given system. This portion of the software generates a list of numbered nodes in the order in which the initial surges would encounter them. This is achieved by searching through a linked list using pointers. The use of pointers is specifically to reduce the permanently defined variables. Thus the technique of pointer definitions rather than array definitions is more suitable for this application. Each ordered number of nodes represents a "path" between the disconnector and the observation point. The number of paths, as well as the number of nodes visited in a path are limited by the software

- Determination of the transmission and reflection coefficients as functions of frequency for all the discontinuities

- Determination of the final time domain form of the transient at the observation point. Once all the transfer functions are known, it is a simple and repetitive procedure to calculate for each the time domain form of the surge occurring at the measuring point as a result of the transfer along that particular path. Thus the third and final portion of the program uses the data produced by the first two portions in order to complete the execution. It must be remembered that our assumptions allow us to build up a single transfer characteristic for each path by adding the transfer characteristics of all the distinctly defined features (paths and discontinuities) along the way. Also, it must be recalled that two surges are generated at the disconnector, travelling in opposite directions - a positive one and a negative one. This must be carefully accounted for, as clearly each see distinctly different families of paths. Once all transfer functions are accounted for, the final time domain waveform is formed by summing the individually determined time domain components

A characteristic of this technique is that each time domain component may be individually examined. This is clear from the description of the program operation. Also the establishment of the valid paths will be recognised as being very similar in operation to a Bewley-Lattice-type simulation, where the reflection matrix is established by accounting for all defined discontinuities.

Let us now briefly study the data and output files of this travelling wave model.

The form of the data file is simple. The first line of data is the total number of discontinuities in the vessel. Thereafter the discontinuities are entered in sequence in the following manner:

The discontinuity is number in the first line of data.
There are two directions from each discontinuity, *left* and *right*. Thus the next line of data pertains to the direction from this discontinuity to the adjoining one. It must be noted at this point the there is no limit to the number of connected discontinuities, nor the number of directions. On the same line in the data file are first the distance to the adjoining discontinuity, and then the discontinuity number.

r 3.30 2

This indicates that there is a connection from this discontinuity to discontinuity number 2 on the right.

l 0.84 3

This indicates that there is a connection from this discontinuity to discontinuity number 3 on the left.
Note that all dimensions for the description of the vessel are in metres. Furthermore, there is no need to list the discontinuities in order, as the linked list is only established once all the discontinuities have been read in. Pointers to each adjoining discontinuity are then established.
The remaining nodes are entered in a similar fashion.

The following is the data descr ne duct in *figure 16.1*, and clearly shows the form of the data file.

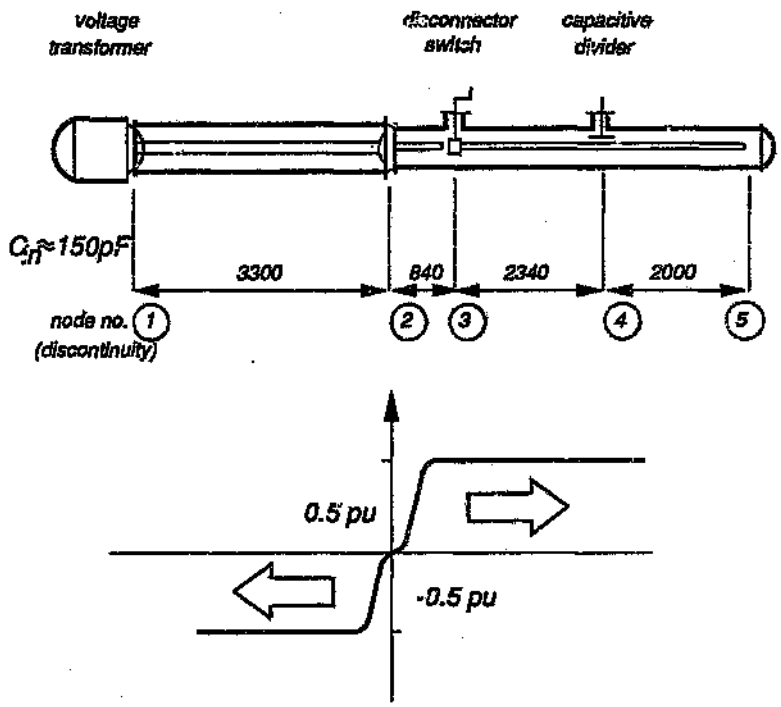


Figure 16.1 : A simple busduct showing the origin of the two initial surges generated at the disconnector. The defined nodes are numbered.

```
5       (* This is the number of discontinuities in the vessel *)

1
r
.
r 3.30 2

2
l
r
.
l 3 30 1
r 0.84 3
```

```
3
l
r
.
l0.84 2
r2.34 4

4
l
r
.
l2.34 3
r2.00 5

5
l
.
l2.00 4
```

This data is input into the program *PathArray*. This program produces a list of all the valid paths. In order to do this, further data is input interactively. This includes listing upon request the discontinuities at which no reflections occur, and the time interval of interest. By assuming that transmission is at the speed of light, the program maintains a running total distance for each path and terminates that path once the time of travel exceeds the observation time. All paths terminating at the observation path within the specified time are written to the output file of this program. As an example, consider an 80ns time interval. The file below is then generated by the program, and indicates:

Firstly the *time interval of interest*. This is followed on the next line by *the total number of paths*. Thereafter the paths are listed in numerical order, listing the nodes visited. It should be noted that the two directions are accounted for in the first two nodes of the path. In the example below, the direction changes at path 12.

```
8.0E-0008       (* The time interval of interest *)
 18
 1
3212121234
 2
32121234
 3
3212123454
 4
321234
 5
32123454
 6
321234543234
 7
3234
 8
323454
```

```
 9
3234543212 34

 10
32345432 34

 11
3234543234 54

 12
34

 13
3454

 14
3454321234

 15
34543212345 4

 16
34543234

 17
3454323454

 18
345432345432 34
```

The program *Reflecco* then prompts the user to define each section of the system described above. The physical details of each individual section (ie material and dimensional characteristics) is requested in order to produce a file of reflection coefficients as functions of frequency. For example, the reflection coefficients at discontinuity 2 in this example are given below for 128 frequency harmonics. The four columns are as follows:

$|H|$ $\angle H$ $|\rho_l|$ $\angle\rho_l$ $|\rho_r|$ $\angle\rho_r$

```
2   (* the number of this particular discontinuity *)
1.000 -0.044 0.077 -0.238 0.077 3.346
1.000 -0.088 0.082 -0.456 0.082 3.531
1.000 -0.132 0.090 -0.644 0.090 3.685
1.000 -0.176 0.100 -0.800 0.100 3.807
1.000 -0.220 0.112 -0.928 0.112 3.902
1.000 -0.263 0.125 -1.034 0.125 3.974
1.000 -0.307 0.139 -1.122 0.139 4.029
1.000 -0.351 0.153 -1.197 0.153 4.071
1.000 -0.395 0.167 -1.262 0.167 4.103
1.000 -0.439 0.182 -1.319 0.182 4.127
1.000 -0.483 0.196 -1.370 0.196 4.145
1.000 -0.527 0.211 -1.415 0.211 4.158
1.000 -0.571 0.226 -1.457 0.226 4.167
1.000 -0.615 0.241 -1.495 0.241 4.173
1.000 -0.659 0.255 -1.530 0.255 4.177
1.000 -0.702 0.270 -1.563 0.270 4.178
1.000 -0.746 0.284 -1.594 0.284 4.178
1.000 -0.790 0.299 -1.623 0.299 4.176
1.000 -0.834 0.313 -1.651 0.313 4.173
```

1.000	-0.878	0.327	-1.677	0.327	4.169
1.000	-0.922	0.341	-1.702	0.341	4.164
1.000	-0.966	0.354	-1.726	0.354	4.158
1.000	-1.010	0.368	-1.749	0.368	4.152
1.000	-1.054	0.381	-1.772	0.381	4.145
1.000	-1.098	0.394	-1.793	0.394	4.138
1.000	-1.141	0.407	-1.814	0.407	4.130
1.000	-1.185	0.419	-1.834	0.419	4.123
1.000	-1.229	0.432	-1.854	0.432	4.114
1.000	-1.273	0.444	-1.873	0.444	4.106
1.000	-1.317	0.456	-1.891	0.456	4.098
1.000	-1.361	0.467	-1.909	0.467	4.089
1.000	-1.405	0.479	-1.927	0.479	4.080
1.000	-1.449	0.490	-1.944	0.490	4.071
1.000	-1.493	0.501	-1.961	0.501	4.062
1.000	-1.537	0.512	-1.977	0.512	4.054
1.000	4.703	0.522	-1.993	0.522	4.045
1.000	4.659	0.533	-2.008	0.533	4.036
1.000	4.615	0.543	-2.024	0.543	4.027
1.000	4.571	0.552	-2.038	0.552	4.018
1.000	4.527	0.562	-2.053	0.562	4.009
1.000	4.483	0.571	-2.067	0.571	4.000
1.000	4.439	0.581	-2.081	0.581	3.991
1.000	4.395	0.590	-2.094	0.590	3.983
1.000	4.352	0.598	-2.108	0.598	3.974
1.000	4.308	0.607	-2.121	0.607	3.966
1.000	4.264	0.615	-2.133	0.615	3.957
1.000	4.220	0.623	-2.146	0.623	3.949
1.000	4.176	0.631	-2.158	0.631	3.940
1.000	4.132	0.639	-2.170	0.639	3.932
1.000	4.088	0.647	-2.182	0.647	3.924
1.000	4.044	0.654	-2.193	0.654	3.916
1.000	4.000	0.661	-2.205	0.661	3.908
1.000	3.956	0.668	-2.216	0.668	3.900
1.000	3.913	0.675	-2.227	0.675	3.892
1.000	3.869	0.682	-2.237	0.682	3.885
1.000	3.825	0.688	-2.248	0.688	3.877
1.000	3.781	0.695	-2.258	0.695	3.870
1.000	3.737	0.701	-2.268	0.701	3.862
1.000	3.693	0.707	-2.278	0.707	3.855
1.000	3.649	0.713	-2.287	0.713	3.848
1.000	3.605	0.718	-2.297	0.718	3.841
1.000	3.561	0.724	-2.306	0.724	3.834
1.000	3.517	0.729	-2.315	0.729	3.827
1.000	3.474	0.735	-2.324	0.735	3.820

The final part of the program, *Transient*, utilises all this data to form, for each path, the transfer function. In other words, it incorporates all the values of $H(f)$, $\rho(f)$, and $\tau(f)$ (which is determined from $\rho(f)$) to form a total transfer function. This is done path by path.

Appendix 17 : Overview of Various Busbar Coating Techniques

Electroplating

Electroplating the final coating material onto the substrate is an attractive alternative since it ensures that no residue of the oxide layer remains on the surface of the aluminium after coating. Hence a mechanically sound and electrically conducting bond is formed between the busbar and the coating. However, the most suitable materials for use in this application are alloys, which are exceedingly difficult to apply in this way (van Thoor, 1970).

Hot Dipping

Hot dipping is the process whereby the substrate is submerged in a bath of molten coating material. Generally, this technique is most successfully applied if the metal to be coated melts at a higher temperature than the coating material. Furthermore, it has been found that, after hot dipping, aluminium/ferrous interfaces become exceedingly brittle due to the formation of an aluminium iron intermetallic compound. Such coated substrates will not tolerate the slightest bending without cracking (van Thoor, 1970).

Metal Spraying

The method considered most suitable for use in this application is that of metal spraying. In this method, metal coatings are sprayed onto the cleaned and roughened substrate in the form of molten metal droplets which congeal and bond immediately on impact. Advantages of this technique include its simplicity and the fact that coating materials that melt at much higher temperatures than the substrate may be used (van Thoor, 1970). In this way, a strong mechanical bond between the substrate and coat is formed. Furthermore, this results in a less brittle product than that formed by hot dipping. However, the coating does not alloy with the substrate, and in the case of aluminium this may imply that a conductive bond is disallowed due to the oxide layer on the substrate. A further consideration is the incompatibility of aluminium and most stainless steels. Any reaction which may be formed between the substrate and the coating must be carefully guarded against if this technique is to prove viable. Both these problems have previously been overcome by first electroplating a thin (6 to 10μm) layer of copper onto the aluminium, and then plating a tin alloy onto the copper (Silveira, 1985). This then forms the substrate for the metal spraying. Such a process would not detract from the effectiveness of the technique, as the really important considerations (in terms of physical attributes) apply to the ferromagnetic coating. The various substrate materials are non-ferrous, and enjoy similar conductivities.

Although a tin alloy (typically alloyed with lead) has a far lower melting point than either the copper or the coating material, the nature of the metal spraying technique is such that this will not adversely affect the metals concerned.

Author: Jandrell Ian Robert.

Name of thesis: Attenuation Of Very Fast Transients In Sf6 Insulated High Voltage Busducts. Theoretical And Experimental Considerations Of The Effect Of A Ferromagnetic Coating Applied To Busbars.

PUBLISHER:

University of the Witwatersrand, Johannesburg
©2015

LEGALNOTICES:

Copyright Notice: All materials on the University of the Witwatersrand, Johannesburg Library website are protected by South African copyright law and may not be distributed, transmitted, displayed or otherwise published in any format, without the prior written permission of the copyright owner.

Disclaimer and Terms of Use: Provided that you maintain all copyright and other notices contained therein, you may download material (one machine readable copy and one print copy per page)for your personal and/or educational non-commercial use only.

The University of the Witwatersrand, Johannesburg, is not responsible for any errors or omissions and excludes any and all liability for any errors in or omissions from the information on the Library website.